

Anomalous Loss of DT Alpha Particles in the Tokamak Fusion Test Reactor

Hans W. Herrmann

A DISSERTATION
PRESENTED TO THE FACULTY
OF PRINCETON UNIVERSITY
IN CANDIDACY FOR THE DEGREE
OF DOCTOR OF PHILOSOPHY

RECOMMENDED FOR ACCEPTANCE
BY THE DEPARTMENT OF
ASTROPHYSICAL SCIENCES

JUNE, 1997

© Copyright 1997 by Hans W. Herrmann.
All rights reserved.

Abstract

Princeton's Tokamak Fusion Test Reactor (TFTR) is the first experimental fusion device to routinely use tritium to study the deuterium-tritium (DT) fusion reaction, allowing the first systematic study of DT alpha (α) particles in tokamak plasmas. A crucial aspect of α -particle physics is the fraction of alphas that escape from the plasma, particularly since these energetic particles can do severe damage to the first wall of a reactor.

An escaping alpha collector probe has been developed for TFTR's DT phase. Energy distributions of escaping alphas have been determined by measuring the range of α -particles implanted into nickel foils located within the alpha collector. Results at 1.0 MA of plasma current are in good agreement with predictions for first orbit alpha loss. Results at 1.8 MA, however, show a significant anomalous loss of partially thermalized alphas (in addition to the expected first orbit loss), which is not observed with the lost alpha scintillator detectors in DT plasmas, but does resemble the anomalous 'delayed' loss seen in DD plasmas. None of the candidate explanations proposed thus far are fully consistent with the anomalous loss observations.

An experiment designed to study the effect of plasma major radius shifts on α -particle loss has led to a better understanding of α -particle dynamics in tokamaks. Intuitively, one might suppose that confined marginally passing α -particles forced to move toward higher magnetic field during an inward major radius shift (i.e. compression) would mirror and become trapped particles, leading to increased alpha loss. Such an effect was looked for during the shift experiment, however, no significant changes in alpha loss to the 90° lost alpha scintillator detector were observed during

the shifts. It is calculated that the energy gained by an α -particle during the inward shift is sufficient to explain this result. However, an unexpected loss of partially thermalized α -particles near the passing/trapped boundary was observed to occur between inward and outward shifts at an intermediate value of plasma current (1.4 MA). This anomalous loss feature is not yet understood.

Acknowledgments

Very special thanks go to my advisor, Dr. Stewart J. Zweben, who provided endless advice and guidance. Needless to say, without his support this work would not have been possible. Of course there are many others who have contributed to this effort. In particular, I would like to thank Doug Darrow, the other third of the ‘Lost Alpha Team’, for his valuable insights. Two others, who were very close to this project, but were unfortunate victims of the Great Reduction in Force of ’95, were John Timberlake and Janet Felt. John’s superb engineering skills were crucial to the completion of the Alpha Collector, and Janet’s meticulous programming skills were instrumental in the modeling of the results.

I am greatly indebted to the managerial ranks of TFTR for realizing the importance of graduate student involvement in ‘big science’. These leaders of the TFTR project include Kingston Owens, Dave Johnson, Ken Young, Kevin McGuire, Mike Bell and Rich Hawryluk. I am also grateful for the contributions of the physicists of the TFTR team, in particular, Ben LeBlanc, Ed Synakowski, Ken Hill, Rob Budny, Emil Ruskov, Steve Batha, Fred Levinton, Sid Medley, Zuoyang Chang, Mike Zarnstorff and Schwick von Goeler. Of course, the wisdom of several theorists, such as Harry Mynick, Nicolai Gorolenkov, Roscoe White and C. S. Chang, was essential in the understanding of alpha physics. Fellow students Mark Herrmann, John Wright, Steve Smith, Steve Cauffman, Jaeyoung Park and Bob Heeter, helped me work out many of the details as well as providing moral support.

The assistance of Carl Tilson, Steve Williams and the rest of the HP division, as well as John Collins, Joe Winston and the rest of the TVPS division is greatly appreciated. Their professional attitude and strict adherence to procedure assured

my safety during many evolutions involving tritium. Further technical support was provided by Greg Lemunyan, Mike Vocaturo, Art Brooks, Mike Diesso, Judy Giarrusso and Doug Loesser, among others. Administrative support was received from Ann McKee, Betty Carey, Terry Greenberg, and most importantly, Barbara Sarfaty.

This work allowed me to form several valuable external collaborations. Special thanks go to Glenn Chong, Spencer Pitcher, Jim Davis, A.A. Haasz of the University of Toronto's Institute for Aerospace Studies, for developing and operating the sample analysis system used to analyze the foils from the Alpha Collector. Glenn's tireless efforts are much appreciated. From this collaboration sprung several others, including Rick Macaulay-Newcomb at McMaster University, who performed calibration implants on their Van de Graaff accelerator, and Armando Antoniazzi at Ontario Hydro Technologies, who helped develop the tritium decontamination method used on the foils. Also, Tom Winter of Pennsylvania State University, Wilkes-Barre campus, was extremely generous in performing time consuming atomic cross section computations for this work.

I would like to thank my readers, who have all been mentioned previously, for their valuable suggestions. These were Roscoe White, Dave Johnson, Stewart Zweben and Doug Darrow.

Finally I wish to thank my extended family who were always there for me: most importantly, my wife, Ryn, and much more recently, my son, Charlie, who have been my inspiration; my parents, Karl and Elfi Herrmann, who have always provided the moral (and proof reading) support I needed; my in-laws, Larry and Tudy Hatch, who have provided many vacation opportunities over the years which have allowed us to 'get away from it all'; and the many siblings, siblings-in-law and friends who have believed in me.

This work was supported by US DoE contract number DE-AC02-76-CHO-3073, Canadian Fusion Fuels Technology Project, and Natural Sciences and Engineering Research Council of Canada

Dedicated to Ryn and Charlie, for all their love and support!

Contents

Abstract	iii
1 Introduction and Motivation	1
1.1 Introduction	2
1.2 Motivation	6
1.3 Objective	7
1.4 Thesis Outline	7
2 Review of Escaping Alpha Particle Physics in Tokamaks	8
2.1 Introduction	9
2.2 Charged Particle Orbits	9
2.2.1 Single Particle Orbits in Real Space	9
2.2.2 Orbits in Phase Space	11
2.3 Classical Alpha Loss	14
2.3.1 First Orbit Loss	15

2.3.2	TF Ripple Induced Loss	15
2.4	Nonclassical Alpha Loss	17
2.4.1	Collisional Nonprompt Loss	17
2.4.2	MHD Induced Loss	18
2.4.3	RF Induced Loss	19
2.5	Previous Experimental Results	19
2.5.1	Lost Alpha Scintillator Detectors	19
2.5.2	Summary of Previous TFTR Results	21
3	Alpha Collector - Description	22
3.1	Introduction	23
3.2	Detection Technique	23
3.3	Probe Head Design	25
3.4	Sample Analysis	30
3.4.1	Thermal Desorption Spectrometry	30
3.4.2	Absolute Calibration	33
3.4.3	Decontamination	34
3.5	TFTR Implementation	35
3.6	Comparison to Lost Alpha Scintillator Detectors	40
4	Alpha Collector - Modelling and Results	45

4.1	Introduction	46
4.2	First Orbit Loss Model	46
4.2.1	Pitch Angle Distribution	46
4.2.2	Range Distribution	49
4.3	Experimental Results	54
4.3.1	Absolute Fluence	59
4.3.2	Energy Distribution	63
4.3.3	Pitch Angle Distribution	68
4.3.4	Radial Distribution	75
4.3.5	Uncertainties	79
4.4	Discussion	81
4.4.1	Summary of Experimental Results	81
4.4.2	Comparison of 1.8 MA Anomalous Loss with Delayed Loss . .	82
4.4.3	Trajectories of anomalous loss orbits	84
4.5	Possible Anomalous Loss Mechanisms	88
4.5.1	Collisional Loss	89
4.5.2	Toroidal Field (TF) Ripple Effects	89
4.5.3	MHD Effects	91
4.5.4	Loss of He^+ from Charge Exchange with Impurities or NBI Neutrals	91
4.5.5	Loss during I_p Rampdown	102

4.5.6	Scattering off RF Limiters and Collimator Walls	104
4.5.7	Activation of Surrounding Materials	104
4.5.8	Foil Surface Fusion	105
4.5.9	Diffusion of Residual He	105
4.5.10	Diffusion of Implanted He	106
4.6	Summary, Conclusions, and Suggestions for Future Work	106
5	Major Radius Shift Experiment	107
5.1	Introduction	108
5.2	Experiment	112
5.2.1	Experimental Design and Initial Expectations	112
5.2.2	Experimental Results	114
5.3	Discussion	120
5.3.1	Shift Induced Loss	120
5.3.2	Anomalous Loss Between the Shifts	127
5.4	Summary, Conclusions, and Suggestions for Future Work	134
6	Conclusion	135
6.1	Introduction	136
6.2	Alpha Collector	136
6.2.1	Summary	136

6.2.2	Conclusions	137
6.2.3	Suggestions for Future Work	140
6.3	Major Radius Shift Experiment	140
6.3.1	Summary and Conclusions	140
6.3.2	Suggestions for Future Work	141
	Bibliography	142

List of Figures

1.1	DT Reaction	3
1.2	Tokamak Geometry	5
2.1	Confined Alpha Particle Orbits	10
2.2	Real and Constants of the motion space	13
2.3	Lost Alpha Scintillator Detectors	20
3.1	Alpha Implantation Ranges in Nickel	24
3.2	Assembled Probe Heads	25
3.3	Probe Head Blueprint	26
3.4	Foil and Spool Assembly	28
3.5	Sample Analysis System	31
3.6	Calibration Samples	33
3.7	Alpha Collector shown in Poloidal Cross Section of TFTR	36
3.8	Alpha Collector in Top View of TFTR	37
3.9	Alpha Collector in Side View of TFTR	38

3.10	Alpha Collector Probe Head Designs	39
4.1	1.8 MA Predicted Alpha Collection Fraction	48
4.2	Alpha Collector Pitch Angle Acceptance	51
4.3	Alpha Implantation Ranges in Nickel	53
4.4	Port transmission fraction vs. Port depth	57
4.5	1.0 MA Fluence measurement	60
4.6	1.8 MA Fluence measurement	61
4.7	Lost Alpha Scintillator Detector I_p dependence	62
4.8	1.0 MA Implantation Range Distributions	64
4.9	1.8 MA Implantation Range Distributions	66
4.10	Lost Alpha Scintillator Gyroradius Distributions	67
4.11	1.0 MA Left Collection Fraction	69
4.12	1.8 MA Left Collection Fraction	71
4.13	1.8 MA Relative Detector Collection Efficiency	72
4.14	Lost Alpha Scintillator Detector Pitch Angle Distributions	74
4.15	1.0 MA Alpha Radial Distributions	76
4.16	1.8 MA Alpha Radial Distributions	78
4.17	1.8 MA Alpha Particle Orbits	85
4.18	Impurity Charge Exchange Cross Sections	93
4.19	Alpha Orbit CX Transition Leading to Outward Transport	94

4.20	Alpha Orbit CX Transition Leading to Inward Transport	96
4.21	1.8 MA Pitch vs. r/a Diagram	97
4.22	Pitch Angle Distribution due to CX	100
4.23	Energy Distribution due to CX	101
4.24	Slowing Down Times	103
5.1	Marginally Passing α -particle Orbit	109
5.2	Collisional Nonprompt Loss	110
5.3	R Shift Waveforms	113
5.4	R Shift Lost Alpha Detector Signals	115
5.5	R Shift Lost Alpha Detector Mean Gyroradius	117
5.6	R Shift Lost Alpha Detector Mean Pitch Angle	118
5.7	R Shift Lost Alpha Detector Pitch Angle Distribution	119
5.8	P/T Boundary Shift	123
5.9	R Shift Predicted Lost Alpha Detector Signal Increase	125
5.10	Baseline Mean Gyroradius as a Function of Pitch Angle	129
5.11	Calculated Pitch Angle Distributions	130
5.12	Nonprompt Loss before and after IN shift	132

List of Tables

3.1	Comparison of Escaping Alpha Diagnostics	40
4.1	Alpha Collector Discharge Parameter List	54
4.2	Anomalous Loss Explanations	88
5.1	R Shift Shot List	114

Chapter 1

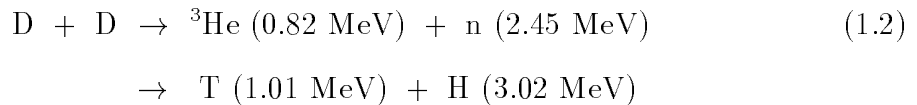
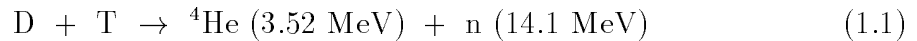
Introduction and Motivation

1.1 Introduction

For the past 45 years, scientists have been attempting to realize the potential of fusion energy, the energy source that powers the sun. Fusion could provide a safe, clean, virtually inexhaustible energy source here on earth. Substantial progress has been made in this endeavor, but the goal of commercial fusion power plants has not yet been achieved.

Fusion Reactions

In a fusion reaction, in which light nuclei are ‘fused’ together, mass (m) is converted to energy (E) according to Einstein’s famous formula $E=mc^2$ [1], where the speed of light ($c=3\times 10^{10}$ cm/s) squared provides an enormous conversion factor. The fusion reactions that have been the main focus of fusion energy research are:



where the fusion fuel nuclei are the isotopes of hydrogen, deuterium (D) and tritium (T), and the two branches of Eq. 1.2 occur with equal probability. The DT reaction of Eq. 1.1 is illustrated in Fig. 1.1.

In order for the positively charged nuclei on the left sides of Eqs. 1.1 and 1.2 to fuse together they must have sufficient energy to overcome their mutual electrostatic repulsion that is the result of having like electrical charge. Once they get close enough, the strong force, which holds positively charged protons together in a nucleus, takes over and binds them into a new larger nucleus. The resulting nucleus is unstable and immediately decays to the fusion products on the right sides of Eqs. 1.1 and 1.2. The sum of the masses of the products is slightly less than that of the reactants. This mass difference is converted to energy. Conservation of momentum determines the fraction of this energy that each fusion product receives in the form of kinetic energy, which

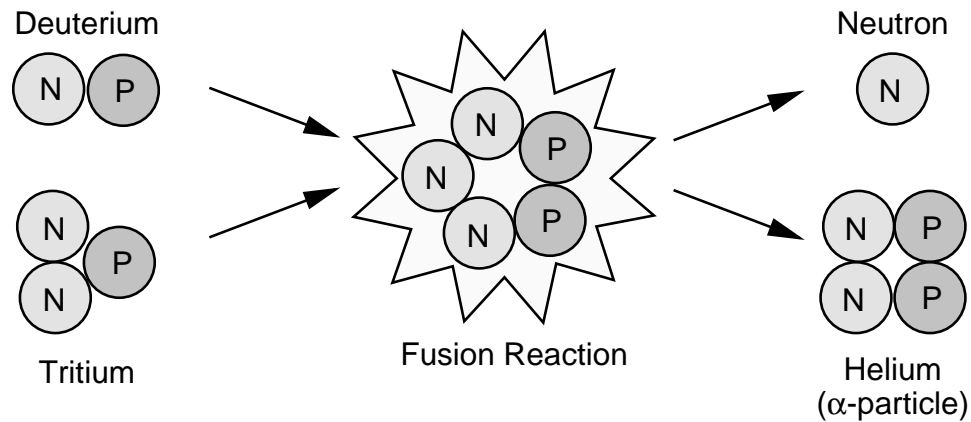


Figure 1.1: *The DT fusion reaction of Eq. 1.1 consists of the nuclei of deuterium and tritium fusing together to produce an unstable nucleus which immediately decays to an energetic neutron and helium nucleus (also known as an alpha (α) particle). The nuclei are made up of positively charged protons (P) and electrically neutral neutrons (N).*

is shown in parenthesis in Eqs. 1.1 and 1.2 where the units are millions of electron volts (eV)¹.

Plasma Confinement

In order for charged particles to have sufficient energy to overcome their repulsion so they can fuse, a working fusion reactor will require the fusion fuel to be heated to hundreds of millions of degrees Celsius ($\gtrsim 10,000$ eV), more than ten times hotter than the interior of the sun. At these temperatures matter exists in the plasma state, i.e. a gas made up of charged particles (free electrons and ions). The main difficulty in attaining a working fusion reactor has been confining these charged particles and the energy they possess for long enough periods such that the fusion power output exceeds the input power needed to heat the plasma. The point at which the fusion power output is equal to the heating power input is known as ‘breakeven’. Princeton’s

¹An eV is the energy an electron gains when accelerated by a 1 Volt potential. The temperature of a substance is determined by the average kinetic energy of its constituent particles (i.e. molecules, atoms, ions, electrons) and can be expressed in eV, where each eV is $\approx 11,000^\circ\text{C}$.

Tokamak Fusion Test Reactor (TFTR) currently holds the world’s record in progress toward breakeven, with an output fusion power about 30% that of the input power [2].

In magnetic confinement fusion, magnetic fields are used to confine the plasma in a ‘magnetic bottle’. This is made possible by the Lorentz force which constrains charged particles to move in helical trajectories about magnetic field lines. This also acts to confine the charged fusion products such as the 3.5 MeV helium (He) nucleus, also known as an alpha (α) particle, seen on the right side of Eq. 1.1. The 14 MeV neutron (n) produced in this reaction, having no charge, is free to pass through the magnetic field and out through the wall of the confinement device where its energy can be used to drive a thermal cycle for the production of electricity. Once the power being transferred to the plasma from the energetic α -particles equals the power needed to sustain the fusion reaction, the reactor reaches the self-sustaining point known as ‘ignition’ at which external heating sources are no longer needed.

Tokamak Reactor

The confinement device which has been the focus of magnetic fusion research for the past ~ 30 years is a Russian invention known as the tokamak [3]. The tokamak has an externally generated toroidal magnetic field (\mathbf{B}_t) inside a ‘doughnut’ shaped plasma as shown in Fig. 1.2. What distinguishes the tokamak from other toroidal confinement devices is the addition of a poloidal magnetic field (\mathbf{B}_p) generated internally by driving a current in the plasma. The resultant magnetic field (\mathbf{B}) winds around inside the tokamak in a helical fashion. \mathbf{B}_t is generated by toroidal field (TF) coils that encircle the vacuum vessel (not shown in Fig. 1.2) in the poloidal direction. \mathbf{B}_p is generated by the plasma current (I_{plasma}) which is, in turn, induced through transformer action by a solenoid coil (also not shown) wound around the central axis. The plasma current also acts to heat the plasma through resistive heating similar to the heating of a wire carrying a current. The tokamak plasma is heated further through the injection of energetic fuel atoms from a series of particle accelerators known as neutral beam injection (NBI).

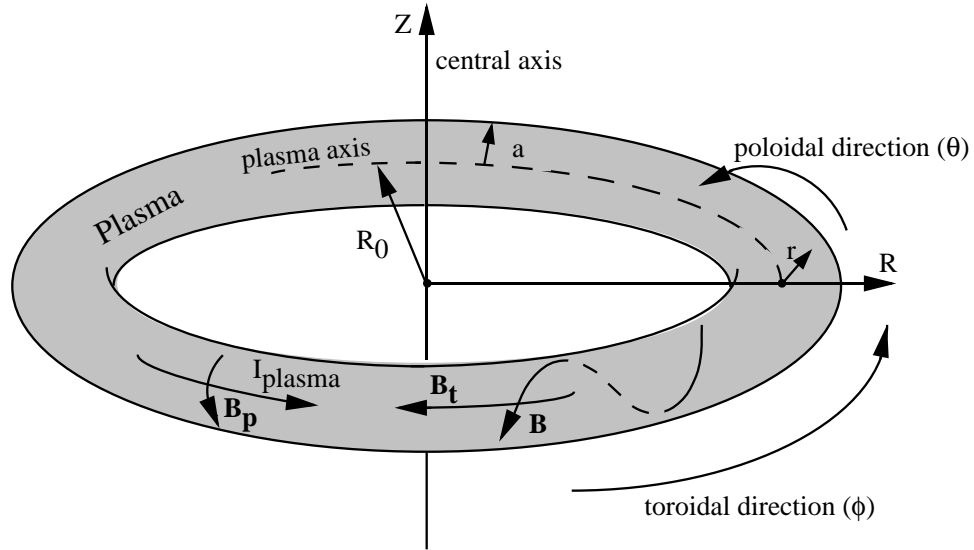


Figure 1.2: *The plasma inside a tokamak vacuum vessel is confined by an externally generated toroidal magnetic field (\mathbf{B}_t) and an internally generated poloidal magnetic field (\mathbf{B}_p), which combine to form a helical magnetic field (\mathbf{B}). The cylindrical (R, Z, ϕ) and the toroidal (r, θ, ϕ) coordinate systems are used to describe the toroidal geometry. Plasma dimensions are defined by the major (R_0) and minor (a) radii.*

Tritium

The DD reactions in Eq. 1.2 have been the primary fusion reactions studied in experimental devices. However, it is the DT reaction of Eq. 1.1 that the first generation of commercial fusion reactors will most likely be based on, since it has the highest fusion reaction rate and requires lower plasma temperatures than other fusion reactions. The DT reaction is not normally used in fusion research due to the radioactive concerns involving tritium. Tritium undergoes beta decay, making it a biological hazard if ingested, with a 12.5 year half life. Furthermore, the increased neutron production from the DT reaction activates reactor components such that they too become radioactive. Hence, the introduction of tritium requires special handling and shielding. The DD reaction has provided valuable information regarding the confinement of fusion grade plasmas, but the development of a working fusion reactor requires addressing the unique issues of DT. In particular, alpha particle behavior and its effect on thermonuclear plasmas must be investigated. TFTR is the first experimental

fusion device to use tritium as a fusion fuel on a routine basis and has conducted the first systematic study of alpha particle physics.

1.2 Motivation

Escaping Alpha Particles

A crucial aspect of alpha particle physics, and the topic of this dissertation, is the fraction of alphas lost to the first wall of the reactor. Alphas which escape from the plasma prior to transferring their excess energy to the plasma (i.e. thermalization) reduce the self-heating power available to achieve ignition. But more importantly, in the design of the International Thermonuclear Experimental Reactor (ITER) and future DT reactors, it will be necessary to predict the alpha particle losses to the first wall and divertor plates, since even a few percent loss may cause damage due to localized heating. Studying alpha particle loss also provides insight into the physics of internal plasma processes, such as plasma instabilities and the effect of numerous alphas acting collectively to perturb the plasma.

Studies of alpha particle loss mechanisms could also prove valuable in developing much needed techniques for improving reactor performance. For instance, once the alphas have thermalized with the bulk plasma, they are no longer useful and actually degrade fusion performance by diluting the plasma. A method of ‘helium ash removal’ is needed to minimize this dilution by extracting α -particles after they have transferred a significant fraction of their energy to the plasma. Another sought after technique is ‘alpha channeling’ [4]. Normally, the majority of alpha power transfers to the plasma electrons. The electrons do not however take part in the fusion reaction. Reactor efficiency could be greatly enhanced if this power could be diverted directly to the plasma ions, which need energy to fuse. Alpha channeling would use a radio frequency (RF) wave as a catalyst to redirect the alpha power to the bulk ions, or to serve some other useful function such as driving plasma current.

1.3 Objective

The main objectives of this thesis were to develop and evaluate a new escaping alpha particle diagnostic, and to conduct new alpha particle experiments on TFTR to gain added insights into alpha particle physics. To this effect, the alpha collector probe, based on the implantation of alpha particles into nickel foils, was developed and implemented on TFTR. This work led to the discovery of an unexpected alpha particle loss, which is not yet understood, but may be a concern in the development of a commercial tokamak reactor. In addition, an experiment designed to study the effect of plasma compression on alpha particle loss has led to a better understanding of alpha particle dynamics in tokamaks.

1.4 Thesis Outline

This thesis is organized into six chapters. In chapter 2 there is a review of escaping alpha particle physics in tokamaks including a summary of measurements made on TFTR using scintillator based detectors. Chapter 3 contains a description of the alpha collector, the diagnostic developed to measure escaping alphas in TFTR in the course of this dissertation, including the factors that influenced design choices. Chapter 4 presents the results of escaping alpha measurements made with alpha collector and compares them to numerical modeling and measurements made with the lost alpha scintillator detectors. This analysis reveals the existence of a previously undetected anomalous loss of partially thermalized alphas. Several candidate loss mechanisms are considered, but none of them offer a satisfactory explanation for this anomalous loss. In chapter 5, the results of the major radius shift (i.e. plasma compression) experiment are evaluated with the aid of a powerful ‘constants of the motion’ theoretical formalism. Chapter 6 contains a summary of results and recommendations for future efforts.

Chapter 2

Review of Escaping Alpha Particle

Physics in Tokamaks

2.1 Introduction

To understand alpha particle loss it is first necessary to understand typical charged particle orbits in tokamaks. Sec. 2.2 contains a description of these orbits for high energy ions. In Secs. 2.3 and 2.4 the various classical and nonclassical high energy ion loss mechanisms are summarized. These loss mechanism descriptions are expanded upon in later chapters as needed. Sec. 2.5 gives a description of the lost alpha scintillator detectors which have provided most of the experimental observations of charged fusion product loss on TFTR and a brief summary of these observations. A comprehensive review of fast ion physics in tokamaks can be found in Ref. [5].

2.2 Charged Particle Orbits

2.2.1 Single Particle Orbits in Real Space

Charged particles locally follow helical trajectories about magnetic field lines according to the Lorentz force equation:

$$\mathbf{F} = q(\mathbf{E} + \frac{1}{c}\mathbf{v} \times \mathbf{B}) \quad (2.1)$$

where, under most circumstances in a tokamak, the electric field term is negligible for fast ions. As a result of the combination of the toroidal and poloidal magnetic fields, the magnetic field lines in a tokamak spiral around the torus in a helical fashion. In the limit of zero particle energy, the guiding center of charged particle orbits follow these field lines. But for finite energy, vertical drifts associated with the nonuniformity of the B field play an important role. In particular, the radial dependence ($B_t \sim \frac{1}{R}$) and curvature of the toroidal magnetic field combine to produce a downward ion drift in TFTR given by:

$$v_{drift} = (E_{\perp} + 2E_{\parallel}) \frac{\mathbf{B} \times \nabla \mathbf{B}}{qB^2} \quad (2.2)$$

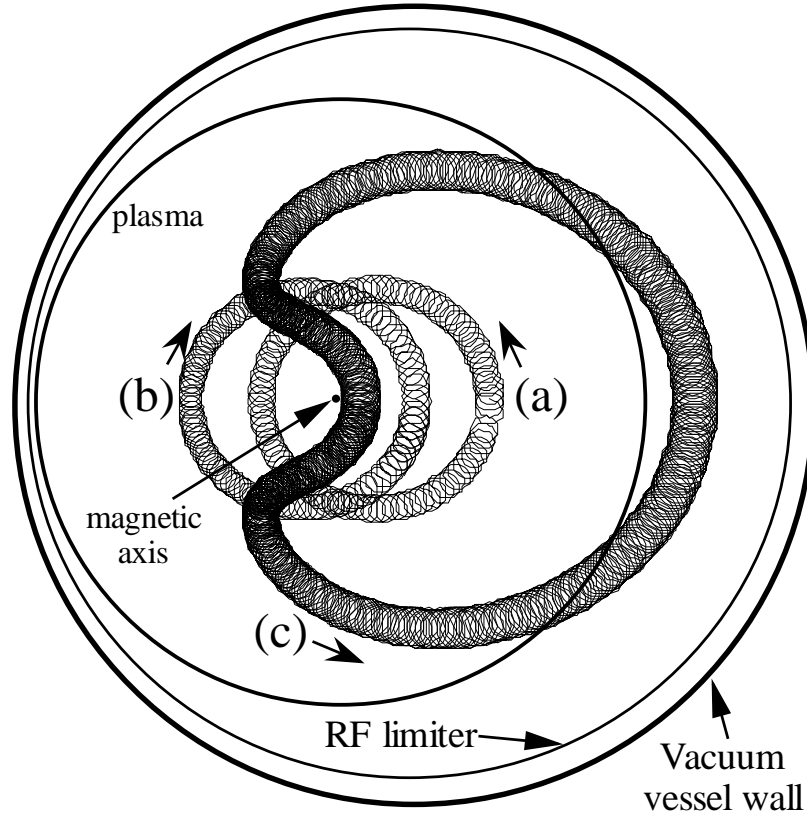


Figure 2.1: *Poloidal cross section of TFTR illustrating projections of: (a) a co-going passing orbit; (b) a counter-going passing orbit; and (c) a trapped orbit. Calculated for 3.5 MeV alpha particles in an $R=2.45$ m, $I_p=1.6$ MA plasma with $B_t=5.0$ tesla. Passing orbits (a) and (b) have the same magnetic moment.*

where the terms containing the perpendicular and parallel (in relation to the direction of the magnetic field) components of the energy (E) correspond to the $\nabla\mathbf{B}$ drift and the curvature drift, respectively.

If not for the helical spiraling of the magnetic field lines, known as rotational transform, these drifts would cause charged particles to drift down to the bottom of the TFTR vessel. However, the rotational transform causes high energy ions to follow drift surfaces that are displaced outward (inward) in major radius from magnetic flux surfaces for particles that are co-going (counter-going) in relation to the plasma current. Fig. 2.1 shows the poloidal projections representative of the three main orbit

classifications¹: (a) Co-going Passing; (b) Counter-going Passing; and (c) Trapped or ‘Banana’ orbits. The banana orbit results from the conservation of magnetic moment, $\mu = \frac{E_{\perp}}{B}$, and energy, E . As a charged particle moves into a region of increasing magnetic field, E_{\perp} must increase to maintain μ constant, while E_{\parallel} must decrease to maintain E constant. When the parallel energy decreases to zero, the particle mirrors and changes its toroidal direction going from counter-going to co-going, or vice versa, forming the banana ‘tips’.

2.2.2 Orbits in Phase Space

The orbit of a charged particle in a given magnetic configuration is uniquely determined by its instantaneous position, \mathbf{r} , and velocity, \mathbf{v} , vectors. These quantities define a six dimensional phase space in which the orbit types and loss boundaries can be delineated. However, by tracking only the guiding center motion of a particle, this phase space can be reduced to just three dimensions. The helical Larmor motion about the guiding center can be added back on, if desired, with only a loss of the phase information.

A common method of representing this phase space is by defining three normalized variables at the guiding center’s outer midplane crossing point, such as the minor radius, r/a , the magnitude of the velocity, v/v_0 (where v_0 is the birth velocity), and the pitch, v_{\parallel}/v . However, these quantities are not conserved under most processes that affect charged particle orbits. A better method is to choose three constants of the motion that are either conserved during such processes, or whose changes can be predicted.

Three convenient constants of the motion are the particle’s magnetic moment, μ , canonical angular momentum, P_{ϕ} , and energy, E [7], given by:

$$\mu = E_{\perp}/B \tag{2.3}$$

$$P_{\phi} = mRv_{\phi} - \frac{e}{c}\Psi \cong \frac{mRB_{\perp}v_{\parallel}}{B} - \frac{e}{c}\Psi \tag{2.4}$$

¹For a more complete discussion of particle orbits, including less common orbit types, see Ref. [6].

$$E = \frac{1}{2}mv^2 \quad (2.5)$$

where Ψ is the poloidal magnetic flux. Solving Eqs. 2.3 and 2.4 for μ in terms of P_ϕ we find:

$$\mu = \frac{E}{B(R, Z)} - \frac{B(R, Z)}{2mR^2B_t^2(R, Z)}\left(P_\phi + \frac{e}{c}\Psi(R, Z)\right)^2 \quad (2.6)$$

It can be seen from Eq. 2.6 that, for a given energy, a fixed (R, Z) position in real space transforms to an inverted parabola in (μ, P_ϕ) space. Thus, the set of all orbits at a given energy passing through one (R, Z) point is a parabola in (μ, P_ϕ) space. The apex of a fixed (R, Z) parabola corresponds to the orbit which has $v_{\parallel} = 0$ at (R, Z) , while the right leg of the parabola corresponds to orbits that are co-going ($v_{\parallel} > 0$), and the left leg to counter-going ($v_{\parallel} < 0$), as they pass through this (R, Z) position. Fig. 2.2(a) defines the three points in real (R, Z) space that make up the plasma boundary in (μ, P_ϕ) space, namely the magnetic axis (MA) and the inner and outer midplane points (IMP and OMP) of the last closed flux surface (LCFS). The parabolas corresponding to these plasma boundary points are shown in Fig. 2.2(b) for fixed α -particle energy. All other points in the plasma are represented by parabolas that fall between these three borders, such their apexes fall within the shaded trapped (TL and TC) region.

The different orbit classes are delineated by boundaries in the constants of the motion space as shown in Fig. 2.2(b)². The passing/trapped boundary is formed by the low μ border of the trapped region which is found by setting $v_{\parallel} = 0$ from the magnetic axis to the LCFS along the inner midplane. Similarly, the high μ border of the trapped region is found by setting $v_{\parallel} = 0$ from the magnetic axis to the LCFS along the outer midplane. The low P_ϕ border of the trapped region is found by setting $v_{\parallel} = 0$ along the LCFS from the outer to the inner midplane.

The guiding center trajectory of an α -particle orbit can be thought of as a collection of all the fixed (R, Z) parabolas in (μ, P_ϕ) space satisfying Eq. 2.6 that pass through the α -particle's fixed (μ, P_ϕ) point, constrained by the condition that the apex of all these parabolas must lie within the shaded trapped region (or to the left of the LCFS $v_{\parallel} = 0$ line for orbits extending outside the LCFS). For example, if an

²Slight modifications to these borders due to the existence of special orbit classes such as 'D orbits' [7] are ignored for illustrative purposes.

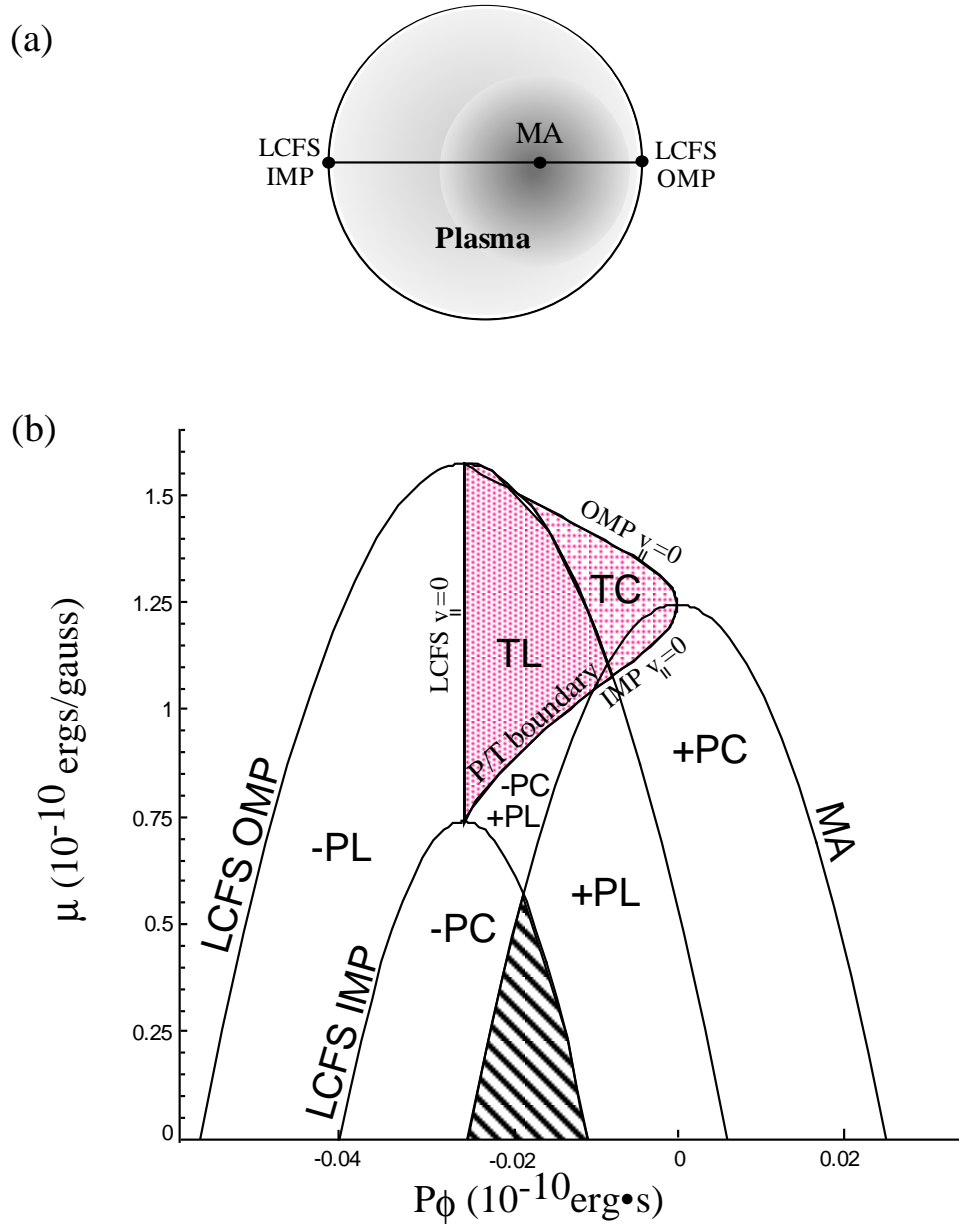


Figure 2.2: (a) Real (R, Z) space defining the plasma magnetic axis (MA) the inner and outer midplane points (IMP and OMP) of the Last Closed Flux Surface (LCFS). (b) (μ, P_ϕ) space calculated for 3.5 MeV α -particles in an $R=2.6$ m, $I_p=1.4$ MA discharge. The plasma boundary is described by the fixed (R, Z) parabolas corresponding to the points shown in (a). These 3 parabolas, along with the $v_{\parallel}=0$ along the midplane and LCFS curves, which enclose the shaded trapped particle region, make up the boundaries that delineate orbit types designated by a 3 character code: $+(-)$ = co-(counter-)going; $P(T)$ = passing(trapped); $C(L)$ = confined(lost).

α -particle's (μ, P_ϕ) lies within the trapped region, then the parabola with its apex ($v_{\parallel} = 0$) at this (μ, P_ϕ) point is allowed, and the orbit can transition smoothly from being on the counter-going side of a parabola (i.e. left side) to the co-going side and is thus a trapped particle. However, if the α -particle's (μ, P_ϕ) lies below the trapped region, then this point is constrained to remain on one side of all the parabolas in the orbit's collection, since the apex of a parabola can not pass through this point, and is thus a passing particle, the direction of which depends on which side of the parabolas the (μ, P_ϕ) point sits on. When the LCFS coincides with the RF limiter radius (e.g. full bore R=2.62 m plasmas in TFTR), an orbit is considered first orbit lost (Sec. 2.3.1) if the apex of any of the parabolas in its collection reach the LCFS $v_{\parallel} = 0$ line. For smaller minor radius plasmas in which the LCFS still intersects the IMP point at the wall (i.e. the bumper limiter in TFTR), the parabola corresponding to the OMP point at the wall defines the new loss boundary for high energy trapped and co-going α -particles.

This constants of the motion space provides a convenient description of α -particle orbits by allowing all orbits at a given energy to be represented in a two dimensional space. Changes in orbit classifications can be quantified by examining shifts in α -particles' (μ, P_ϕ) or shifts in the orbit classification boundaries themselves due to a change in alpha energy or changes in the magnetic topology. This formalism will be used in the analysis of chapter 5.

2.3 Classical Alpha Loss

Classical losses are determined by the unperturbed magnetic field geometry of the tokamak and can be calculated by following individual particle orbits numerically. Classical losses include first orbit loss, and the TF ripple induced losses.

2.3.1 First Orbit Loss

First orbit loss, the simplest loss, results from particles being born on orbits that intersect the wall on their first bounce (i.e. before completing a poloidal transit). First orbit loss consists of particles born in the loss regions shown in Fig. 2.2 (i.e. +PL, -PL, TL). These particles are lost with very nearly their birth energy since the time for one bounce ($< 10 \mu\text{s}$) is much less than the collisional slowing down time ($\tau_{sd} \approx 200 \text{ ms}$ energy e-folding time) [8] and are thus also known as ‘prompt’ loss. Hence, the energy of first orbit lost particles is $\approx 3.5 \text{ MeV}$ with a Doppler spread of up to $\sim \pm 0.5 \text{ MeV}$ caused by the beam-target and beam-beam reactions [9, 5].

This prompt loss follows the neutron source rate very closely in time since for each neutron produced by fusion, an α -particle is also produced. Escaping alpha flux levels can be calculated from a knowledge of the current (or equivalently, q) and fusion source profiles. The global fraction of particles that are first orbit lost decreases with increasing plasma current. This is due to the reduced banana widths of trapped particles in a magnetic geometry with higher rotational transform and hence less overall drift, resulting in a particle staying closer to a given flux surface and thus farther from the walls. Global losses in TFTR can vary from 3% of the total source rate at $I_p = 2.7 \text{ MA}$ to $\sim 50\%$ at $I_p = 0.6 \text{ MA}$ [10].

2.3.2 TF Ripple Induced Loss

The need for access to the plasma for diagnostics and external heating and fueling sources, such as NBI, necessitates the use of a finite number of discrete toroidal field (TF) coils. TFTR has 20 such TF coils. This results in a rippling of the toroidal field that is most pronounced at the outer midplane. This ripple is responsible for two types of alpha loss, ripple well trapping and stochastic ripple diffusion.

Ripple Well Trapping

Ripple well trapping occurs when particles become mirror trapped in the magnetic ripple wells that form between TF coils [11]. These particles are quickly lost to the first wall because the vertical drift is not compensated by the rotational transform of the magnetic field lines. Their orbits, known as ‘superbananas’, have a pitch angle ($\chi = \cos^{-1}v_{\parallel}/v$) very close to 90° and drift vertically downward only ~ 0.1 cm per gyro-orbit. This makes their detection difficult, requiring a collection aperture very close to the tip of a probe to avoid scraping them off on the probe itself. For this reason, this type of loss has not been experimentally verified in TFTR. It is, however, expected to be a small loss channel, since the alpha source rate is small at the outer midplane where the ripple is most pronounced, and only a very small fraction of the alphas in this region occupy the portion of phase space corresponding to ripple trapping. It can, however, be coupled to other loss mechanisms, such as TAE induced loss (Sec. 2.4.2), causing it to be ‘fed’ to produce enhanced losses.

Stochastic Ripple Diffusion

Stochastic ripple diffusion (SRD) [12] is a process by which trapped particles, with their banana tips within a threshold region, can diffuse to the wall due to stochasticity brought on by the TF ripple. Passing orbits average out the magnetic field line perturbations brought on by the TF ripple. Trapped particles, however, only sample a portion of the TF ripple perturbation near their banana tips. Stochasticity is then brought on by the toroidal drift that banana orbits experience (or by collisions) which acts to randomize the amount of ripple perturbation sampled at each banana tip. The result is a random jump near each banana tip in the vertical direction to conserve μ . The step size in TFTR is generally on the order of ~ 1 cm, resulting in a loss process that is relatively fast compared to slowing down, so that these particles are lost with nearly all of their birth energy. This loss process corresponds to trapped confined (TC) particles crossing the trapped confined/lost boundary (i.e. the portion of the OMP LCFS parabola in the trapped region of Fig. 2.2) to the left as the particles’ P_ϕ decreases while μ and E are conserved.

As SRD particles diffuse outward in minor radius (from source to sink), the first place they hit the wall is at the outer midplane. For instance, the closet point of approach to the wall for the trapped orbit of Fig. 2.1 is at the midplane. For this reason, SRD loss tends to concentrate within 30° of the outer midplane. Simulations show that 5%–15% of alphas are lost through SRD at 1.0–2.0 MA and $R = 2.52$ m [13]. SRD is expected to be the dominant classical loss mechanism for alphas at high current in TFTR ($I_p \geq 1.5$ MA) [14].

2.4 Nonclassical Alpha Loss

Other than classical losses result from varying perturbations such as small scale electric fields (collisions), perturbed magnetic field lines (MHD), and those due to interaction with RF waves.

2.4.1 Collisional Nonprompt Loss

Collisional loss results from the pitch angle scattering of marginally passing α -particles across the passing/trapped boundary as they slow down, causing these particles to be nonpromptly lost. Normally, the 90° pitch angle scattering rate is much smaller than the slowing down rate for energetic ions. Particles very close to the passing/trapped boundary, however, only need a small amount of pitch angle change to be scattered into the prompt loss region. Since the small angle pitch angle scattering rate is much larger than the 90° rate, these particles can scatter across the boundary in the process of slowing down. Hence, this process establishes a partially depleted boundary layer in phase space near the passing/trapped boundary in which the α -particle distribution function decays to zero at the boundary. The slope of this distribution function should lead to a diffusive flux of particles across the boundary. This loss is expected to be small in comparison to the usual first orbit loss. For instance, an analytical calculation of Ref. [15] predicted a collisional loss of $\sim 1.3\%$ in a 1.65 MA

TFTR supershot, while a TRANSP [16] calculation, which did not include TF ripple, predicted a $\sim 0.3\%$ nonprompt loss and a total prompt and nonprompt loss rate of $\sim 10\%$ using the same parameters.

2.4.2 MHD Induced Loss

Magnetohydrodynamic (MHD) instabilities act to perturb magnetic field lines and hence also perturb the α -particle orbits passing through them. In general, MHD modes are thought to give α -particles a radial kick, causing a decrease in P_ϕ while conserving μ . This can allow previously confined passing particles to cross the passing/trapped boundary in Fig. 2.2 and become lost on large banana orbits. In a similar fashion, MHD can ‘feed’ other loss channels, such as SRD. MHD modes of any type, whether pressure driven, current driven, or kinetic, can cause loss [17].

With the introduction of tritium, the possibility of alpha driven collective effects arises. A collective instability requires a sufficient population of fast ions such that the ions themselves drive MHD modes. It has been determined that the observed alpha loss in TFTR does not depend on the fusion power level. This indicates that alpha driven collective instabilities either do not or are too weak to induce alpha particle loss in TFTR [9].

A collective instability, the toroidicity-induced Alfvén eigen (TAE) mode, has been observed in TFTR to be driven by NBI ions, ICRF H-minority tail ions, and more recently by α -particles following the end of NBI [18]. However, none of the alpha loss measurements made during these discharges indicate that these modes induce α -particle loss. Simulations have, however, shown that TAE modes can transport energetic ions into the ripple trapping region where they are quickly lost to the bottom of the vessel. It has been determined that this synergistic effect was responsible for a melted weld that resulting in a vacuum leak on TFTR [19].

2.4.3 RF Induced Loss

Radio frequency (RF) waves can interact with high energy ions to put them onto loss orbits [20]. As is the case with MHD-induced loss, RF acts to push fast ions in phase space into existing loss cones, e.g. first orbit or SRD. RF waves, however, can change all three constants of the motion, E , μ , and P_ϕ [17]. The interaction between fast ions and RF occurs when the wave-particle resonance condition is satisfied,

$$\omega_{RF} = \Omega_f(R) - k_{\parallel}v_{\parallel f} \quad (2.7)$$

where ω_{RF} is the applied rf frequency, $\Omega_f(R)$ is the fast ion cyclotron frequency, k_{\parallel} is the parallel wave number, and $v_{\parallel f}$ is the fast ion parallel velocity. The large value of $v_{\parallel f}$ allows fast ions to interact over a much larger resonance region than do thermal ions. RF interactions with α -particles may play an important role in ‘helium ash removal’ and ‘alpha channeling’ (Sec. 1.1).

2.5 Previous Experimental Results

Previous measurements of escaping alphas have been made in TFTR using the lost alpha scintillator detectors. These detectors are briefly summarized in Sec. 2.5.1, and the previous DD and DT results obtained using these detectors are summarized in Sec. 2.5.2 to provide a starting point for this thesis.

2.5.1 Lost Alpha Scintillator Detectors

Four scintillator detectors are installed on TFTR to detect fusion product losses to the wall [21, 22]. While these detectors were designed to detect alpha particles, they are also capable of detecting the ‘alpha-like’ DD fusion products (i.e. 3 MeV proton and 1 MeV triton). These detectors are installed at various poloidal angles below the outer midplane (20, 45, 60 and 90°) and are all at the same toroidal angle.

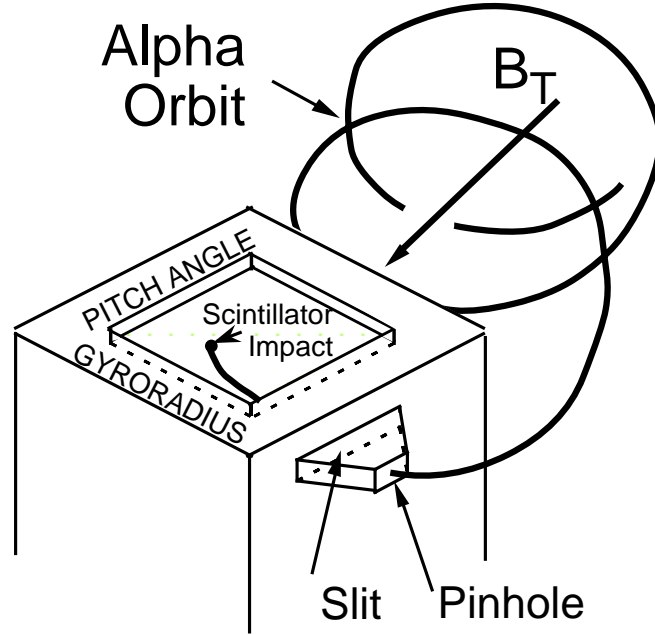


Figure 2.3: Schematic diagram of the lost alpha scintillator detector located 90° below the outer midplane. The escaping alphas enter a pair of apertures that disperse them in pitch angle and gyroradius. The 2-D image of the visible light emission from the scintillation screen is transmitted through a quartz fibreoptic bundle to a gated intensified video camera for analysis.

As illustrated in Fig. 2.3 each detector consists of a pinhole and slit collimator designed to disperse fusion products along a rectangular scintillator according to gyroradius, ρ , (depending on their energy) in one dimension and pitch angle, χ , (depending on their magnetic moment) in the other. The visible light from ion impacts on the scintillator is imaged onto a shielded charged coupled device (CCD) camera and a series of photomultiplier tubes (PMTs). A detector analysis code determines a (ρ, χ) grid that is used to interpret the camera images. For this grid, the ρ coordinate is the centroid of the predicted scintillator impacts for an ion of gyroradius ρ_0 (the gyroradius the ion would have if all its energy were put into perpendicular motion, i.e. at $\chi = 90^\circ$) and the χ coordinate is the orbit's toroidal pitch angle, χ_t , measured locally with respect to the co-going toroidal field direction at the detector. Specifics on the design and use of the lost alpha scintillators can be found in Refs. [9, 22].

2.5.2 Summary of Previous TFTR Results

The escaping alpha measurements contained in this thesis were all made at the bottom of the TFTR vessel (i.e. 90°) in MHD quiescent DT plasmas without RF. All previous observations of alpha loss to the 90° scintillator detector in MHD quiescent DT plasmas without RF have been consistent with the classical ‘single particle’ first orbit loss process [9]. There have been no signs of any collective α -particle loss processes up to the maximum fusion power level of 10.7 MW. The alpha loss to the 45° and 20° detectors was not consistent with the first orbit loss model alone, perhaps owing to the additional effects of TF ripple induced loss.

Previous measurements of charged fusion product loss to the 90° scintillator detector in DD plasmas, however, were not fully consistent with just first orbit loss. At small major radii ($R \leq 2.52$ m) and high plasma current ($I_p \geq 1.4$ MA) an additional anomalous ‘delayed’ loss was seen. This loss feature, which is not understood, will be examined in greater detail in Sec. 4.4.2.

Chapter 3

Alpha Collector - Description

3.1 Introduction

TFTR has previously relied on the lost alpha scintillator detectors (Sec. 2.5.1) as the sole escaping alpha diagnostic. In order to provide a complementary measurement of escaping alphas, a new alpha collector sample probe [23, 24] has been developed. The alpha collector probe operates on an entirely different physical principle, i.e. the implantation and subsequent trapping of alpha particles in nickel foils [25]. This detection technique offers several improvements over the scintillator method. In particular, the primary reasons this detection technique was selected are:

1. for improvement of the energy resolution with respect to the lost alpha scintillators;
2. for its inherent ease of absolute calibration, allowing a valuable cross calibration for the lost alpha scintillators and validation of alpha loss models;
3. for its immunity to high neutron fluxes, which may prove useful in ITER and future DT reactors.

A general overview of the detection technique is described in Sec. 3.2. The specifics of the probe head design and many of the factors that drove design choices are presented in Sec. 3.3. The sample analysis method used to measure helium content in individual nickel foils is covered in Sec. 3.4. The geometry of the alpha collector with respect to components and α -particle orbits within TFTR is discussed in Sec. 3.5, and finally, the alpha collector is compared and contrasted to the lost alpha scintillator detectors in Sec. 3.6.

3.2 Detection Technique

The alpha collector probe [23, 24] is based on the foil deposition technique originally proposed by Langley [25]. Similar methods have been previously used on TFTR to

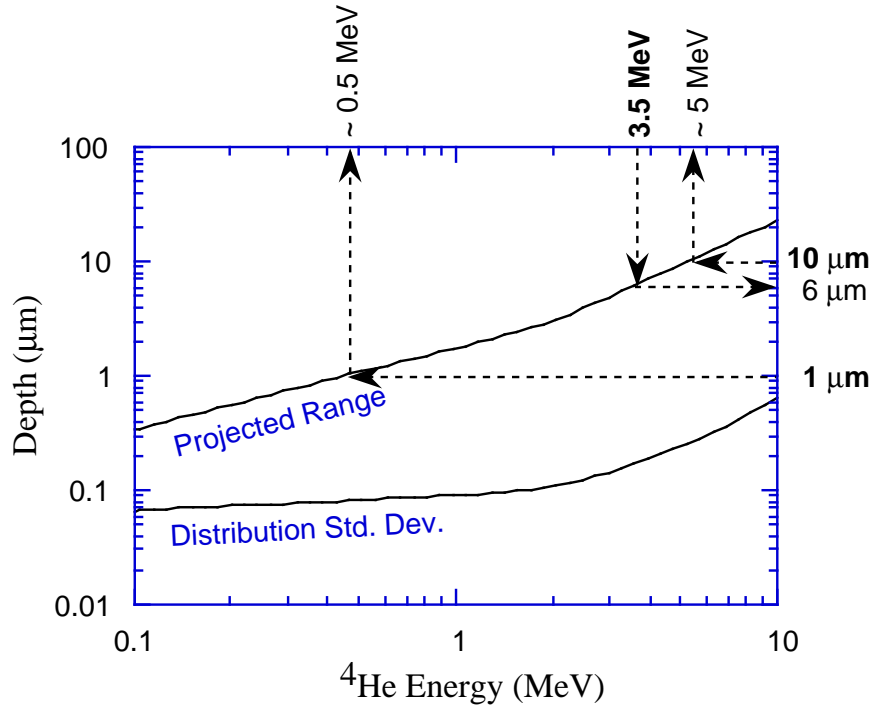


Figure 3.1: *Projected implantation range and standard deviation (straggling) for ^4He implanted into nickel. Birth energy alphas at 3.5 MeV travel $\sim 6 \mu\text{m}$. Energy detection range for 1–10 μm of nickel is ≈ 0.5 –5.0 MeV. (Taken from Ref. [29])*

collect DD fusion produced tritons [26], and on the Joint European Torus (JET) to collect ^3He ions accelerated by ICRH [27, 28]. In the current TFTR implementation of this technique, escaping alpha particles whose trajectories intercept the detector are implanted into a stack of nickel foils consisting of ten layers of 1 μm thick foil. This is sufficient to stop DT fusion alphas at 3.5 MeV, which have a projected penetration range of 6 μm in nickel [29] as seen in Fig. 3.1. The alpha particles form a distribution of implantation ranges in the foil stack that is dependent on their incident angles and energies. Once the alphas are stopped in the Ni, they are trapped and remain immobile as long as the Ni remains below a critical temperature of $\sim 400^\circ\text{C}$ [30, 31].

The foils are removed from the TFTR vacuum vessel after exposure to the alpha flux of one or more discharges. They are then analyzed for He content by melting the foils one at a time in an off-site vacuum chamber (located at the University of Toronto), thus releasing the He, and then measuring the partial pressure of He with

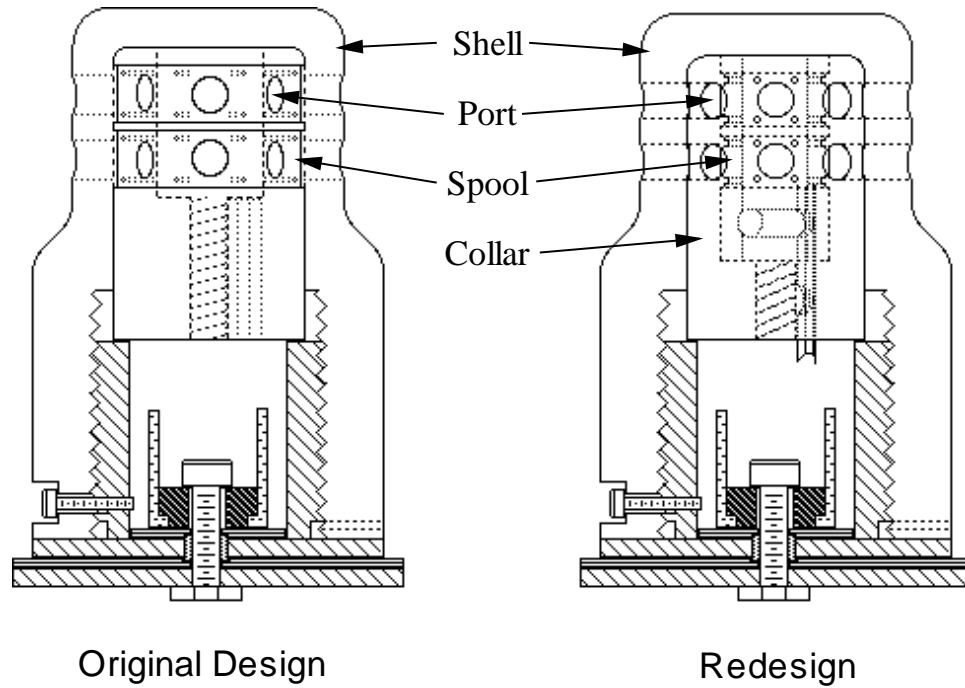


Figure 3.2: (a) Original design and (b) redesign of alpha collector probe head. Head consists of outer shell which houses $1/4$ in deep collimating ports, inner spool on which the nickel foils are wrapped, collar in the redesign shown in (b) which extends the collimating ports to $1/2$ in, and supporting components to provide electrical isolation and mount to TFTR bottom probe located in bay-D.

a Residual Gas Analyzer [23, 32]. The alpha energy spectrum is then inferred from the range distribution of He in the Ni foil stack. Calibration implants of known energies and total fluences (Sec. 3.4.2) have been used to check the accuracy of the implantation model (Sec. 4.2) and sample analysis method (Sec. 3.4.1).

3.3 Probe Head Design

The two alpha collector probe head designs used are shown in Fig. 3.2. Feature dimensions for the original design are specified in Fig. 3.3. The probe head consists of nickel foils held by a spool piece which is inserted into a shell. The shell is made of a 4D

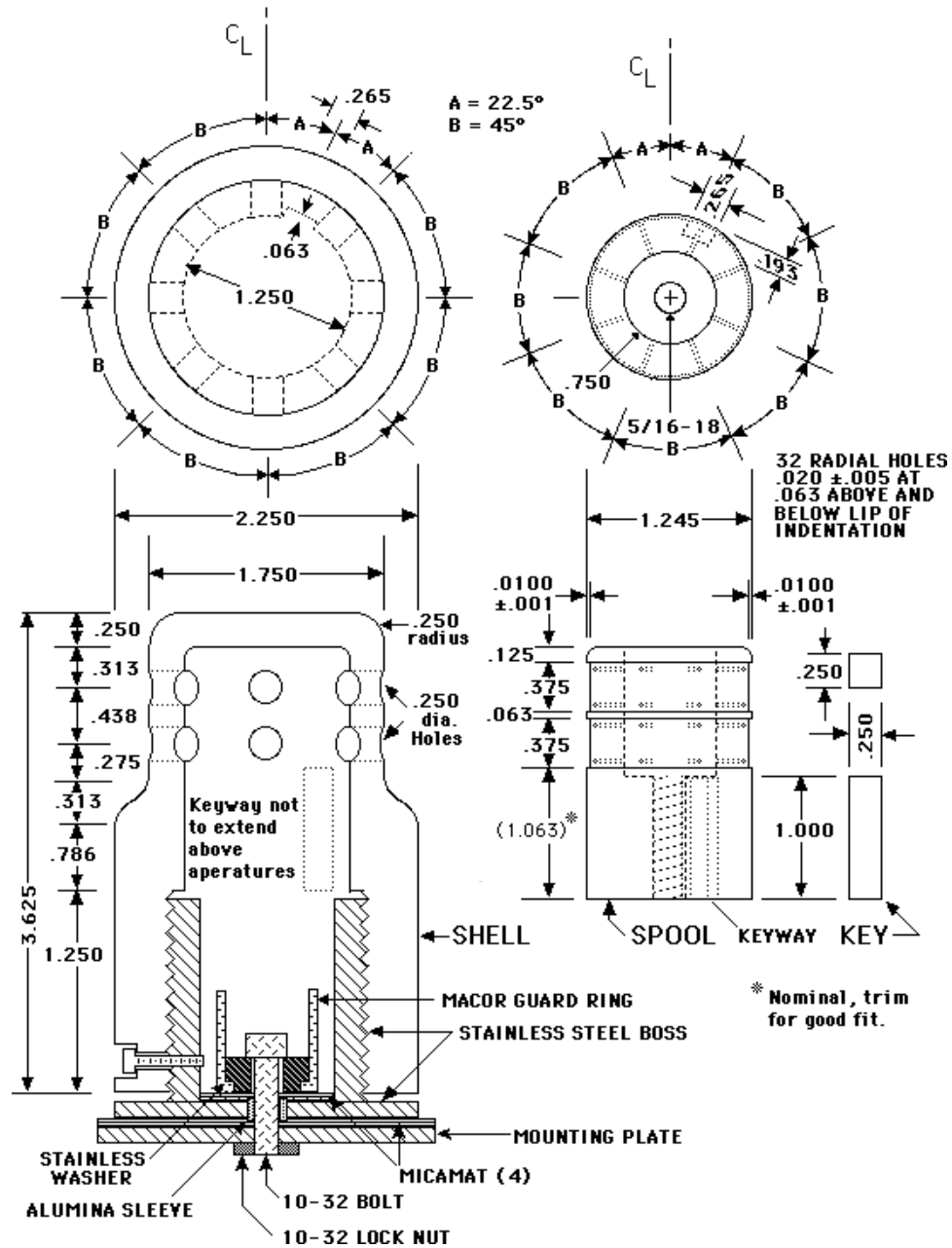


Figure 3.3: Top and side view schematics of components included in original design of the alpha collector. Dimensions are inches.

weave carbon-fiber-composite chosen for its superior thermal and structural properties, and made of carbon for its low atomic number (Z). Low Z materials are preferred for use as plasma facing components since the power lost due to Bremsstrahlung radiation is proportional to the effective atomic number of the plasma (Z_{eff}). Z_{eff} increases dramatically if high Z impurities enter the plasma through plasma erosion of wall components.

Two rows of 0.635 cm (1/4 in) diameter collimating ports, for α -particle pitch angle selectivity, are drilled into the 0.635 cm wall of the shell. Each row of collimating ports has eight evenly spaced ports placed 45° apart. The spool is made of graphite and the shell and spool are supported and electrically isolated from the tokamak by the mounting components seen in Fig. 3.2. Two nickel foil stacks are wrapped around the cylindrical spool which is inserted into and keyed to the shell.

The redesign of the probe head shown in Fig. 3.2(b) was prompted by the need to reduce foil heat damage from neutral beam ion loss as will be discussed in Sec. 4.3. The primary change was an extension of the collimating port depth by drilling 0.635 cm holes through the original spool design (labeled as the Collar in Fig. 3.2(b)). This collar is then modified to fit a new smaller spool inside of it. So the original design has ports of 0.635 cm in width (w) and depth (d), whereas the redesign has $w = 0.635$ cm, but has twice the port depth at $d = 1.27$ cm (1/2 in). These port dimensions allow high energy particles (i.e. $\rho \gg w, d$) with trajectories within $\pm 45^\circ$ of a port's axis to strike the foils in the original design, but an acceptance range of only $\sim \pm 27^\circ$ for the redesign, which improved the pitch angle resolution.

The choice of nickel as the implantation foil was based on the immobile character of He in Ni at temperatures below $\sim 400^\circ\text{C}$ [30, 32]. The Ni foil, acquired from Goodfellow Corporation, has a 99.95% purity rating and a $\pm 10\%$ thickness accuracy as determined by weight. As depicted in Fig. 3.4, a foil stack is prepared by folding a 10 cm \times 10 cm sheet of 1 μm Ni foil 9 times to form a 10 cm \times 1 cm strip consisting of 10 layers. The foil is folded in a 'rolled' fashion, rather than an 'accordion' fashion, to limit the amount of tritium that can diffuse to the inner layers during exposure to a DT plasma. Tritium adhering to the foil surfaces can present a radioactive contamination problem once the foils are removed from the probe. In the event that the outer layers

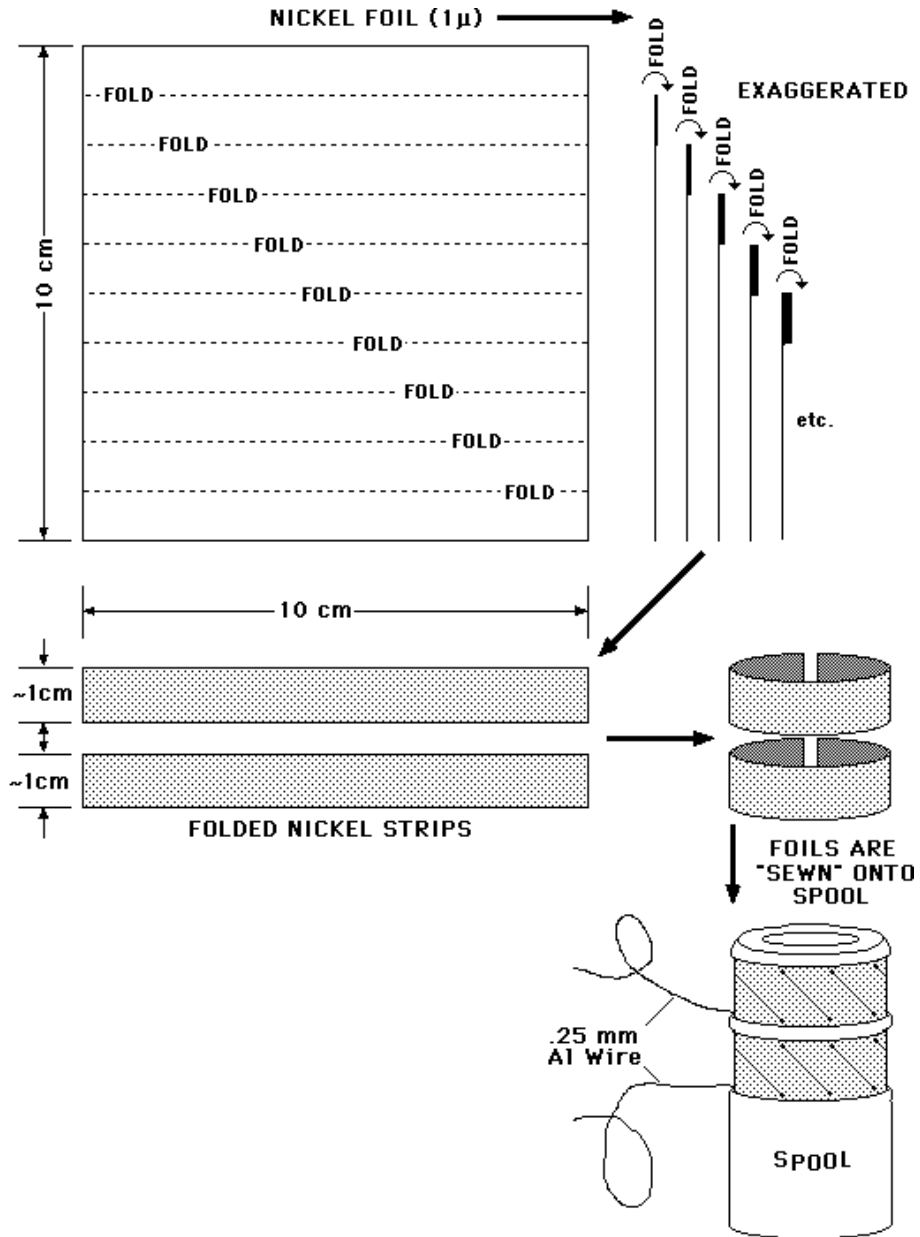


Figure 3.4: Nickel foils are 'rolled' to produce two 1 cm \times 10 cm strips of ten layer stacks which are wrapped and 'sewn' onto the spool prior to being inserted into the alpha collector probe head.

of the rolled stack (layers 1 and 10) are overly contaminated with tritium they can be removed and discarded. The remaining layers can then be surveyed for tritium contamination and decontaminated to acceptable levels (Sec. 3.4.3).

The Ni foil stack is wrapped around and ‘sewn’ onto the spool using 0.25 mm aluminum wire and the overlapping ends of the Ni are spot welded together. The Al wire holds the Ni tightly to the graphite spool, improving the thermal contact between the Ni and the spool, allowing the spool to act as a heat sink. The 660°C melting point of Al enables the wire to also act as a temperature indicator. If the Al wire exposed in a collimating port experiences any melting due to heat flux from a plasma discharge then it is assumed that the Ni foil in that port exceeded 400° C and the implanted He sample is no longer a reliable indicator of escaping α -particles.

The range of 3.52 MeV birth energy α -particles in Ni is seen in Fig. 3.1 to be 6.0 μm . The standard deviation of the depth distribution, or straggling, is 0.15 μm for alphas at this energy. Removing the first layer results in a lower energy limit of about 0.5 MeV. The collimating effect of the port results in most particles implanting into the foils at near normal incidence. For collimating ports of equal depth and diameter whose dimensions are much less than the gyroradius of an alpha, the straggling of the range distribution is broadened in the direction of reduced depth by $\sim 10\%$ due to alphas implanting at less than normal incidence.

The choice of 1 μm Ni foils arranged in a stack and collimating ports of equal depth and diameter should result in the ability to resolve between the first orbit alpha loss at 3.52 MeV, which should be implanted in the sixth and seventh layers of the foil stack, and other losses at energies below about 2.8 MeV, which would be implanted in the fifth and shallower layers. This results in an energy resolution of about $\sim 20\%$, a significant improvement over the $\sim 50\%$ resolution of the scintillator detectors [8].

3.4 Sample Analysis

3.4.1 Thermal Desorption Spectrometry

The sample analysis method is based on thermal desorption spectrometry (TDS) using resistive heating of the samples and a UTI 100C residual gas analyzer (RGA), consisting of a quadrupole mass spectrometer with an electron multiplier, for He detection. The sample analysis system was developed and operated at the University of Toronto's Institute for Aerospace Studies in collaboration with PPPL.

The sample analysis vacuum chamber, illustrated in Fig. 3.5, is pumped down to $\sim 10^{-5}$ torr, as measured by the ion gauge, using the combination of a mechanical roughing pump and a turbo pump. A baking jacket is placed over the vacuum chamber and baked at 150°C for 24 hours to drive gases out of the walls and components of the system. This bake also drives deuterium out of the Ni foils which would otherwise corrupt the measurement since deuterium has the same charge to mass ratio as ^4He . This bake is conducted at sufficiently low temperature to ensure that the implanted He remains immobile in the Ni.

The system vacuum is improved further to a base pressure of $\sim 10^{-9}$ torr with the aid of a titanium sublimator and a liquid nitrogen cold finger. The titanium sublimator only getters out reactive gases and so has no effect on the He concentration. Most gases are condensed onto the surface of the cold finger, particularly methane which may be present in significant quantities but is not removed by the sublimator. The cold finger also has no effect on the He concentration due to the low boiling point of He. The effectiveness of the bake and titanium sublimator were tested by analyzing a foil sample implanted with $\sim 10^{16}$ deuterium atoms, over 7 orders of magnitude above the minimum sensitivity of the sample analysis system of 5×10^8 atoms. This test resulted in no mass-4 signal being detected by the RGA, meaning the deuterium had been effectively removed.

Each of ten tantalum foil strips is folded in half to form a pocket which holds a Ni foil sample corresponding to a specific collimating port and layer depth. Attached

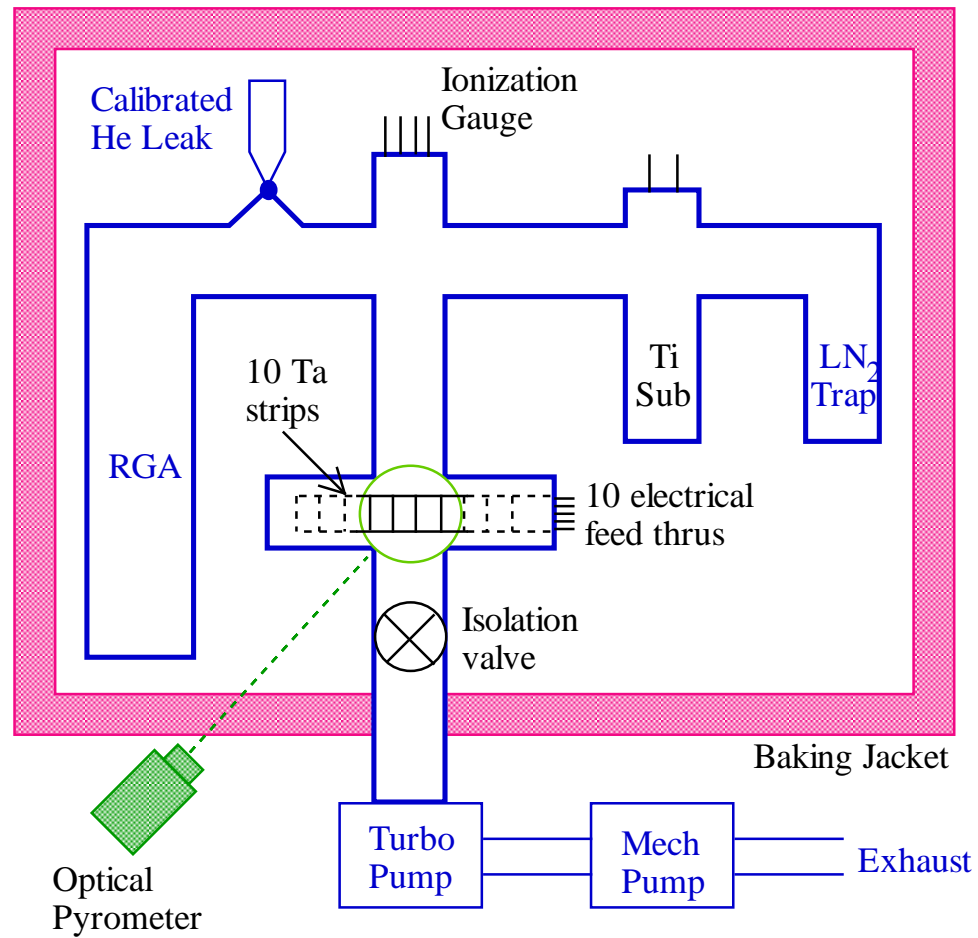


Figure 3.5: Sample analysis system used to desorb and measure He from nickel samples.

to one side of each tantalum holder is an electrical lead that penetrates the vacuum vessel through a vacuum sealed electrical feedthrough. The other side of each holder is grounded to the vessel. One at a time, a current of ~ 30 A is passed through each tantalum holder, resistively heating it to $> 1700^\circ\text{C}$ as measured with an optical pyrometer viewing the holders through a vacuum window. Nickel, with a melting point of 1453°C , quickly melts releasing the implanted He to the vacuum chamber which has been isolated from the pumps by shutting the isolation valve. The ^4He signal of the RGA is then recorded by an interfaced PC. Between each foil analysis the valve is opened to allow the pumps to remove the He in the system from the previous sample. The RGA output is calibrated before and after the analysis by introducing He into the system at a known rate using a calibrated He leak.

TDS was chosen over other surface sample analysis methods for its ability to achieve excellent minimum sensitivity. The system used was capable of detecting He levels as low as 5×10^8 atoms in the ~ 1 liter vacuum system. By desorbing all the He contained within the $1 \mu\text{m}$ thick foil, in essence integrating all the He contained within a $\sim 3 \times 10^{-5} \text{ cm}^3$ volume, a minimum He concentration of $\sim 2 \times 10^{13} \text{ atoms cm}^{-3}$ was detectable, roughly two orders of magnitude smaller than expected concentrations based on first orbit loss modeling (Sec. 4.2). By comparison, the secondary-ion mass spectrometry (SIMS) system used to measure ^3He and ^4He ions heated by ICRH in JET, achieved a sensitivity of only $5 \times 10^{18} \text{ atoms cm}^{-3}$ [28], about three orders of magnitude higher than levels expected for alpha collector samples.

Resistive heating of samples was chosen for its simplicity, trading off the ability to process large numbers of samples in a single batch. To ensure good minimum sensitivity, the main concern in choosing a desorption method was minimizing vacuum system volume to be able to maximize the partial pressure of released He. Systems using external heating sources, such as lasers or flash lamps, that could process on the order of 100 samples in one analysis run were considered. However, instead of minimizing vacuum volume by using an external heating source, it was decided to limit the number of samples in a batch to 10 to allow use of a 10 pin electrical feedthrough to provide the resistive heating current.

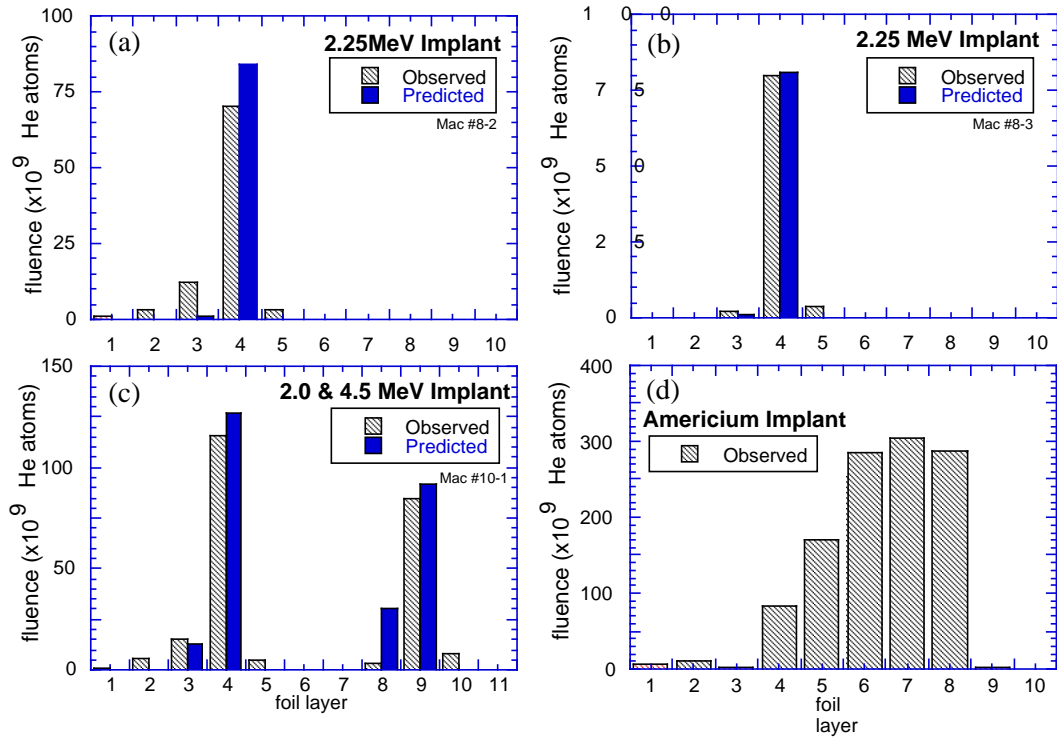


Figure 3.6: Calibration samples implanted at McMaster University’s Van de Graaff accelerator with monoenergetic He beams at (a) and (b) 2.25 MeV; (c) 2.0 and 4.5 MeV; and (d) calibration sample implanted using ^{241}Am 4.5 MeV alpha source.

3.4.2 Absolute Calibration

For use as a check of the absolute calibration of the sample analysis, calibration samples were prepared at McMaster University using a Van de Graaff accelerator [32]. Monoenergetic beams of He ions were implanted at normal incidence into stacks of $1\ \mu\text{m}$ Ni foils. These samples were then analyzed using the method described in Sec. 3.4.1. Figs. 3.6 (a) and (b) show the depth distributions for two Van de Graaff calibration samples at 2.25 MeV. Rutherford backscattering was used to accurately measure the total fluence implanted. IBM’s Monte Carlo TRIM-95 code that calculates the penetration of ions into solids (Sec. 4.2.2) was used to calculate the predicted depth distribution. Good agreement was found between the observed and the predicted distribution. Slight spreading of the distribution, such as in Fig. 3.6 (a) was attributed to nonuniformities in the foils. Fig. 3.6 (c) shows acceptable agreement

between predicted and observed depth distributions for a single foil sample with two separate implants at 2.0 and 4.5 MeV.

As another check of the absolute calibration, a foil stack was implanted using an Americium-241 alpha source. The source was an Amersham International AMRQ7779 sealed ^{241}Am 4.5 MeV alpha reference source containing 135 μCi of activity which emitted $\sim 10^6$ alphas/min $\cdot\mu\text{Ci}$ from the face of a 1 cm diameter circular foil. The source was placed over a 0.635 cm deep and 0.635 cm diameter collimator drilled out of an aluminum blank. A stack of ten 1 μm nickel foils was placed flat against the other side of the collimator. The source was left in place for 173 days, yielding a total predicted implanted fluence of $\sim 10^{12}$ alphas, in excellent agreement with the total measured He content of 1.2×10^{12} alphas. Taking into account the geometry of the source and collimator, the energy distribution of the source as a function of emission angle, and energy attenuation in air, the α -particle concentration was expected to peak in the 7th foil layer and to be distributed from the 4th to 8th layers. The measured depth distribution, shown in Fig. 3.6(d), is in good agreement with this prediction. This foil sample underwent the decontamination process described in Sec. 3.4.3 to ensure that the decon process would not interfere with implanted He levels.

3.4.3 Decontamination

Decontamination of the foils was necessary to avoid contaminating the sample analysis vacuum system with tritium that may have adhered to foil surfaces during exposure in TFTR. Initially, water soaked cotton swabs were used to wipe down the foils, but this proved to be insufficient. Several decon methods were considered including cleaning with a surfactant, baking, and ultrasonic bathing. Ontario Hydro Technology's Tritium Lab, having vast experience with tritium contamination, offered use of their decon expertise and facilities. Upon their suggestion, it was decided to bake the foils at 200°C under a flow of wet argon for 24 hours [33, 32]. Destructive testing of foil samples exposed to TFTR's DT environment, but not needed for He analysis, showed that this process removed over 90% of the tritium adhered to the foils. In addition,

the first layer, which was found to contain over 90% of the total tritium in a foil stack, was discarded.

The bake at 200° was conducted at low enough temperature to avoid the release of implanted He, which remains immobile below about 400°C. To ensure that the decon process did not cause desorption of He from Ni samples, the ²⁴¹Am calibration sample (Fig. 3.6(d)) underwent decon prior to being analyzed.

3.5 TFTR Implementation

Fig. 3.7 depicts a poloidal cross section of TFTR showing the exposure position of the alpha collector probe at the bottom of the vessel, and the poloidal projection of the RF limiters. TFTR has nine carbon poloidal RF limiters of varying poloidal extent to protect the RF launchers. They are centered at a major radius of 261 cm and have a minor radius of $99.0 \pm \sim 0.2$ cm.

After exposure to one or more discharges, the probe is lowered remotely and isolated from the TFTR vacuum vessel by shutting the torus interface valve shown in Fig. 3.7. The probe chamber can then be vented and the probe head removed through a six inch flange. The exposed nickel foils are then removed for analysis and replaced with new foils. Also shown in Fig. 3.7 are various α -particle orbits that strike the detector for a 2.45 m major radius plasma with a plasma current of 1.8 MA. These orbits will be discussed in more detail in Sec. 4.2.

Fig. 3.8 is a partial toroidal cross section of TFTR showing the position of the alpha collector with respect to the nearby poloidal RF limiters and the 90° lost alpha scintillator detector. The alpha collector and the lost alpha scintillator detectors are located in adjacent bays separated by one of the 20 toroidal field (TF) coils, placing them 18° apart toroidally. The major radii of the alpha collector probe and the 90° scintillator detector are 262.5 cm and 259.2 cm respectively, placing each of them within 2 cm of the major radius of the RF limiter center.

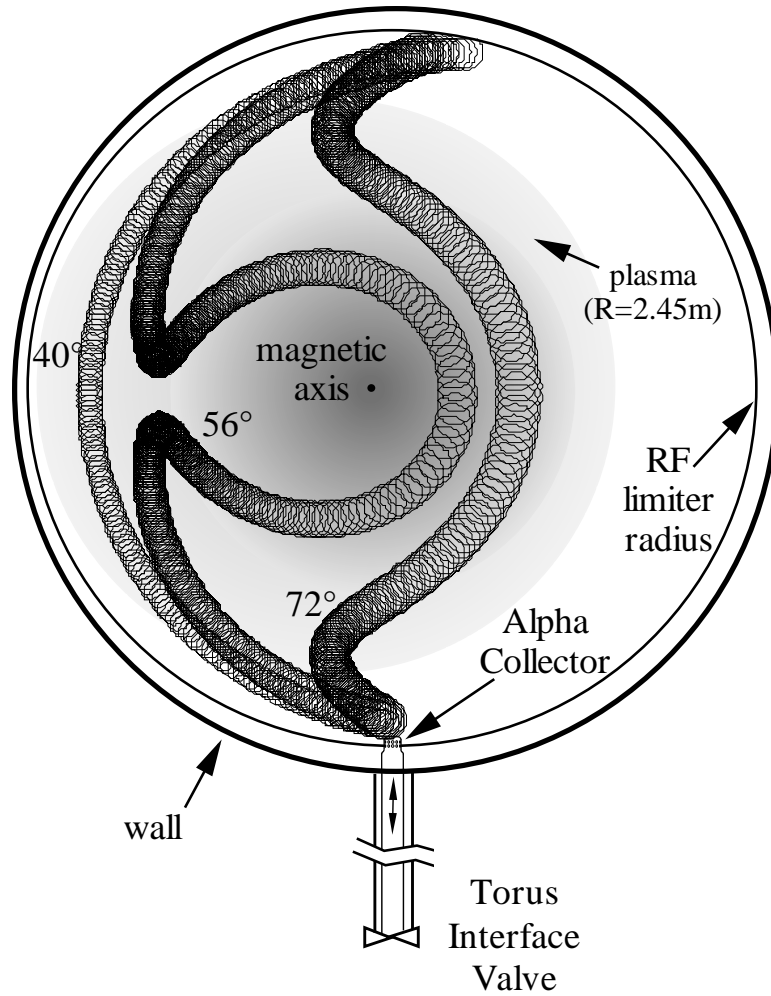


Figure 3.7: *Poloidal cross section of TFTR illustrating a co-going passing particle ($\chi_t = 40^\circ$, where χ_t is the toroidal pitch angle at the detector), a trapped particle at the fattest banana orbit ($\chi_t = 56^\circ$), and a deeply trapped orbit ($\chi_t = 72^\circ$) that strike the alpha collector probe located at the bottom of the vessel for a 1.8 MA plasma. Once exposed, the alpha collector is lowered below the torus interface valve so it can be isolated and removed.*

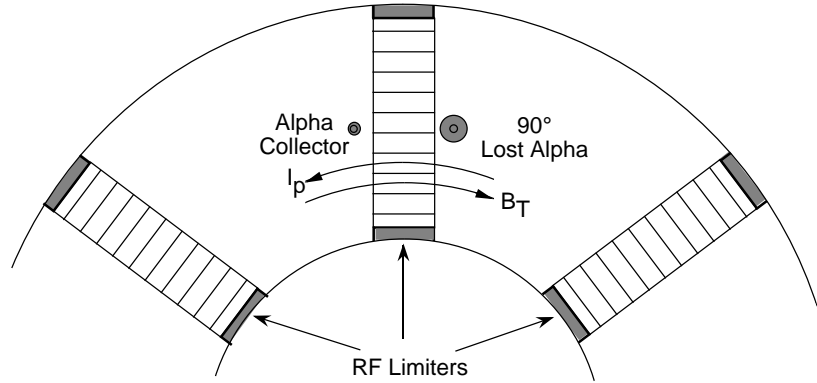


Figure 3.8: *Top view of TFTR vessel showing the relative locations of the alpha collector and the 90° lost alpha scintillator detector with respect to the nearest RF limiters.*

Particles intercepting the 90° lost alpha scintillator detector on co-going (in relation to the plasma current) orbits have 45° of toroidal clearance between the center of the nearest RF limiter and the detector. Particles intercepting the alpha collector on co-going orbits, however, only have 9° of toroidal clearance, making it necessary to position the probe closer to the plasma to avoid shadowing of these orbits by the limiter. This is essential for detection of first orbit loss since the majority of this loss occurs on the co-going leg of trapped banana orbits such as the 56° and 72° orbits depicted in Fig. 3.7. Orbits near the 56° ‘fattest banana’ dominate first orbit loss because they pass closest to the magnetic axis where the alpha source rate is peaked.

Fig. 3.9 shows the alpha collector and nearest RF limiter as seen when looking toward the center of the torus. This figure depicts a co-going alpha particle orbit entering a collimating port on the detector. Alpha particles can enter any one of a series of 16 collimating ports that are separated into two rows on the cylindrical probe head. At the back of each port is the 10 layer stack of 1 μm thick nickel foils into which the alpha particles implant. Each port only accepts particles within a particular range of pitch angles.

The edge of the probe and the RF limiter are separated toroidally by 12.4 cm.

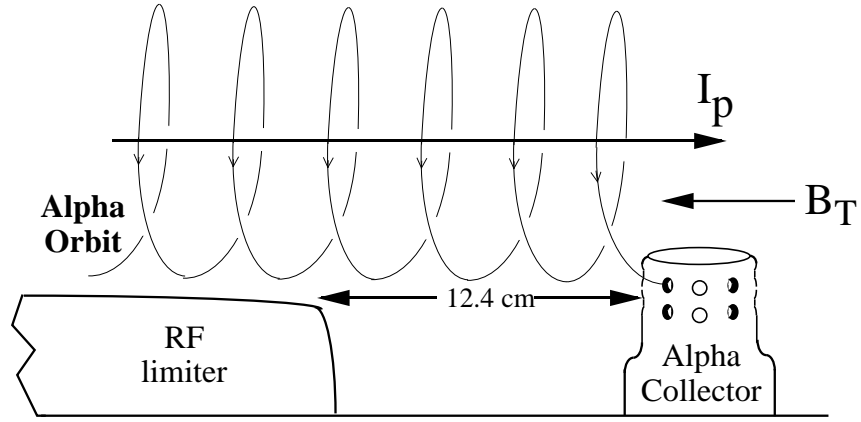


Figure 3.9: *Side view (looking in toward centerline of TFTR) of the alpha collector probe head depicting a co-going alpha particle entering one of the 16 collimating ports.*

The probe was placed in the same position for each exposure, placing the center of the upper row of collimating ports 0.5 cm radially inward from (i.e. above) the nearest limiter, and the lower row 0.6 cm radially outward from (i.e. below) the limiter. This was sufficient to avoid shadowing of first orbit loss at 3.5 MeV to both rows, as will be discussed in Sec. 4.3.4. The top of the lower row of collimating ports was only 0.3 cm below the RF limiter. The larger toroidal separation for co-going orbits between the nearest RF limiter and the 90° scintillator detector allows its 0.1 cm high pinhole aperture to be placed ~ 1.2 cm below the RF limiter [22], or ~ 0.9 cm below the top of the lower row of the alpha collector.

A cross section taken through the middle of a row of collimating ports is shown in Fig. 3.10(a) for the original design and Fig. 3.10(b) for the redesigned probe head. The orientation of each port is labeled in Fig. 3.10 with respect to the toroidal direction (0° corresponding to the collection of co-going particles). The redesigned head was rotated with respect to the original probe head by 7.5° clockwise when viewed from above. This was to line the probe head up with the scintillator detector which is oriented along 67.5° . For convenience, the orientations of the original design will be referred to when discussing the probe in general (subtract 7.5° to obtain the redesign orientations).

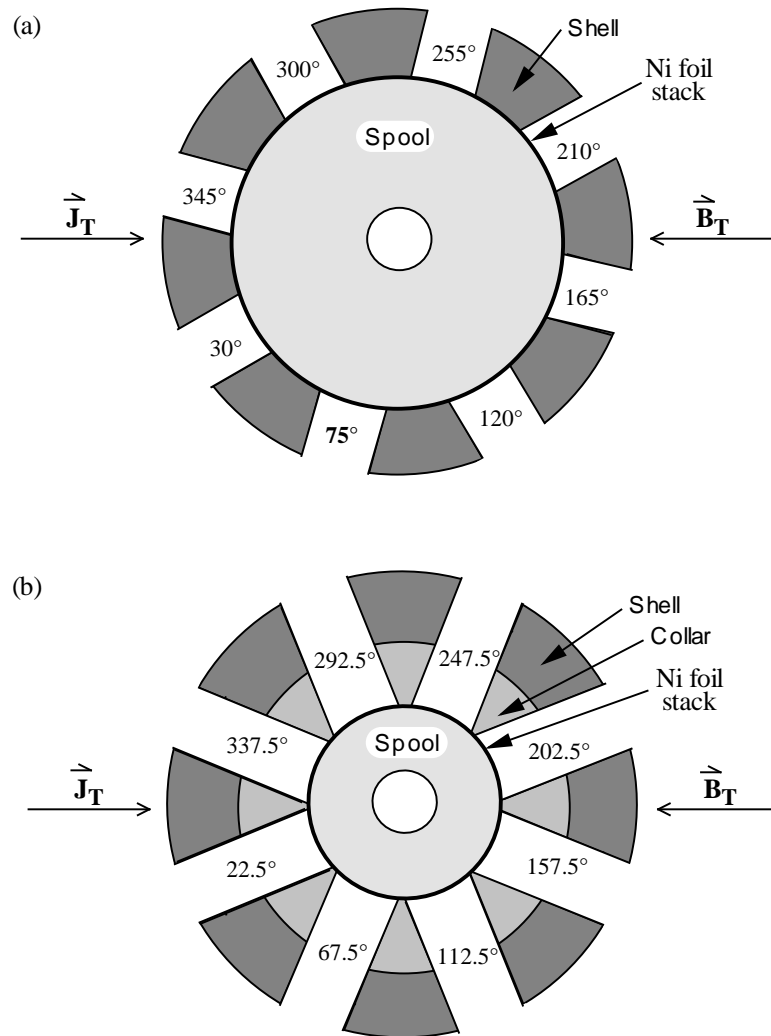


Figure 3.10: Midplane cross section of a row of collimating ports for the (a) original design and (b) redesigned alpha collector probe head. The stack of 10 layers of $1 \mu\text{m}$ Ni foil is wrapped onto the inner spool which is then inserted into an outer shell. Cylindrical 0.635 cm diameter holes drilled into the 0.635 cm thick outer shell make up the collimating ports. The collimator depth is extended to 1.27 cm in the redesigned head of (b) by inserting a cylindrical 0.635 cm thick collar that also has 0.635 cm diameter holes drilled into it. The spool diameters are (a) 3.175 cm and (b) 1.905 cm

<u>Advantages of Alpha Collector:</u>		
	<u>Scintillator</u>	<u>Collector</u>
A1. Energy Resolution	$\pm 50\%$	$\pm 20\%$
A2. Absolute Calibration	\sim factor of 2	$\pm 15\%$
A3. DT Noise Immunity	Fair	Good
A4. Positive Ion Identification	No	Yes
A5. Pitch Angle Coverage	40-80°	0-180°
A6. Radial Coverage	No	Yes
<u>Disadvantages of Alpha Collector:</u>		
	<u>Scintillator</u>	<u>Collector</u>
D1. Time Resolution	50 μ s	1s
D2. Real Time	Yes	No
D3. Access Required	No	Yes
D4. Pitch Angle Resolution	$\pm 3^\circ$	$\pm 45^\circ$
D5. Multiple Ion Detection	Yes	He ⁴ , He ³
D6. Passive Detection	Yes	Less passive

Table 3.1: Comparison of Escaping Alpha Diagnostics

3.6 Comparison to Lost Alpha Scintillator Detectors

The lost alpha scintillator detectors are described in Sec. 2.5.1. The alpha collector complements the lost alpha scintillator detectors in many ways. Each has its strengths and weaknesses. Table 3.1 summarizes the advantages and disadvantages of the alpha collector as compared with the scintillator detectors. The advantages of the alpha collector are:

- A1.** As discussed in Sec. 3.3 the alpha collector, in its current configuration, is capable of achieving 20% energy resolution, a significant improvement over the 50% resolution obtainable with the scintillator detectors. Further improvement in the energy resolution may be possible by using thinner Ni foils and higher degrees of collimation. The use of 1/4 μ m Ni foils and deeper collimating ports may allow an energy resolution limited by the straggling of the distribution to

$\sim 5\%$.

- A2.** Absolute calibration of the foil deposition method is inherently straightforward since it is possible to accurately determine the number of alpha particles implanted in the foils by measuring the partial pressure of ^4He in a closed volume in which the foils are melted. Due to a combination of several factors, including uncertainties in the light output per MeV ion, in the angular distribution of this light output, and in the optical throughput of the lenses and fiber bundles, the absolute calibration of the scintillator detectors for DT is uncertain by about a factor of ~ 2 [34]. Thus the foil deposition method should provide a valuable absolutely calibrated cross-check with these detectors and a means of validating alpha loss models.
- A3.** Since there are no optics nor electronics that can experience interference or degradation from high neutron fluxes, the foil deposition technique may prove more survivable than other detection methods in ITER and future DT reactors. Extensive efforts went into shielding the fiber optics, detectors (CCDs and PMTs) and associated electronics of the scintillator detectors on TFTR, resulting in a signal-to-background ratio slightly above unity [22]. It is not clear whether scintillator detectors can be designed to provide useful alpha loss information in the harsh neutron environment of a DT reactor such as ITER.
- A4.** The use of an RGA allows the positive identification of different ion species by means of mass spectrometry. Thus the sample analysis of the foil deposition method is capable of distinguishing between ^4He signals and those of the D-D fusion products, 3 MeV protons and 1 MeV tritons. Deuterium, which has the same charge to mass ratio as ^4He , but is not as immobile in Ni as He, is driven off the foils by the decontamination process and the low temperature bake ($< 200^\circ\text{C}$) so as not to be counted as He. The scintillator detectors, on the other hand, are unable to discriminate between high energy ions, leading to ambiguity when fusion products and other high energy ions exist in comparable quantities (e.g. during ICRH minority heating experiments).
- A5.** The alpha collector was designed to collect alphas over the full pitch angle range of $0\text{--}180^\circ$, with the exception of a small region ($\approx 8^\circ$) around 90° . Alphas with

a pitch angle $\approx 90^\circ$ are shadowed by the probe head itself, making detection of ripple well trapped particles (Sec. 4.5) unlikely. The scintillator detectors were designed such that they only cover $\sim 40\text{--}80^\circ$ in pitch angle, possibly missing important alpha loss features.

- A6.** The alpha collector was designed with two rows of collimating ports to provide radial dependence information of alpha loss. Also, being mounted on a movable probe enables a scan of radial position. The scintillator detectors contain only one collimating aperture, and, with the exception of the 20° detector, are mounted in a fixed position behind the RF limiter radius.

The advantages over the scintillator detectors made possible by the specific design of the foil deposition alpha collector (A1, A5 and A6) make it a particularly useful complementary escaping alpha diagnostic for TFTR. While some of the advantages can be lost through possible design changes of the scintillator detectors, advantages A2, A3 and A4 are inherent advantages of the alpha collector that may prove valuable in future DT reactors. Of course, there are also inherent disadvantages to the foil deposition detection method:

- D1.** The time resolution of this technique is inherently poor. The current detector foils must be exposed to a minimum of one TFTR shot, resulting in a time resolution on the order of one second. In a reactor operating in steady state it may be possible to design fast acting shutters over the collimators or moving foil samples at the back of collimators. The time resolution will be limited by the exposure time necessary to obtain a signal greater than the minimum sensitivity of the sample analysis. JET is attempting a similar foil stack diagnostic in which each of several electrically insulated layers are monitored in real time for charge collection, essentially making a stack of Faraday cups [35]. It may prove too difficult to overcome DT neutron electronic interference of a DT reactor with such a method, but if successful, it could overcome the next two disadvantages as well.
- D2.** A large turn around time is required to remove the foil samples from the tokamak and to analyze them. With the current probe, it is possible to change out

foils overnight in preparation for new exposures the next day. The process of shipping, decontaminating and analyzing the foils in Toronto limits the time to availability of data to a few weeks. While vast improvements are possible it is difficult to imagine a real time diagnostic using this technique.

- D3.** Removing and replacing the foils requires access to the TFTR test cell basement during machine down time to open a tritium contaminated system. A remote sample retrieval system allowing foil replacement during machine operations would be useful for ITER, but tritium contamination remains an issue.
- D4.** Pitch angle resolution of the alpha collector is determined by the geometry of the collimating ports, with deeper/narrower ports giving better resolution. In the current design, pitch angle resolution was traded off for total α -particle fluence to ensure measurable levels of He in the foil samples. As discussed in Sec. 3.3, the original design has a pitch angle acceptance range of $\pm 45^\circ$, while the redesign has $\pm 27^\circ$. This ensures overlapping coverage between adjacent ports which are separated by 45° . The pitch angle resolution is generally limited by this 45° spacing, although some tricks to get around this are discussed in Sec. 4.3.3.
- D5.** Advantage A4 can also be viewed as a disadvantage. Since the foil deposition technique is only sensitive to He species, the alpha collector can not be used to diagnose the loss of other high energy ions. Although the lack of ion identification associated with the scintillator detectors can be confusing, it can also be extremely useful if ambiguities can be resolved through a physical understanding of the processes involved.
- D6.** The fixed scintillator detectors are completely passive, able to diagnose high energy ion losses in any type of discharge without having any effect on the plasma. The alpha collector (and the 20° scintillator detector) is on a movable probe which requires close attention to ensure the probe is not placed too close to the plasma. Thermal damage to the probe head during plasma operations could be catastrophic for TFTR. For this reason, thorough thermal analysis of the probe head was conducted. This thermal analysis allowed operation of the alpha collector just inside the RF limiter radius in disruption free plasmas with major radii as large as 2.52 m. Therefore, the discharges for which the

alpha collector was to be used had to be carefully selected. Thermal safety considerations also ensure that the probe head is not far enough into the vessel to have an effect on the plasma.

Modeling and results of the alpha collector are presented in the next chapter.

Chapter 4

Alpha Collector - Modelling and Results

4.1 Introduction

The design of the alpha collector was considered in Chapter 3. This chapter will evaluate the results obtained using the alpha collector in several TFTR DT discharges. First, modeling of the detector response to first orbit loss is discussed in Sec. 4.2. The results of five separate DT exposures are presented in Sec. 4.3 with comparisons to the first orbit model and the results obtained with the lost alpha scintillator detector located at 90° below the outer midplane. These results show that the alpha collector detects a large partially thermalized anomalous loss at the higher plasma current (1.8 MA) which does not appear on the 90° scintillator detector, while the results at the lower plasma current (1.0 MA) are mainly consistent with first orbit loss. In the discussion of Sec. 4.4, the experimental results are summarized and the 1.8 MA anomalous loss is found to be consistent with an anomalous loss feature known as ‘delayed’ loss which only appeared in DD plasmas on the 90° scintillator detector. A look at the trajectories of α -particles reveals a dilemma regarding radial diffusion to the bottom of the vessel which makes it difficult to explain both ‘delayed’ loss to the 90° scintillator detector and the 1.8 MA anomalous loss to the alpha collector. Several loss mechanisms are considered in Sec. 4.5, but none provide a satisfactory explanation for the anomalous loss. Summary, conclusions, and suggestions for future work are offered in Chapter 6.

4.2 First Orbit Loss Model

4.2.1 Pitch Angle Distribution

First orbit loss can be calculated using the PPPL Lorentz ORBIT code [36]. The Lorentz ORBIT code integrates the Lorentz force equation to trace a single charged particle’s trajectory. Fig. 3.7 shows some typical orbits at various pitch angles that strike the alpha collector. The orbit at a pitch angle of 40° is a co-going passing

orbit, whereas the other two orbits are trapped orbits. The orbit at a pitch angle of 56° corresponds to the fattest banana orbit (i.e. at the passing-trapped boundary) and passes closest to the magnetic axis where the alpha source profile is peaked, thus giving the largest contribution to first orbit loss.

By integrating the source profile along particle orbits backwards in time from the detector through the plasma and taking into account the detector area and solid angle, the code calculates the expected collection fraction (alphas/neutron) and pitch angle distribution of first orbit loss striking the detector. The collection fraction is simply the fraction of the total alpha production (equal to neutron production) that is collected by a foil stack inside one of the collimating ports, and can be of the order of 10^{-6} alphas/neutron as calculated by ORBIT.

This collection fraction can be estimated by multiplying the expected global first orbit loss fraction by the ratio of the area of the exposed foil in the detector to the area of the vessel wall that α -particles strike. For a $\sim 10\%$ global first orbit loss spread approximately evenly over the bottom $\sim 1/3$ of the $\sim 100 \text{ m}^2$ vessel wall (ion ∇B drift direction is down) it would be expected that an area the size of the exposed foil surface of $\sim 3 \times 10^{-5} \text{ m}^2$ would collect $\sim 1 \times 10^{-7}$ of the lost alphas. However, since the foils are perpendicular to the wall they intercept particles that would have struck the wall over a larger area than the foil area, giving the foils a projected area onto the wall about an order of magnitude larger than their geometrical area. This raises the estimate based on the detector to wall area to $\sim 10^{-6}$ alphas/neutron, consistent with the code results.

ORBIT was used to predict the alpha collection fractions for the exposure conditions which will be described in Sec. 4.3. These exposures consist of two shots at 1.0 MA (exposures C & E) and two at 1.8 MA (exposures B & D). Fig. 4.1 is a plot of the predicted alpha collection fraction for first orbit loss as a function of collimating port orientation for the 1.8 MA exposures calculated using the Lorentz ORBIT code. The squares on the exposure B prediction mark the port orientations of the original probe head design which was used for this shot (Fig. 3.10). Likewise, the circles on the exposure D prediction mark the port orientations of the redesigned probe head. The alpha collection fraction is the detector response to the local pitch

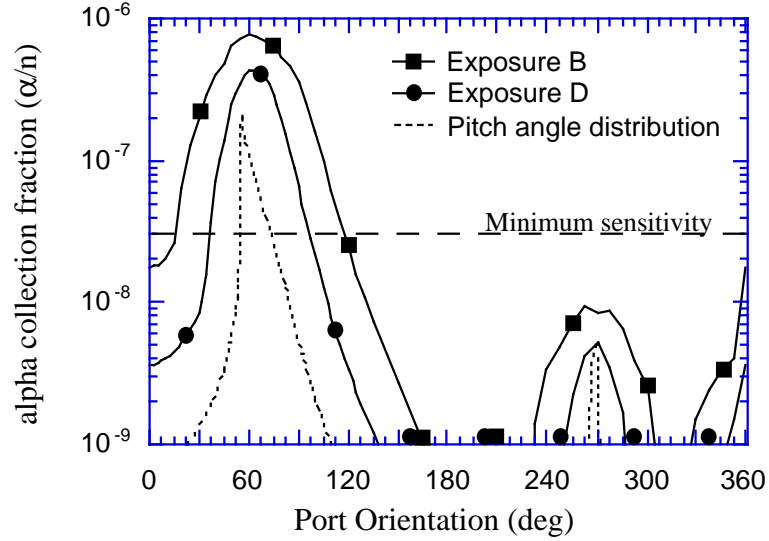


Figure 4.1: *Predicted alpha collection fraction (alphas/neutron) as a function of port orientation for the 1.8 MA exposures using the original (exposure B) and the re-designed probe head (exposure D). The dashed curve represents the expected pitch angle distribution in arbitrary units. The horizontal dashed line at 3×10^{-8} alphs/neutron represents the minimum sensitivity assuming 1×10^{17} global neutron production.*

angle distribution of the expected first orbit loss, which is plotted in arbitrary units (dashed curve) for comparison. The peaks of the detector response curves (B & D) are shifted to higher pitch angle with respect to the local pitch angle distribution due to the asymmetry in this distribution (i.e. the high pitch angle tail). The reduced magnitude (by $\sim 45\%$ at the 60° peak) of the exposure D curve with respect to the exposure B curve in Fig. 4.1 is the result of reduced alpha collection associated with the deeper collimating ports of the redesigned head.

Since the α -particles of interest have gyroradii much larger than the dimensions of the collimating port ($\rho \approx 5.0 \text{ cm} \gg 0.64 \text{ cm} = w$), their paths inside the port can essentially be thought of as straight lines. Thus an α -particle striking the foil surface in the original probe head design, in which the port's depth (d) and width (w) are equal (0.635 cm), can have a maximum angle of incidence, $\alpha_{max} = \tan^{-1}(w/d)$, of 45° . This maximum angle of incidence translates to a $\pm 45^\circ$ pitch angle acceptance range about the orientation of the collimating port axis. The maximum angle of incidence for the redesigned head, in which $d = 2w$, is 26.6° . The FWHM of the

detector response curves in Fig. 4.1 can be shown to be approximately the FWHM of the local pitch angle distribution ($\sim 5^\circ$) plus half of the pitch angle acceptance range of the collimating port used in each design (45° for the original head; $\sim 27^\circ$ for the redesign).

The detector response for inboard facing (towards the centerline of the torus, i.e. $180\text{--}360^\circ$) ports in Fig. 4.1 lies below the minimum sensitivity, illustrated by the horizontal dashed line, estimated for a 1×10^{17} total neutron production (for increased neutron production, the minimum sensitivity in alpha collection fraction is reduced). This is because an α -particle undergoing left handed gyromotion about the magnetic field (Fig. 3.9) must approach the probe head from beneath in order to enter an inboard port and is thus much more likely to be scraped off by the RF limiter before reaching the probe. Only particles with a pitch angle very close to 90° can intercept the inboard side of the detector since they travel nearly straight down (e.g. ripple well trapped particles) and can avoid limiter scrape off. These particles are represented by the peaks centered at the 270° port position. However, these particles would most likely be shadowed by the probe head itself before they could enter a collimating port, an effect that is not taken into account in this simulation. Thus, it is expected that inboard facing ports would not collect significant quantities of escaping alphas.

Since an α -particle is produced for each neutron, the calculated collection fraction is converted to expected alpha fluence by multiplying by the global neutron production. The code's accuracy is highly dependent on the assumed source and current profiles as is discussed in Sec. 4.3.5. These profiles are generally obtained from the transport code, TRANSP [16], which takes inputs from various diagnostics to generate time dependent plasma parameters.

4.2.2 Range Distribution

The Lorentz ORBIT code predicts the total fluence and pitch angle distribution to a detector. However, to determine the range distribution of alphas in the nickel foils it is also necessary to determine the angle of incidence distribution of alphas on the

foils. The conversion from pitch angle distribution to incident angle distribution is accomplished using an auxiliary code called PORT, developed specifically for this detector. PORT launches ions backwards in time from a grid on the foil surface of each port at various pitch angles and gyrophases, weighted by the ORBIT-calculated pitch angle distribution. Particle drifts, such as ∇B and curvature drift, are ignored since the particles are generally tracked for less than one gyro-orbit to determine if they clear the probe head. Thus a particle orbit is a simple helix about the magnetic field vector, defined by the particle's gyroradius ρ and pitch angle, $\chi = \cos^{-1}(v_{\parallel}/v)$, where v is the particle's velocity and v_{\parallel} is the parallel velocity component along the magnetic field. The magnetic field at the probe location (i.e. at the bottom of the vessel) is assumed to lie in the horizontal plane (i.e. parallel to the midplane) and to make an angle χ_{bt} with the toroidal direction determined by $\chi_{bt} = \tan^{-1}(B_p/B_t)$, where B_p is the poloidal field and B_t is the toroidal field at the alpha collector. PORT assumes that the first orbit loss to a detector port is independent of gyrophase at the detector (good to within $\sim 20\%$ as determined by ORBIT) and that the foil surface is flat. If a particle clears the port walls and the probe head, it is counted and its angle of incidence is determined. The angle of incidence, α (0° corresponding to normal incidence), is determined by taking the scalar product between the particle's velocity vector at the foil surface and a unit vector along the axis of the collimating port and is found to be:

$$\cos \alpha = \cos \chi \cos \chi_0 + \sin \chi \sin \chi_0 \cos \gamma \quad (4.1)$$

where χ is the particle's local pitch angle (0° being along the magnetic field in the direction of the plasma current), χ_0 is the angle between the magnetic field and the axis of the collimating port, and γ is the gyrophase of the particle at the foil (0° corresponding to the bottom of a gyro-orbit). Fig. 4.2 shows the conversion of 1.0 MA and 1.8 MA ORBIT calculated pitch angle distributions for 3.5 MeV α -particles to incident angle distributions for a 30° and a 75° port using PORT. Notice that the 1.8 MA pitch angle distribution of Fig. 4.2(a) has a peak at 56° corresponding to the fattest banana orbit, which was depicted in Fig. 3.7, since it passes closest to the magnetic axis where the source profile is peaked.

Once the distribution of incident angles onto the foil is determined using the PORT code, the range distribution of 3.5 MeV first orbit lost α -particles can be determined using IBM's TRIM-95 code [37]. The TRIM code uses a Monte Carlo algorithm to

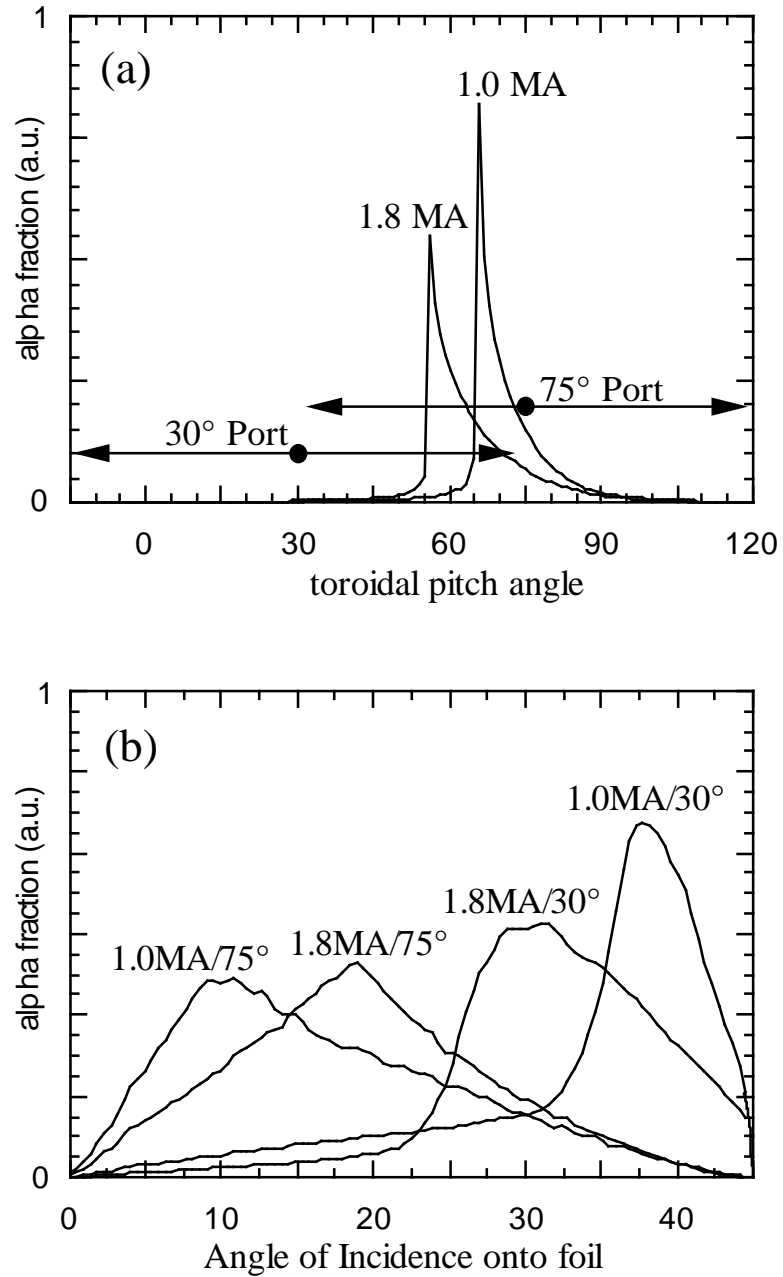


Figure 4.2: (a) Toroidal pitch angle distributions in arbitrary units calculated by the Lorentz ORBIT code for 3.5 MeV α -particles from exposures B (1.8 MA) and C (1.0 MA). The $\pm 45^\circ$ acceptance range of the original probe design is depicted for the 30° and 75° ports. (b) The resulting angle of incidence distributions for the 30° and 75° ports calculated by PORT for the pitch angle distributions shown in (a).

calculate the penetration of ions into solids. Fig. 4.3(a) shows the TRIM calculated range distributions for He ions implanted at various energies into nickel at normal incidence. The standard deviation of the range distribution, known as straggling, is $\sim 0.2 \mu\text{m}$ at 3.5 MeV. The relative magnitude of the distribution peaks decrease with increasing energy as the straggling increases, keeping the area under each curve constant. Discarding the first layer, to minimize tritium contamination, results in a minimum detection energy of ~ 0.5 MeV.

Fig. 4.3(b) shows the TRIM calculated range distributions for He ions at 3.5 MeV into nickel at various angles of incidence. The widths of the range distributions increase with incident angle because transverse straggling is more significant than longitudinal straggling. These distributions are combined with the predicted incident angle distributions to obtain the expected range distribution for first orbit loss in each nickel foil stack.

The foils are actually curved since they are wrapped around a cylindrical spool inside the probe head. This curvature can cause particles to strike the foil at larger incident angles than if the foil were flat, resulting in a more shallow implantation range. However, this curvature can only be responsible for spreading of the first orbit loss range distribution to, at most, one foil layer shallower. It has little effect on the position of the peak in the range distribution. This effect is neglected along with other spreading effects such as non-uniformities in foil thickness, which may be responsible for the spreading of calibration sample results seen Sec. 3.4.2, and the $\pm \sim 0.5$ MeV Doppler broadening of the birth energy distribution (Sec. 2.3.1). These effects taken together can be expected to spread the depth distributions of first orbit loss by one foil layer in either direction.

In the next section, the first orbit loss model predictions generated through the use of ORBIT, PORT and TRIM are compared to alpha collector measurements.

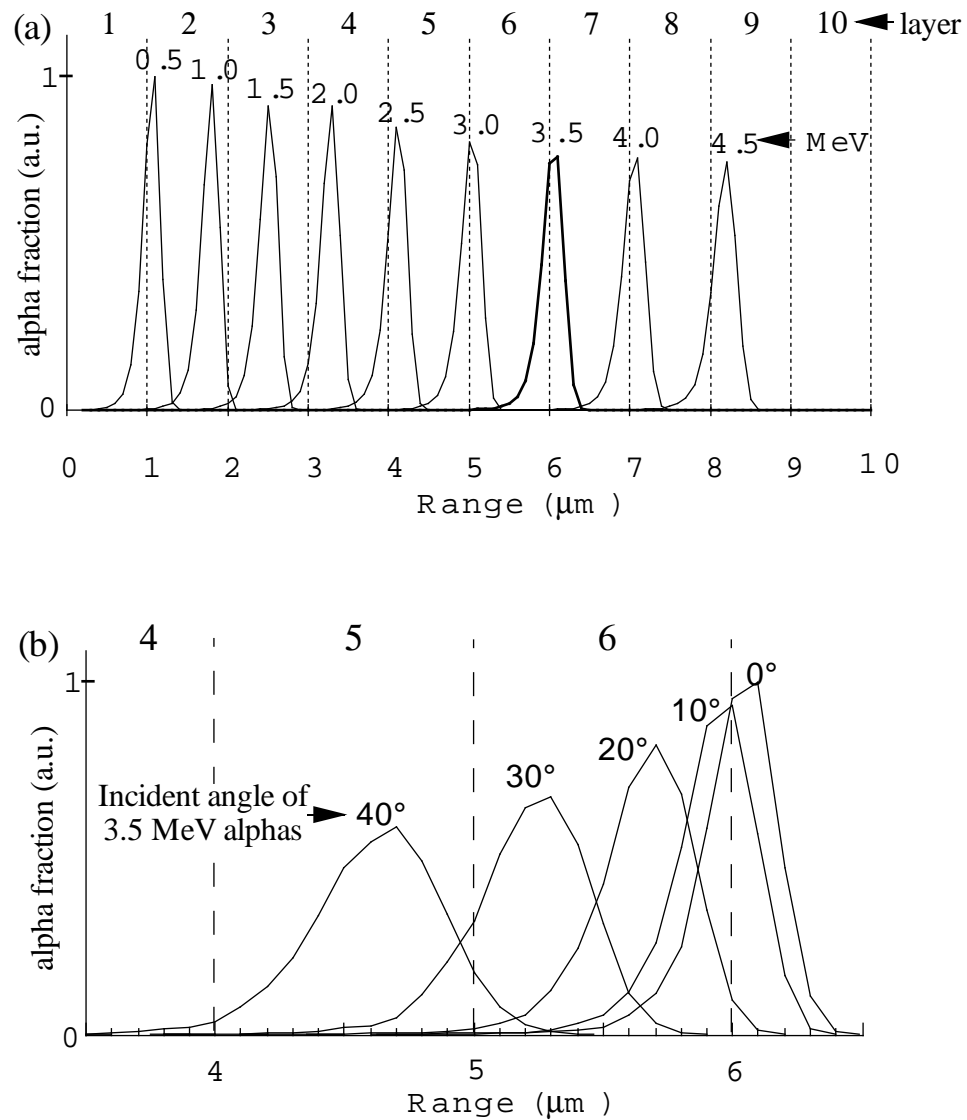


Figure 4.3: (a) Implantation range distributions for monoenergetic alpha particles implanted into nickel at various energies and at normal incidence as calculated by the TRIM-95 code. The boundaries between the 1 μm thick foil layers are depicted by the dashed lines. (b) Implantation range distributions for 3.5 MeV alpha particles implanted into nickel at various angles of incidence.

Exposure	A	B	C	D	E
Probe head	Original	Original	Original	Redesign	Redesign
Shot #	73319/73320	74796	76014	80553	84593
I_p (MA)	0.6	1.8	1.0	1.8	1.0
R_0 (m)	2.45	2.45	2.45	2.45	2.45
B_t (Tesla)	4.75	4.75	4.88	4.87	4.88
P_b (MW)	5.2	10.2	9.4	12.7	11.1
t_b (s)	3.0-3.7	3.0-3.7	3.0-3.7	3.0-4.0	3.0-3.7
S_n ($\times 10^{17}$ n)	0.6	1.3	1.1	4.3	1.8
n_{e0} ($\times 10^{13}$ cm $^{-3}$)	---	4.6	3.1	4.2	3.6
T_{e0} (keV)	---	6.1	5.8	7.4	6.4
τ_{sd0} (s)	---	0.21	0.29	0.30	0.28

Table 4.1: *Alpha Collector Discharge Parameter List*

4.3 Experimental Results

The alpha collector has been exposed to a total of five DT discharges. Plasma parameters for these 5 discharges, labeled A through E, are given in Table 4.1. These discharges were conducted at low neutral beam injection (NBI) power to avoid MHD activity, so that first orbit loss was expected to be the dominant loss mechanism. The power was also kept low to avoid probe overheating, although thermal design considerations do allow its use in high power discharges with plasmas as large as $R=2.52$ m. The probe was placed in the same position for each exposure, placing the center of the upper row of collimating ports 0.5 cm radially inward from (i.e. above) the nearest limiter, and the lower row 0.6 cm radially outward from (i.e. below) the limiter. In this position, the probe tip was ~ 16 cm outside the last closed flux surface.

Exposure A

Exposure A was actually exposed to two identical DT discharges (and two ‘dry run’ DD discharges) conducted at a plasma current of 0.6 MA and a neutral beam power of 5 MW using one co-going (in relation to the plasma current) tritium beam and one

counter-going deuterium beam. This exposure resulted in the unexpected melting of a majority of the foils and aluminum wires. It is suspected that neutral beam ion loss was responsible for the overheating of the foils, as explained below. The exposure A foils were not analyzed for He content for this reason.

Although exposure A did not provide useful data in terms of a depth profile of He, the resulting heating pattern did provide useful information. The observation that most of the heat damage occurred in ports that were outboard facing implies that the damage was caused by high energy ions. This is because a large gyroradius is necessary to avoid collimation at these large pitch angles (e.g. 75°). In order to enter an outboard facing port, an ion (which undergoes left handed helical motion w.r.t. the magnetic field) must enter the port on the bottom portion of its gyrophase (Fig. 3.9). Thus its gyrocenter will be above the port. To enter an inboard facing port, however, the gyrocenter must be below the elevation of the port, increasing the likelihood that it would have been scraped off by limiters or other obstructions prior to reaching the port (Sec. 4.2.1). For this reason the foils of the inboard facing ports are not expected to be exposed to a large ion flux, and hence, experienced little damage.

Melting of nickel from room temperature requires heating to the melting point of 1453°K and then additional heating to incur the phase transition. The specific heat of nickel in the temperature range of interest is $\approx 0.5 \text{ J}/^\circ\text{K}\cdot\text{g}$, and the latent heat of vaporization is 6378 J/g . The minimum heat flux (i.e. ignoring thermal conduction and radiation) necessary to melt $1 \mu\text{m}$ thick Ni foil with a density of 8.9 g/cm^3 in 1 s is $\approx 6 \text{ W/cm}^2$, with $\sim 90\%$ of this energy going into the phase transition. The maximum α -particle heat flux to the foil stack in the collimating port oriented 75° outboard of the toroidal direction for this exposure as predicted by ORBIT is only $\approx 300 \text{ mW/cm}^2$. Thus the expected alpha heating is at least a factor of 20 too small to cause any melting. The peak DT neutron rate for these shots of $6 \times 10^{16} \text{ n/s}$ corresponds to a maximum alpha power of 34 kW . Assuming for the moment that the same fraction of the 5 MW of NBI power strikes the 75° foil stack as does the alpha power results in $\sim 44 \text{ W/cm}^2$ of beam ion heating to the foils. Thus the large NBI power, combined with the possibility of higher relative NBI ion loss to the probe due to their nonisotropic velocity distribution, may account for the overheating of the

foils.

As a means of avoiding heat damage due to excessive NBI ion loss, subsequent exposures were conducted at higher plasma current and used co-going only NBI. The effect of the higher plasma current is to reduce the banana width of trapped beam ions allowing more of them to be confined. The use of co-going beams also causes more trapped beam ions to be confined since they are ionized on the co-going leg of their banana orbits and move in closer to the center of the plasma on the subsequent counter-going leg. The use of counter-going beams has the opposite effect of neutrals ionizing on their counter-going leg and then shifting outward during their co-going leg and thus are more likely to be unconfined. The result that calculated prompt first orbit loss of neutral beam ions ranges from 30 to 38% (depending on the beam tangency radius) for counter-injection, and only 0 to 1% for co-injection, for a 2.6 m major radius plasma at a plasma current of 0.9 MA [13] illustrates the strong dependence of beam ion loss on the direction of beam injection. These two modifications, namely higher plasma current and co-going beams, resulted in virtually no overheating of the foils in subsequent exposures with the exception of two ports which were facing directly into the magnetic field and presumably were exposed to excessive thermal plasma flux. None of the exposed Al wires experienced any melting.

NBI ions were not taken into consideration in the original design of the collimating ports. Their relatively large gyroradius of about 1.6 cm for 100 keV tritium ions allows a large fraction of them to reach the foils without being separated out by collimation. The PORT code was used to calculate the fraction of high energy ions with a given gyroradius that can avoid collimation to reach the foils. Fig. 4.4 shows the fraction of ions that can reach the 75° foils without being separated out versus the collimating port depth. A port width of 1/4 in (0.63 cm) and a flat pitch angle distribution were assumed and the gyro-phases of the particles were incremented from -90° to 90°, 0° being the bottom of a gyro-orbit. The maximum transmission is calculated for particles hitting the foil at the pitch angle corresponding to the orientation of the port (i.e. 75°). It can be seen from Fig. 4.4 that the original design depth of 1/4 in did little to discriminate between alphas and the smaller gyroradius NBI tritons. By increasing the port depth the collimator is made much more effective in discriminating between the two ion species. For this reason the redesigned probe head was developed

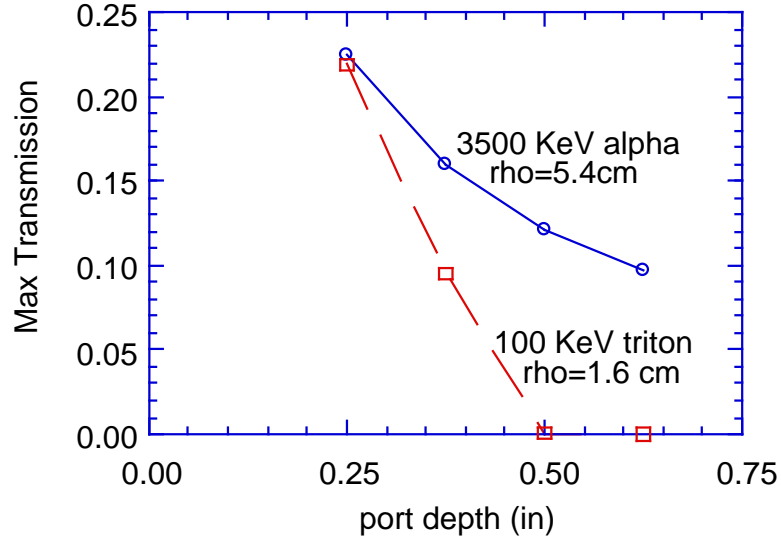


Figure 4.4: *Maximum transmission fraction for $\chi = 75^\circ$ particles hitting the 75° foil stack versus collimating port depth plotted for birth energy alphas and NBI tritons. Averaged over gyrophase ($-\pi/2$ to $\pi/2$) and foil surface for $1/4$ in diameter port. NBI transmission cuts off at $d = 1/2$ in.*

with ports having double the depth at $1/2$ in (1.27 cm) while leaving the diameter at $1/4$ in. As can be seen in Fig. 4.4, this has the effect of nearly eliminating the ability of NBI ions to reach the foils in this 75° outboard facing port, while only reducing the maximum transmission of alpha particles by about a factor of 2. This, combined with a reduced pitch angle acceptance range of also about a factor of 2, results in reducing the alpha flux by only about a factor of 4 for the 75° port when compared to the original design (assuming a flat pitch angle distribution). The redesigned probe head allows the use of the alpha collector in discharges with low plasma current and/or counter-going beams (such as exposure A), but it has not been exposed in TFTR under these conditions.

Exposures B–E

Exposures B through E are nominally identical discharges with the exception of the two values of plasma current and slight modifications that can be seen in Table 4.1.

Note that exposures B & C used the original probe head, and exposures D & E used the redesigned head with collimating ports that were twice as deep, and the head rotated clockwise 7.5° (Sec. 3.5).

Exposures B through E suffered only minimal foil heat damage, and only in ports that had a direct line of sight along the magnetic field on the side opposite the nearest RF limiter. This corresponds to ports at 165° and 210° . Thermal plasma could flow along field lines unimpeded to the foils in these ports. These four samples (i.e. the upper and lower row of the 165° and 210° ports) were not analyzed for this reason.

Analysis of foils from the inboard facing ports (towards the center of the torus) resulted in levels of implanted He below or near the minimum sensitivity ($\sim 5 \times 10^8$ alphas). This was as expected for the reasons discussed in Sec. 4.2.1. Therefore, only the outboard facing ports are compared to the first orbit loss model in this section. Although there was essentially no He implanted in these inboard facing samples, it was important to obtain these results to verify expectations and to provide additional insight into any anomalous results that may be obtained.

When a fluence measurement is compared to the first orbit loss model in this section, only the summed fluence of foil layers 4 through 9 is included. Due to the geometry of the collimating ports and the predicted range distribution of 3.5 MeV α -particles (Fig. 4.3), it is to be expected that essentially no first orbit lost α -particle will be stopped by foil layers shallower than $3 \mu\text{m}$, nor penetrate deeper than $9 \mu\text{m}$. Layers 2 through 3, and 10 were therefore excluded from comparisons against first orbit loss since He in these layers must be due to other sources such as partially thermalized alpha ash or externally introduced He puffs.

In each part of this section, a characteristic of the observed loss is compared to the first orbit loss model, first for the two exposures conducted at a plasma current of 1.0 MA (exposures C & E), then for the two exposures conducted at 1.8 MA (exposures B & D). A comparison is then made with the 90° lost alpha scintillator images for each exposure. Sec. 4.3.1 considers absolute fluence, Sec. 4.3.2 energy distribution, Sec. 4.3.3 pitch angle distribution, and Sec. 4.3.4 radial distribution.

4.3.1 Absolute Fluence

$I_p=1.0$ MA Absolute Fluence

Fig. 4.5 shows the comparison between the observed fluence (in number of α -particles collected) to the upper and lower rows of outboard facing ports (30° , 75° , 120°) at 1.0 MA (exposures C & E), along with the first orbit loss model predictions generated with the Lorentz ORBIT code (Sec. 4.2.1) for the upper row as a function of collimating port orientation. The first orbit loss model for the lower row is not plotted because it is essentially unchanged from the model for the upper row. The first orbit loss model curve is the predicted alpha collection fraction (as seen in Fig. 4.1 for 1.8 MA exposures) times the total neutron production for each shot. The observed fluence is plotted for the total He content of layers 4 through 9. The observed fluence agrees very well with the first orbit loss model, within the uncertainties discussed in Sec. 4.3.5.

$I_p=1.8$ MA Absolute Fluence

Fig. 4.6 (analogous to Fig. 4.5) shows the comparison between the observed fluence and the first orbit loss model at 1.8 MA (exposures B & D). The results of the 30° and 75° ports indicate that an anomalously large loss exists, with an alpha fluence roughly an order of magnitude larger than is expected for first orbit loss to the upper rows. This anomalous loss is significantly diminished in the lower rows. The results for the 120° ports, however, appear to be in agreement (keeping in mind that they are near minimum sensitivity) with the first orbit loss model, within the uncertainties discussed in Sec. 4.3.5. This indicates that the anomalous loss does not extend to pitch angles as large as does first orbit loss.

The samples with the largest fluence for each of the 1.8 MA exposures, corresponding to the upper 75° port for exposure B and the upper 67.5° port for exposure D, show increases by factors of 4.7 and 6.4 respectively when the measured fluence in layers 4 through 9 is compared to the predicted fluence for first orbit loss. When

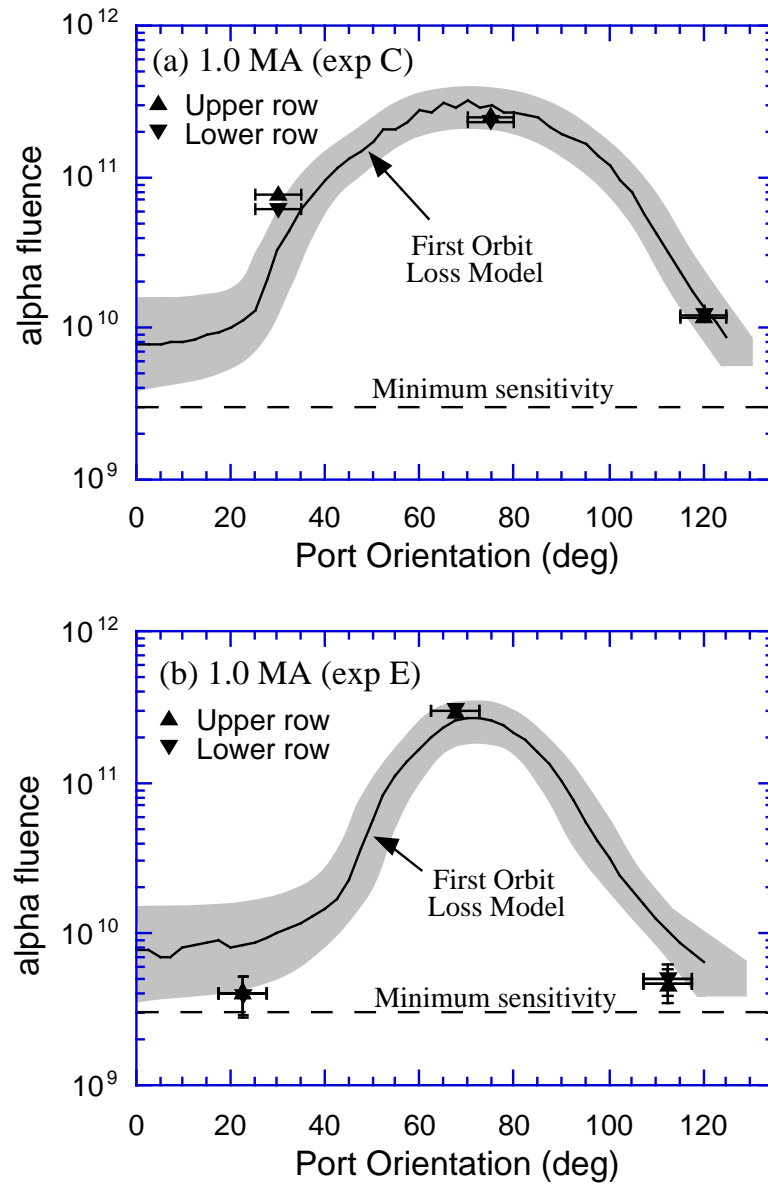


Figure 4.5: $I_p=1.0$ MA - Measured fluences of He in layers 4 through 9 for the upper and lower rows of (a) exposure C using the original probe head design, and (b) exposure E using the redesigned probe head, compared with the first orbit loss model calculated with the Lorentz ORBIT code as a function of port orientation. The dashed line, representing the minimum sensitivity, is approximated by multiplying the minimum sensitivity per layer (5×10^8 alphas) by 6 layers. The vertical error for data points above 1.2×10^{10} alphas is $\sim \pm 10\%$, corresponding approximately to the height of the triangular data symbol.

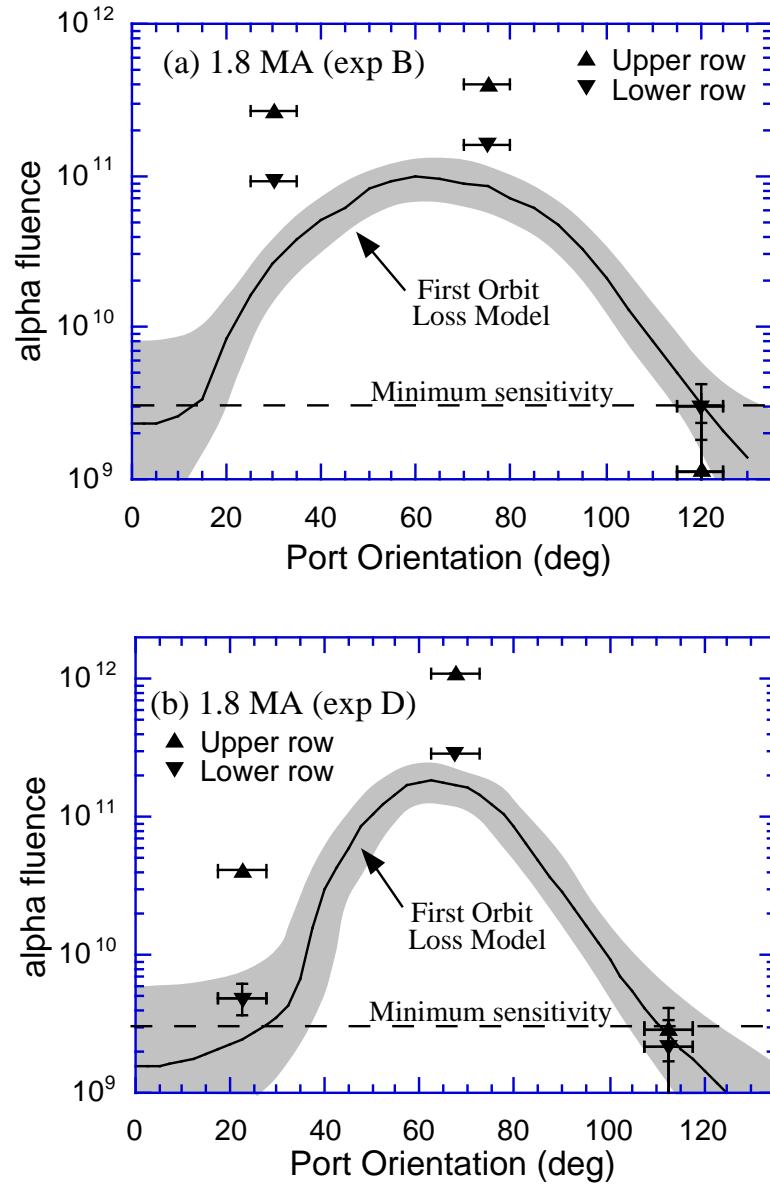


Figure 4.6: $I_p=1.8$ MA - Measured fluences of He in layers 4 through 9 for the upper and lower rows of, (a) exposure B using the original probe head design, and (b) exposure D using the redesigned probe head, compared with the first orbit loss model. Same notation as Fig. 4.5. The 30° and 75° ports reveal the existence of an anomalous loss at 1.8 MA.

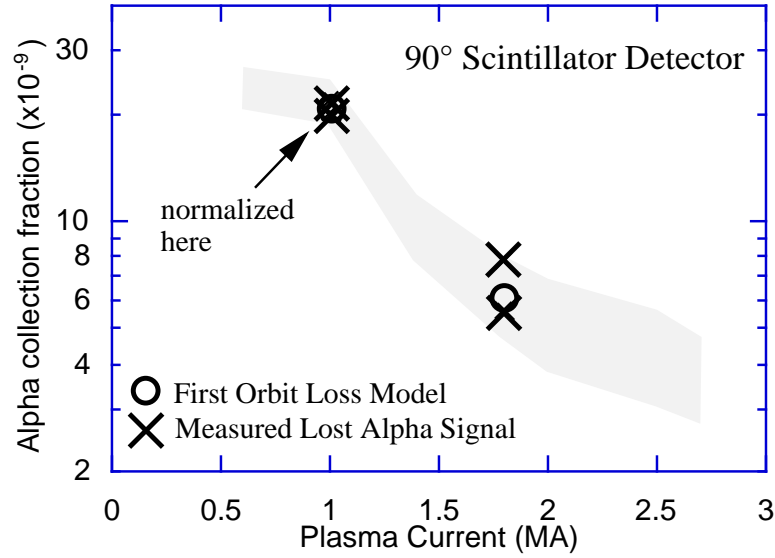


Figure 4.7: Plasma current dependence of the alpha collection fraction measured with the 90° lost alpha scintillator detector normalized to the first orbit loss model at 1.0 MA. The shaded region corresponds to the first orbit loss model calculated for $R=2.52$ m plasmas in Ref. [9], but appears to fit the $R=2.45$ m data well. The good agreement with the model implies that this detector does not ‘see’ the anomalous loss apparent at 1.8 MA using the alpha collector probe.

the total measured fluence of layers 2 through 10 is compared to the predicted fluence, both of these samples show an increase by a factor of ~ 7 . Assuming that the predicted first orbit loss is included in these measurements makes the anomalous loss ~ 6 times larger than first orbit loss.

Absolute Fluence to Lost Alpha Detector

Fig. 4.7 shows the dependence of the 90° scintillator signal on plasma current for shots B through E. The data are normalized to the model at 1.0 MA due to uncertainties in the absolute calibration [9]. The gray area overlaid on this plot is taken from the analysis of Ref. [9]. It represents the first orbit loss model with uncertainties as calculated for $R=2.52$ m plasmas, but appears to fit the model predictions at $R=2.45$ m quite well. The ratio of alpha loss between 1.0 and 1.8 MA agrees with the first

orbit loss model within the uncertainties. There is no increase in the signal at 1.8 MA with respect to the model, consistent with the behavior observed in all other plasma discharges. The first orbit loss model, shown by circles in Fig. 4.7, predicts a drop in the alpha collection fraction by a factor of ~ 3.4 between 1.0 MA and 1.8 MA. An anomalous loss causing a factor of 7 increase at 1.8 MA, such as that observed by the alpha collector, would make the measured alpha collection fraction, shown by X's in Fig. 4.7, a factor of ~ 2 larger at 1.8 MA than at 1.0 MA. Hence, it appears that the anomalous loss detected at 1.8 MA with the alpha collector is not seen by the 90° lost alpha scintillator detector.

4.3.2 Energy Distribution

$I_p=1.0$ MA Energy Distribution

Fig. 4.8 shows the comparison between the measured range distribution and the first orbit loss model of 3.5 MeV α -particles generated with the ORBIT, PORT, and TRIM codes (Sec. 4.2) for the upper and lower row of outboard facing ports at 1.0 MA (exposures C & E). There is reasonable agreement between the observed distribution and the model, with the exception of a low energy loss feature appearing in layers 2 and 3 corresponding to an energy below 2.0 MeV. Although the shape of the peaks lying between layers 4 and 9 do not exactly match the first orbit loss model peaks, the important feature is that the peaks appear in approximately the same layers at an overall magnitude determined in Sec. 4.3.1 to be in agreement with first orbit loss. The disagreement in the specific shape of the distributions may be attributable to the neglect of foil non-uniformities, curvature of the foils, and Doppler broadening of the birth energy distribution (Sec. 4.2). Overall, the agreement is sufficient to conclude that the observations are consistent with the model for first orbit loss with the exception of a low energy loss feature that is not yet understood, but might be related to the anomalous loss at 1.8 MA.

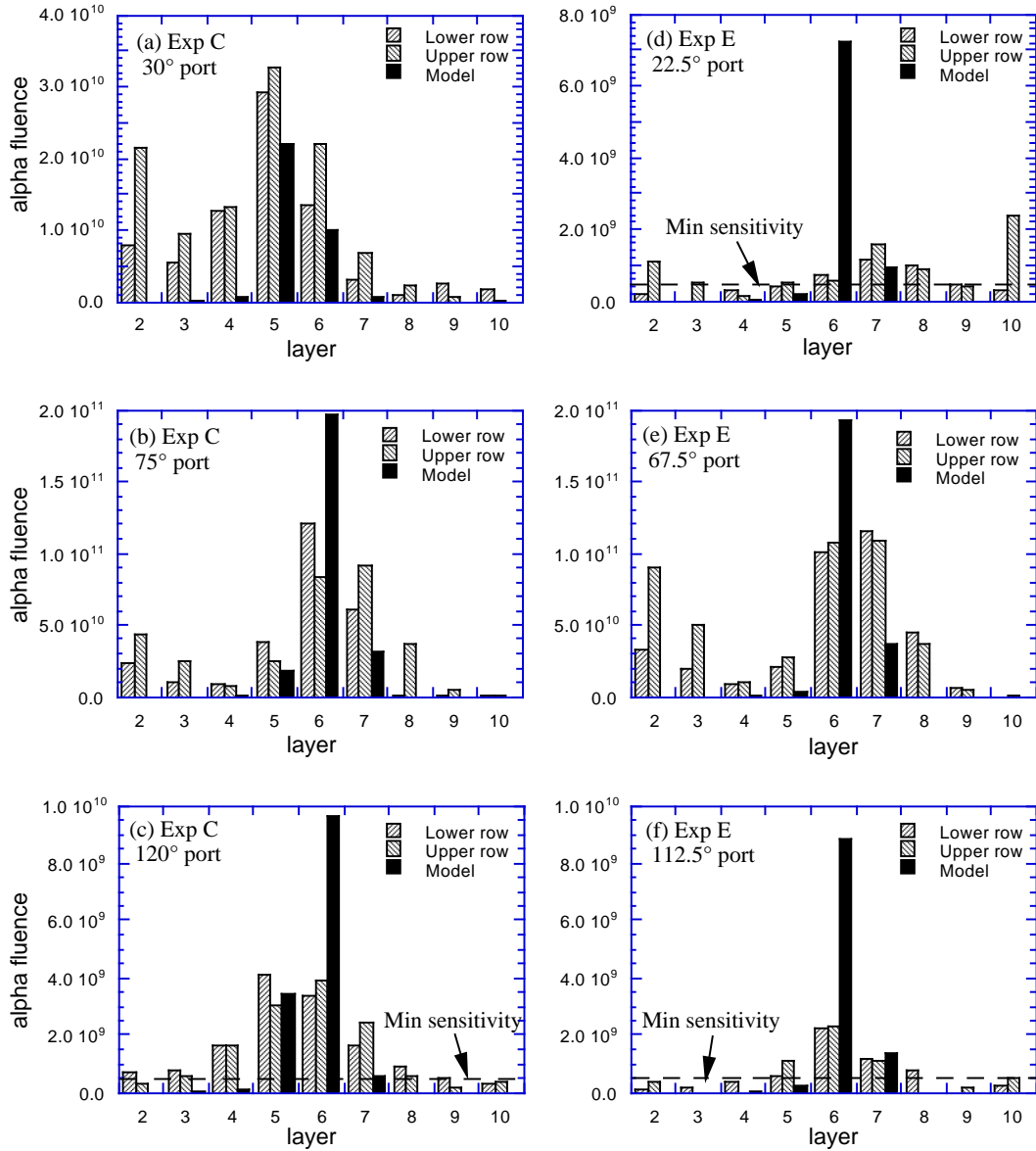


Figure 4.8: $I_p=1.0$ MA - Implantation range distributions as a function of layer (*i.e.* $1 \mu\text{m}$ bins) for the upper and lower rows and model predictions for (a) 30° (b) 75° and (c) 120° ports of exposure C, and (d) 22.5° (e) 67.5° and (f) 112.5° ports of exposure E. Notice that the vertical scales are linear and not all the same. The plots with a maximum of the vertical scale $\leq 2 \times 10^{10}$ alphas have the minimum sensitivity of the sample analysis ($\sim 5 \times 10^8$ alphas/layer) represented by a dashed line.

$I_p=1.8$ MA Energy Distribution

Fig. 4.9 (analogous to Fig. 4.8) shows the comparison between the measured range distribution and the first orbit loss model for the upper and lower rows of outboard facing ports at 1.8 MA (exposures B & D). The observed peak in the range distribution occurs at a shallower depth and has a significantly larger width than the first orbit loss model for the 30° and 75° ports of exposure B, and the 67.5° port of exposure D (Figs. 4.9(a, b, e)). This indicates that the anomalous loss occurring at 1.8 MA consists of partially thermalized α -particles.

The data from the 22.5° ports (upper and lower rows) from exposure D (Fig. 4.9(d)) seem to indicate an alpha loss near the birth energy and not the partially thermalized loss mentioned above. This is an indication that the partially thermalized anomalous loss does not occur at pitch angles below the maximum pitch angle accepted by this port ($\sim 49^\circ$). Thus, the observed signal should correspond to purely first orbit loss of passing particles. However, as seen in Fig. 4.6(b), the total fluence for layers 4–9 of the upper 22.5° port was nearly 17 times expected first orbit loss. The peak in the sixth layer is repeated in the lower row of the 22.5° port, as seen in Fig. 4.9(d), verifying the lack of a partially thermalized loss to this location. Also, the total fluence for the lower row seen in Fig. 4.6(b) is consistent with first orbit loss. Although there does appear to be an anomalously large signal to the upper row, until this result can be shown to be reproducible, it will be assumed that the loss to this port is purely first orbit loss and is not associated with the partially thermalized anomalous loss observed at 1.8 MA. If this is a valid result, it is associated with a prompt loss mechanism, not the delayed mechanism (allowing for time to slow down) responsible for the partially thermalized anomalous loss.

The peak in the fourth layer of the 75° port of exposure B (Fig. 4.9(b)) corresponds to an alpha loss energy of $\sim 2.2 \pm 0.3$ MeV (see Fig. 4.3(a)) if normal incidence is assumed. Similarly, the peak in the fifth layer of the 67.5° port of exposure D (Fig. 4.9(d)) corresponds to an alpha loss energy of $\sim 2.7 \pm 0.3$ MeV. Exposure D used the redesigned probe head with the improved collimation (i.e. particles implant closer to normal incidence), and thus provides a better indication of alpha loss energy than does exposure B, which used the original design. It might also be inferred from the

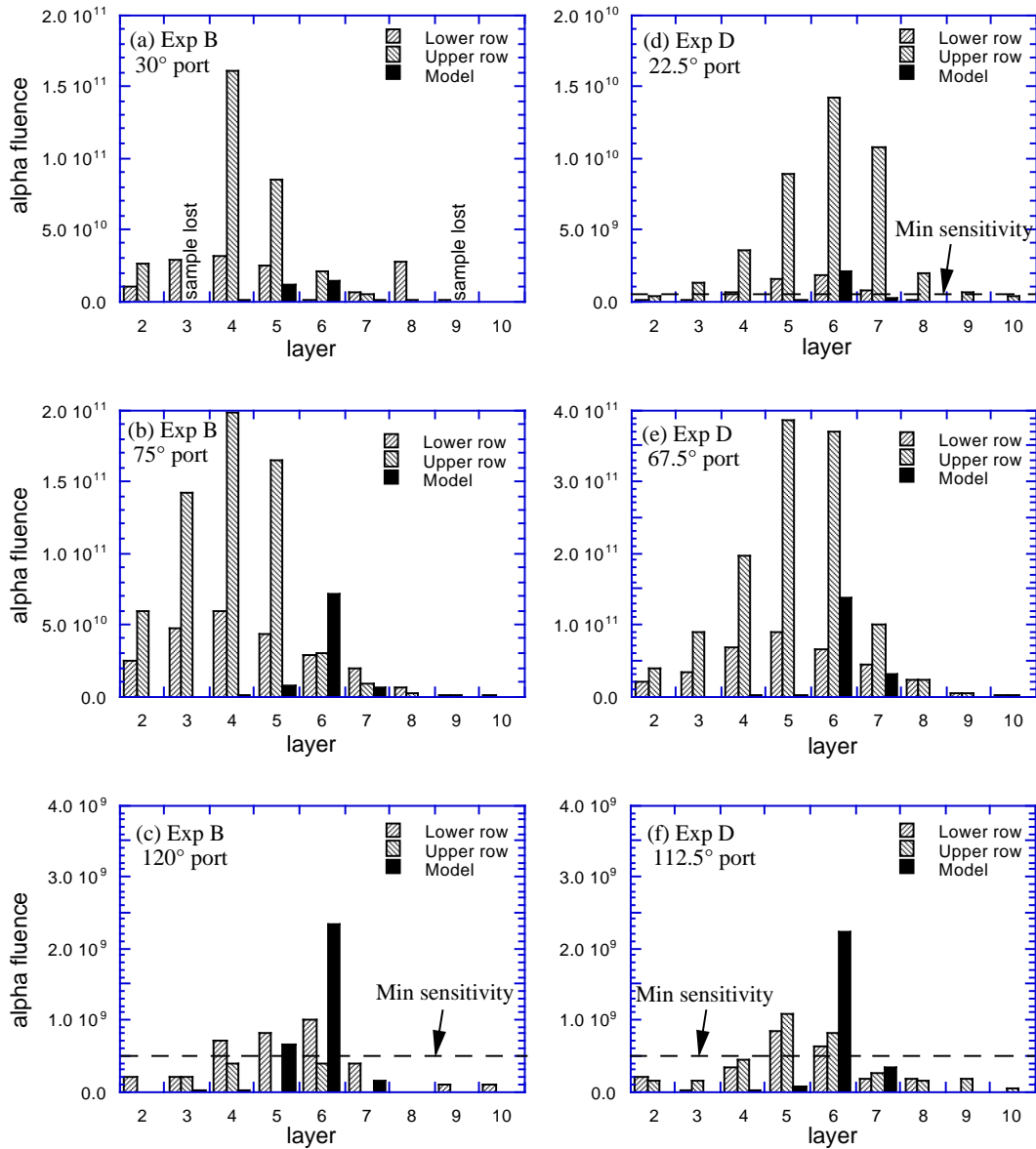


Figure 4.9: $I_p=1.8$ MA - Implantation range distributions as a function of layer for the upper and lower rows and model predictions for (a) 30° (b) 75° and (c) 120° ports of exposure B, and (d) 22.5° (e) 67.5° and (f) 112.5° ports of exposure D. Same notation as Fig. 4.8. Layers 3 and 9 of the upper row of the 30° port of exposure B in (a) were lost during the tritium decontamination process [31].

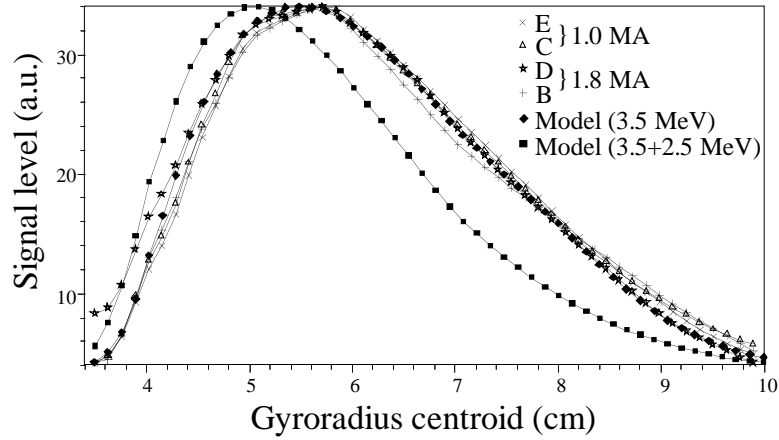


Figure 4.10: *Gyroradius distributions of alpha loss as measured with the 90° lost alpha scintillator detector averaged over toroidal pitch angle, from 45° to 90° , and time, from 3.4 to 3.7 sec (i.e. the quasi-steady state portion of the discharge). Model curves are plotted for 3.5 MeV α -particles and equal fluxes of 2.5 MeV and 3.5 MeV α -particles after being corrected for the finite aperture sizes and optical resolutions of the detectors. The curves are normalized vertically to each other near their peaks, but the horizontal axes were absolutely calibrated by an in-vessel alignment to within ~ 1 cm.*

deeper implantation range in exposure D that the 7.5° clockwise rotation that went into the redesign was such as to bring the axis of the port closer to the pitch angle of the anomalous loss, also allowing particles to implant closer to normal incidence. In other words, the anomalous loss probably occurs at a pitch angle closer to 67.5° than to 75° . Assuming the two 1.8 MA exposures are exposed to an anomalous loss of the same energy, the peak of the energy distribution is inferred to be $\sim 2.5 \pm 0.3$ MeV (i.e. $\sim 70 \pm 10\%$ of the birth energy). In the discussion of Sec. 4.4, the anomalous loss at 1.8 MA will be simplified as having a single loss energy of 2.5 MeV.

Energy Distribution to Lost Alpha Detector

The gyroradius distributions for exposures B through E as measured with the 90° lost alpha scintillator detector are shown in Fig. 4.10. Two model curves, taking into account the finite aperture sizes and optical resolutions of the detectors, are

also plotted. The distributions show good shot to shot consistency, independent of the plasma current, and they agree closely with the model assuming alpha loss at a single energy of 3.5 MeV. For comparison with what might be expected if some of the anomalous loss observed with the alpha collector were also detected by the 90° scintillator detector, the other model assumes equal loss components at energies of 2.5 MeV and 3.5 MeV. These distributions provide further evidence that the lost alpha scintillator detectors do not detect the partially thermalized anomalous loss observed with the alpha collector at 1.8 MA, which was inferred to be up to 6 times the first orbit loss at an energy of ~ 2.5 MeV.

4.3.3 Pitch Angle Distribution

$I_p=1.0$ MA Pitch Angle Distribution

The first orbit model predictions in Figs. 4.5 and 4.6 are just the expected pitch angle distributions corrected for the geometric resolution of the detector (Sec. 4.2). So the pitch angle distributions of Fig. 4.5 for the exposures at a plasma current of 1.0 MA (C & E) show good agreement between the observations and the first orbit loss model. However, the wide pitch angle acceptance of the collimating ports ($\pm 45^\circ$ for the original design; $\pm 27^\circ$ for the redesign) result in relatively poor pitch angle resolution. To obtain improved information pertaining to the pitch angle distribution, it was decided to cut selected samples vertically in half to compare the fluences contained in the right and left halves. A loss at a pitch angle larger than the collimating port's orientation tends to concentrate He in the left half of the foil stack, assuming $\rho \gg w, d$ and $\chi_0 > 0$ (see Secs. 3.3 and 4.2.2 for symbol definitions).

The PORT code was used to predict the fraction of alpha fluence implanted in the left half of the foil stack, referred to as the left collection fraction, for the pitch angle distribution generated for first orbit loss using the Lorentz ORBIT code. In other words, the left collection fraction L is:

$$L = \frac{l}{l+r} \quad (4.2)$$

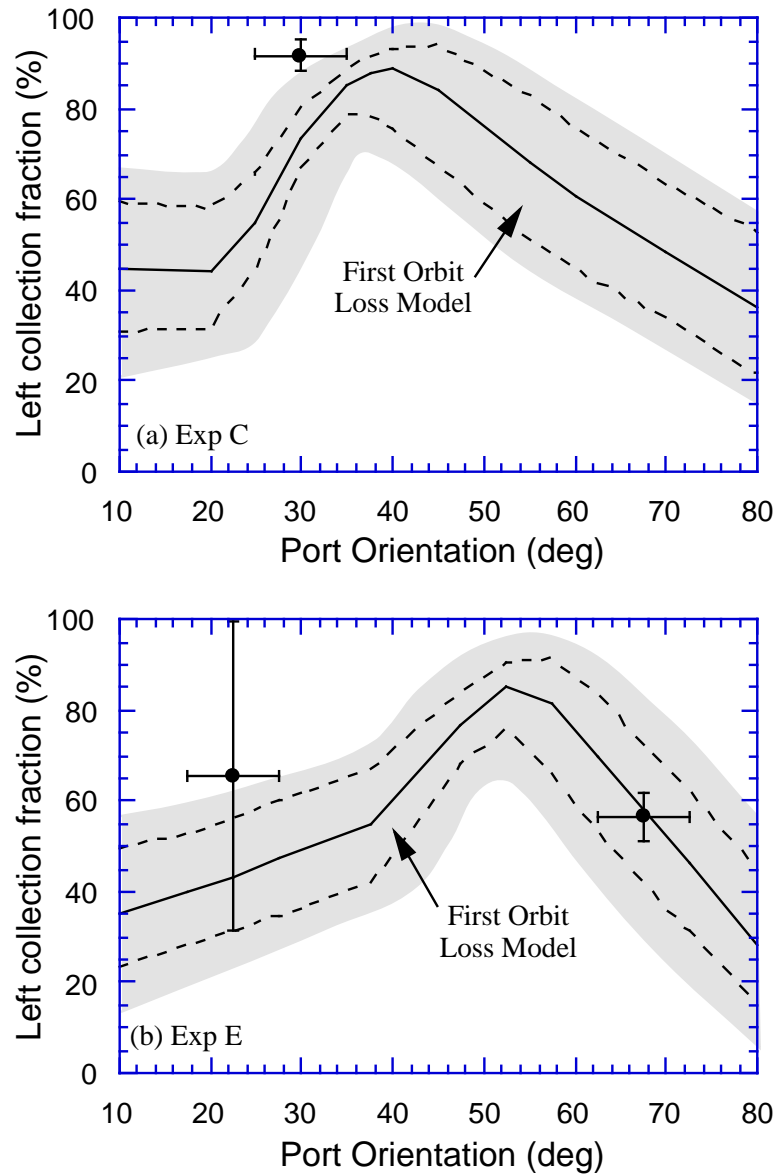


Figure 4.11: $I_p=1.0$ MA - Left collection fraction as a function of port orientation for the upper row of the (a) 30° port of exposure C, and (b) 22.5° and 67.5° ports of exposure E. The left collection fraction is the fraction of He in layers 4 through 9 that implanted in the left half of the stack. The model is based on the first orbit loss pitch angle distributions calculated using ORBIT. The dashed lines represent the model assuming the cut is made 10% of the port width to the right (upper dashed line) or left (lower dashed line) of center.

where l and r are the amounts of He contained in the left and right halves respectively. Fig. 4.11 shows a comparison between the fraction of He detected in the left half for the selected samples at 1.0 MA and the model prediction as a function of port orientation. The solid line represents the expected left collection fraction assuming the cut was made right down the middle of the foils. The dashed lines represent the expected left collection fractions for the cases where the cut is made just 10% to the left or right of center of the port diameter (i.e. $\sim 0.6\text{mm}$). Notice that the model appears to slightly underestimate the left collection fraction at the 30° port. A possible explanation for this will be discussed in Sec. 4.3.5. Otherwise, there is reasonable agreement between the first orbit loss model and the data.

$I_p=1.8$ MA Pitch Angle Distribution

Fig. 4.12(a) (analogous to Fig. 4.11) shows the comparison between the fraction of He detected in the left half of the foil stacks for the 22.5° and 67.5° ports of exposure D and the model prediction as a function of port orientation. Again, notice that the model appears to underestimate the left collection fraction at the 22.5° port. The observation at 67.5° is in good agreement with the model for 3.5 MeV α -particles lost with the pitch angle distribution calculated using the Lorentz ORBIT code. However, the majority of the loss detected by this port is the partially thermalized anomalous loss.

The PORT code was used to find the toroidal pitch angle for the anomalous loss that produces the best match to the observed left collection fraction. This assumes that the anomalous loss can be represented by a loss at a single pitch angle and single energy of 2.5 MeV. Fig. 4.12(b) shows that the measured left collection fraction, at $\sim 36\% \pm 5\%$, best matches the model for 2.5 MeV α -particles at a toroidal pitch angle of $\sim 63^\circ \pm 7^\circ$. The toroidal pitch angle of the fattest banana orbit χ_{fb} which corresponds to the boundary between passing and trapped particles was seen in Fig. 3.7 to occur at $\chi_{fb} \approx 56^\circ$ for $I_p = 1.8$ MA. Thus it is concluded that $\chi_{anom} > \chi_{fb}$ under the preceding assumptions.

The extent of the anomalous loss in pitch angle can be further narrowed down by

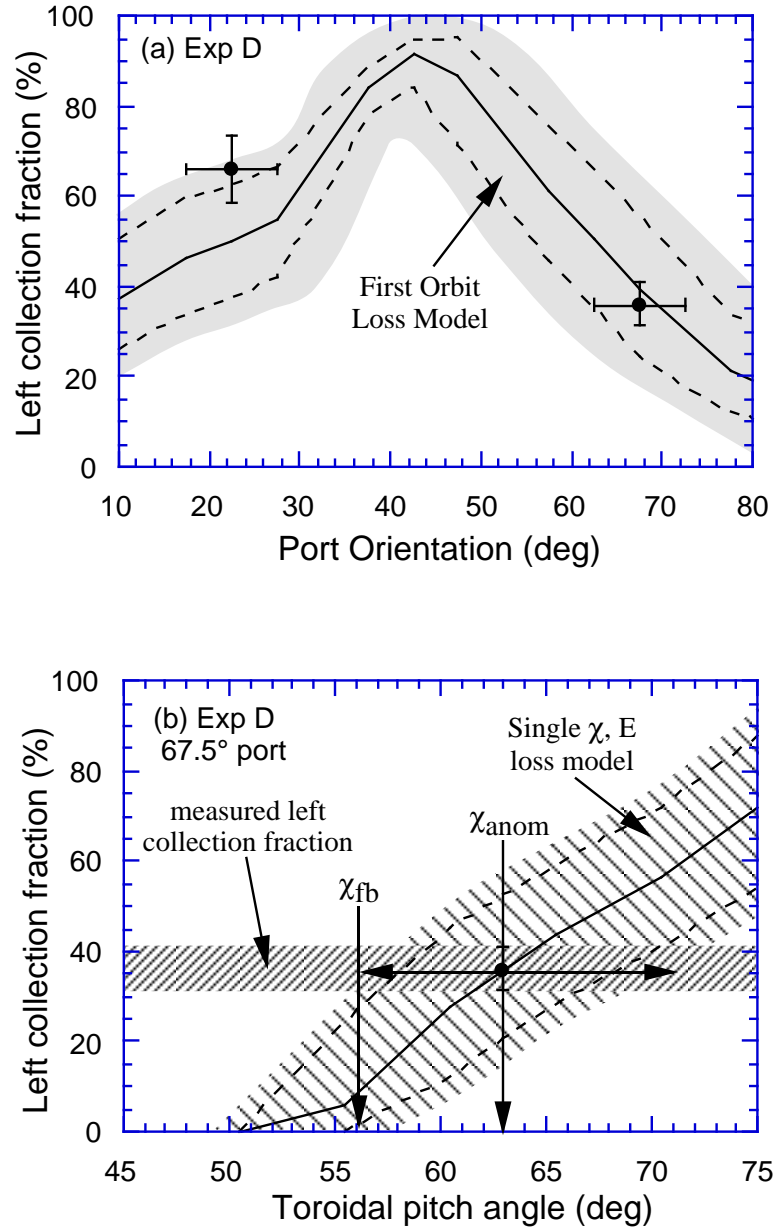


Figure 4.12: $I_p=1.8$ MA - (a) Left collection fraction as a function of port orientation for the upper row of the 22.5° and 67.5° ports of exposure D, analogous to Fig. 4.11. (b) Left collection fraction for the upper 67.5° port of exposure D fit to a model based on alpha loss at a single energy (2.5 MeV) and a single toroidal pitch angle as a function of this pitch angle. From the data, a toroidal pitch angle for the anomalous loss of $63^\circ \pm 7^\circ$ is inferred.

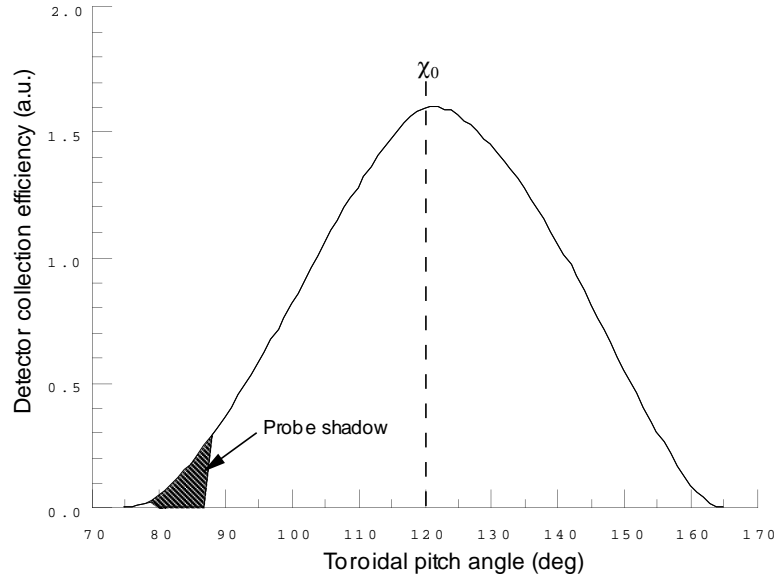


Figure 4.13: $I_p=1.8$ MA - Relative detector collection efficiency as a function of toroidal pitch angle for the 120° port of the original probe head design (exposure B). The collection efficiency drops off away from the pitch angle of the port axis (χ_0) due to collimation, and is cut off at $\pm 45^\circ$ either side of χ_0 . The probe shadow occurs near a true pitch angle of $\chi = 90^\circ$ ($\chi_t = \chi - \chi_{bt} \approx 85^\circ$) where the gyro-orbit of a high energy ion intercepts the probe head.

its absence in some of the detector samples. The pitch angle distributions of Fig. 4.6 for the exposures at a plasma current of 1.8 MA (B & D) show that there is no anomalous loss being detected by the 120° (112.5°) port of exposure B (D), indicating that the anomalous loss does not extend to pitch angles as large as first orbit loss as previously mentioned in Sec. 4.3.1. Fig. 4.13 shows the relative detector collection efficiency (i.e. the fraction of particles that reach the foil without being stopped by collimation), assuming flat pitch and gyro angle distributions, as a function of the toroidal pitch angle, $\chi_t = \chi - \chi_{bt}$ (Sec. 4.2.2), for the 120° port of exposure B for α -particles at 2.5 MeV (the representative anomalous loss energy). The pitch angle acceptance of $\pm 45^\circ$ for the original probe design, centered approximately about the port's orientation of 120° for exposure B can be seen in this figure. Incidentally, the data from this port represents the first experimental measurement of particles escaping to the TFTR wall on counter-going orbits (i.e. $\chi > 90^\circ$). Although the signals are small in the 120° ports, as evidenced in Figs. 4.5 through 4.9, the results

appear to be consistent with first orbit loss.

Also shown in 4.13 is the self-shadowing effect of the probe head. This shadowing is the result of insufficient displacement of an α -particle along the magnetic field line making the α -particle unable to clear the probe head in one gyro-orbit when the true pitch angle, χ , is near 90° ($\chi_{bt} = 4.6^\circ$ for a 1.8 MA exposure explains the shift away from $\chi_t = 90^\circ$ in Fig. 4.13). So, with the exception of a small degree of acceptance at 75° to 80° for exposure B, the effective minimum toroidal pitch angle cutoff occurs at $\chi_t > 87^\circ$. The use of the redesigned probe, with its smaller pitch angle acceptance range in exposure D, is slightly more restrictive. This sets the upper limit on the toroidal pitch angle of the anomalous loss at 87° .

Similarly, the toroidal pitch angle acceptance for the 30° (22.5°) port extends up to $\chi_t = 75^\circ$ (49.1°) for exposure B (D). Probe shadowing is not a factor in these ports since pitch angles near 90° are excluded. It was seen in Sec. 4.3.2 that the partially thermalized anomalous loss was detected in the 30° port of exposure B, but not in the 22.5° port of exposure D (although the anomalously large alpha fluence in this port is not fully understood). Thus the anomalous loss occurs at toroidal pitch angles $\chi_t < 75^\circ$, but not at $\chi_t < 49^\circ$. This sets the lower limit on the toroidal pitch angle of the anomalous loss, χ_{anom} , at 49° . Combining these results yields, $49^\circ \leq \chi_{anom} \leq 87^\circ$. It might, however, be expected that a feasible anomalous loss mechanism would preferentially provide either trapped or passing particles. Since the best fit in Fig. 4.12(b) gave $\chi_{anom} > \chi_{fb}$, trapped particles are probably the main constituent of the anomalous loss. It thus seems likely that the anomalous loss pitch angle distribution is concentrated in a narrow range above the passing-trapped boundary (i.e. $56^\circ < \chi_{anom} < 87^\circ$).

Pitch Angle Distribution to Lost Alpha Detector

The toroidal pitch angle distributions measured with the 90° lost alpha scintillator detector are shown in Fig. 4.14. For comparison, the Lorentz ORBIT generated pitch angle distributions are plotted after being corrected for the geometric and optical resolutions of the detectors. Notice that the model at $I_p=1.0$ MA in Fig. 4.14(a)

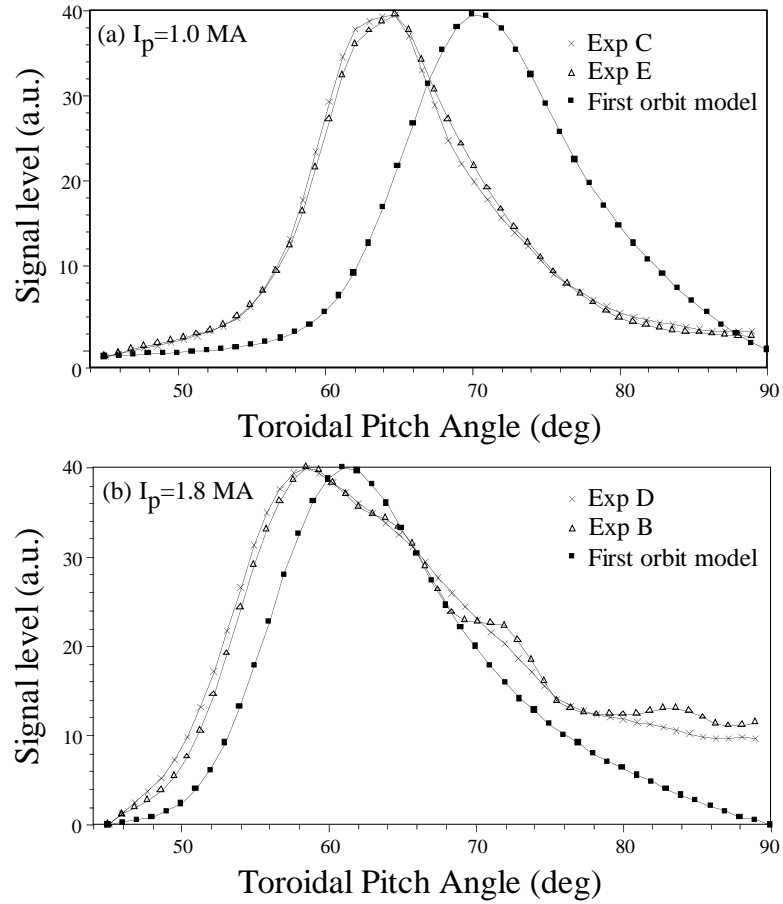


Figure 4.14: *Toroidal pitch angle distributions of alpha loss as measured with the 90° lost alpha scintillator detector averaged over gyroradius, from 3.5 to 9.9 cm, and time, from 3.4 to 3.7 s. Model curves are plotted for the ORBIT calculated first orbit loss after being corrected for the finite aperture sizes and optical resolutions of the detectors. The curves are normalized vertically to each other near their peaks, but the horizontal axes were absolutely calibrated by an in-vessel alignment to within $\sim 3^\circ$.*

tends to overestimate the toroidal pitch angle of first orbit loss (i.e. the model is shifted to the right of the measured distribution) by $\sim 6^\circ$. This discrepancy will be referred to in Sec. 4.3.5. The peaks of the $I_p=1.8$ MA distributions in Fig. 4.14(b), however, agree to within the 3° uncertainty associated with the scintillator detectors. The shapes of the model distributions are in reasonable agreement with the measured ones. The distribution at 1.8 MA appears to be somewhat wider than predicted, but there is no indication of an anomalously large loss occurring at a pitch angle above the fattest banana orbit.

4.3.4 Radial Distribution

$I_p=1.0$ MA Radial Distribution

It is apparent from Fig. 4.5 that the fluences of α -particles at a plasma current of 1.0 MA to the upper and lower rows of outboard ports are comparable. Fig. 4.15 shows the fluence levels for the 1.0 MA exposures (C & E) measured in layers 4–9 (representing first orbit loss) of the 75° upper and lower ports and compares them to the first orbit loss model as a function of detector height as measured from the midplane. The modeled fluence drops sharply about 1.0 cm outside the RF limiter radius due to the shadowing effect of the limiter. The shadow occurs outside of the RF limiter radius as a result of the combination of the outward bulge of the magnetic field (by ~ 1.5 mm [38]) between TF coils associated with TF ripple, and the downward drifts (∇B and curvature) that an α -particle experiences during its transit from the limiter to the probe. So, although the lower row of ports was placed below the RF limiter, these effects are sufficient to keep the lower ports out of the limiter shadow for first orbit loss.

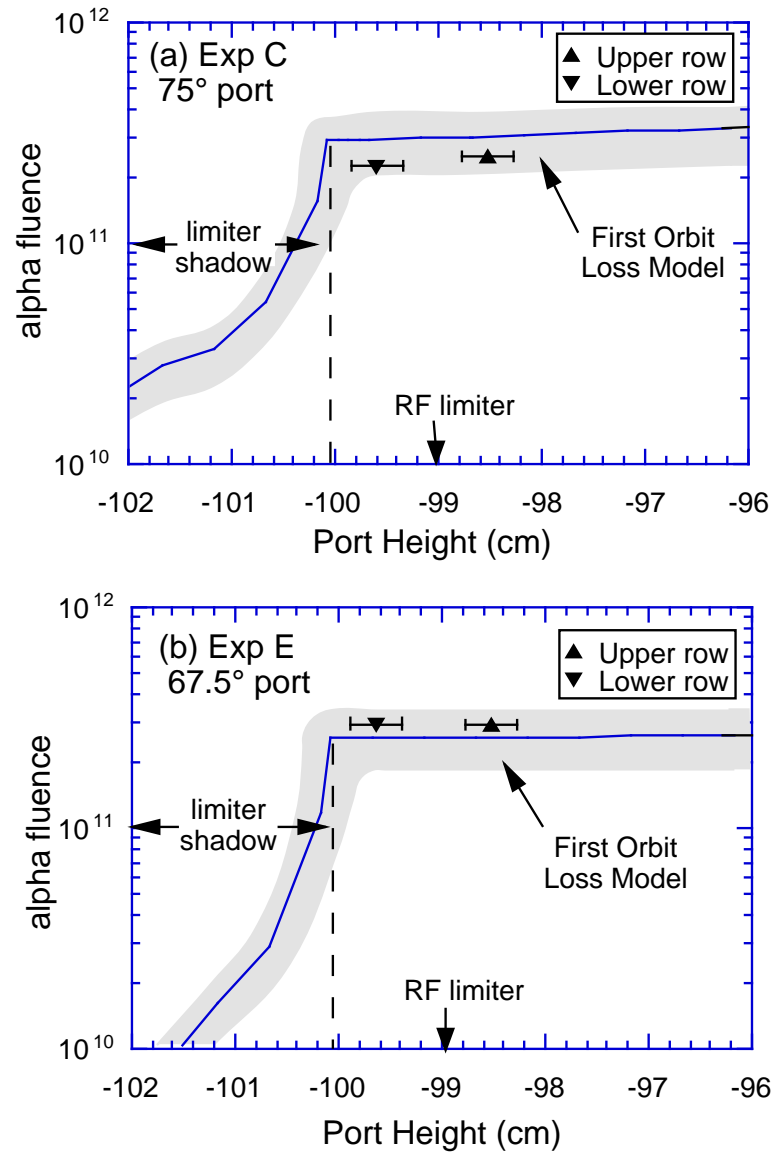


Figure 4.15: $I_p=1.0$ MA - Alpha fluence for layers 4 through 9 as a function of port height for the upper and lower rows of the (a) 75° port of exposure C, and (b) 67.5° port of exposure E. The RF limiter shadow begins ~ 4 mm below the midplane of the lower row.

$I_p=1.8$ MA Radial Distribution

Fig. 4.6 showed that the fluences of α -particles at a plasma current of 1.8 MA for the 30° and 75° ports drop by a factor of 3 or more between the upper and lower rows. Fig. 4.16 (analogous to Fig. 4.15) shows the fluence levels for the 1.8 MA exposures (B & D) of the 75° upper and lower ports and compares them to the first orbit loss model as a function of detector height. A strong radial dependence is clearly present among the 1.8 MA anomalous loss data. It is unclear whether this radial dependence is due to the RF limiter shadowing or a radial diffusive loss of α -particles. The shadowing effect of the limiter increases when the α -particle orbits stay closer to the magnetic field lines, as occurs with decreased α -particle energy, decreased α -particle pitch angle, or increased plasma current. Lorentz ORBIT code simulations show that for a 2.5 MeV α -particle, the limiter shadow is brought only ~ 1 mm closer to the RF limiter radius than is shown in Fig. 4.16 for first orbit loss, making it unlikely that the strong radial dependence is due solely to limiter shadowing. A diffusive loss having a finite random radial step-size between toroidal transits, could give rise to a radial dependence near absorbing boundaries such as the RF limiter and the probe head itself (Sec. 4.4.3). Further experiments that vary the radial position of the probe would be necessary to obtain a conclusive result. However, the strong radial dependence is further evidence that the 1.8 MA loss is not pure first orbit loss.

Radial Distribution to Lost Alpha Detector

The 90° scintillator detector with which the alpha collector results are compared is fixed in position such that a radial scan is not possible. As pointed out in Sec. 2.5.1, the pinhole aperture of the scintillator detector is located ~ 0.9 cm lower than the top of the lower row of the alpha collector. Therefore, the strong radial dependence of the anomalous loss might explain why it isn't observed on the 90° scintillator.

The scintillator detector located 20° below the outer midplane is, however, movable. Radial scans have been accomplished using this probe to investigate the diffusive nature of stochastic ripple diffusion (SRD) of fusion products. SRD (Sec. 2.3.2) causes

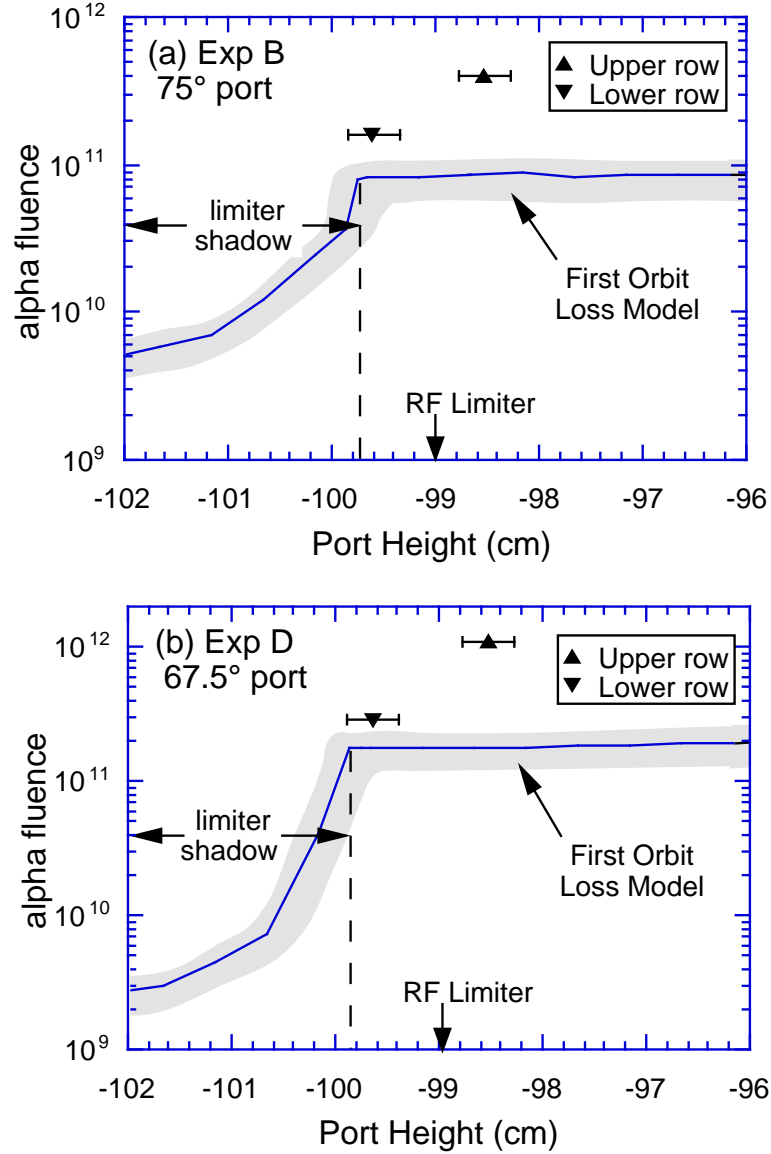


Figure 4.16: $I_p=1.8$ MA - Alpha fluence for layers 4 through 9 as a function of port height for the upper and lower rows of the (a) 75° port of exposure B, and (b) 67.5° port of exposure D. The RF limiter shadow begins only ~ 2 mm below the midplane of the lower row, possibly placing the lower row partially in the shadow. The decrease in the anomalous loss from the upper to lower row may be attributable to shadowing and/or a radial diffusive loss.

α -particles to be lost near their birth energy and can be the dominant loss mechanism in a narrow poloidal region about the outer midplane. These scans have shown a radial dependence of alpha loss comparable to that of the 1.8 MA anomalous loss observed using the alpha collector (i.e. \sim a factor of 3 decrease for ~ 1 cm radially outward movement near the RF limiter edge). There have not, however, been any indications of a partially thermalized loss to the 20° scintillator detector.

4.3.5 Uncertainties

The minimum experimental uncertainty in the alpha fluence measurement is estimated to be equal to the minimum detectable fluence of $\sim \pm 5 \times 10^8$ alphas per sample [32]. For Figs. 4.5, 4.6, 4.15, and 4.16, where the fluence of layers 4 through 9 (6 layers) are summed, the minimum uncertainty is $\sim 1.2 \times 10^9 (\approx \sqrt{6} \times 5 \times 10^8)$. For summed fluences $\geq 1.2 \times 10^{10}$ alphas, the experimental uncertainty is estimated to be $< \pm 10\%$ [32], corresponding approximately to the height of a data point (i.e. triangle symbol) on this semilog scale.

The 5° uncertainty in the port orientation assigned to the data points in Figs. 4.5, 4.6, 4.11, and 4.12(a), corresponds to ~ 2 mm on the circumference of the probe. This is the maximum misalignment that might be expected from the method used to align the probe head onto its base, combined with the uncertainty in the base alignment with respect to the vessel. The uncertainty in the port height assigned to the data points in Figs. 4.15 and 4.16 is 0.25 cm.

The error in the first orbit loss model represented by the shaded region in Figs. 4.5, 4.6, 4.15, and 4.16, is based on several uncertainties. First of all, the source and current profiles used by the Lorentz ORBIT code are taken from TRANSP for one time during the flat top portion in the discharge. These profiles are used to represent the plasma for the entire duration of the shot. Performing the calculation for other times throughout the discharge results in less than 15% variation in the total fluence calculation. So the choice of a single time near the time of maximum fusion rate should introduce

no more than 15% error. Another error in the first orbit loss model comes from converting the alpha collection fraction in α -particles per neutron to total loss fluence by multiplying by the global neutron production. The global neutron measurements have an $\sim 7\%$ error associated with them [39], which is transferred to the alpha fluence calculation. Combining these uncertainties, along with other sources of uncertainty such as the accuracy of the TRANSP profiles, the overall minimum error in the first orbit loss model is estimated to be $\pm 30\%$. This uncertainty is based on the modeling of the 75° port. The 22.5° port can have substantially more error since the main contribution of α -particles to this port is from co-going α -particles born near the edge of the plasma (e.g. the 40° orbit of Fig. 3.7), and is thus extremely sensitive to uncertainties in the source profile which can greatly affect the source term at the edge. The 75° port fluences are dominated by α -particles lost near the fattest banana orbit which pass closest to the magnetic axis where the source profile is peaked and are thus not as sensitive to the shape of the profile. The uncertainty due to the source profile was estimated using the results of a sensitivity analysis in which a parabolic to a power source profile was assumed: $S(r) = S_0(1 - (r/a)^2)^{i_s}$, where $S(r)$ is the source profile as a function of minor radius r , S_0 is the alpha source term at the magnetic axis, a is the edge minor radius, and i_s is the source term peaking exponent. The Lorentz ORBIT calculated alpha collection fraction was evaluated for $i_s = 8 \pm 1$, a common value for the peaking exponent with a reasonable uncertainty. Where the alpha collection fraction varied by more than $\pm 30\%$, the higher uncertainty due to source profile sensitivity was used.

The first orbit model also incorporates a $\pm 5^\circ$ uncertainty in the port orientation which comes about due to uncertainties in the plasma current profile and modeling inaccuracies of the vacuum magnetic field in the Lorentz ORBIT code. As illustrated in Fig. 4.14, the first orbit model does not match the pitch angle distribution measured by the scintillator in the 1.0 MA case. Correcting this overestimate would roughly correspond to a shift of the model distributions to the left by $\sim 5^\circ$. The agreement between the data and the model for the 1.0 MA distributions, shown in Figs. 4.5 and 4.11, would be improved by such a shift. To account for this uncertainty, the first orbit model is given a $\pm 5^\circ$ spread.

The uncertainty in the left collection fraction data of Figs. 4.11 and 4.12 is based

on comparing the maximum and minimum possible measured alpha fluences, using a measurement uncertainty of the larger of $\pm 1.2 \times 10^9$ α -particles or $\pm 10\%$, for the left and right halves.

4.4 Discussion

4.4.1 Summary of Experimental Results

Measurements of escaping α -particles were made using the alpha collector probe for plasma currents of 1.0 and 1.8 MA. The He released from foil layers 4 through 9, which should be representative of first orbit lost α -particles, was then compared to a first orbit loss model with respect to the total alpha fluence implanted into these foils, and the energy, pitch angle and radial distributions inferred from the measured loss. The comparison at 1.0 MA indicates that the measurement from layers 4 through 9 is consistent with the first orbit loss model for 3.5 MeV α -particles. The shallow layers (2 through 3), however, suggest that a small ($\sim 1/3$ the fluence of first orbit loss), low energy (< 2.0 MeV) anomalous loss feature may be occurring at this plasma current.

The comparison at 1.8 MA reveals a partially thermalized loss with a total alpha fluence nearly an order of magnitude ($\approx 7\times$) larger than that of the first orbit loss model and a wide energy distribution peaked at $\sim 2.5 \pm 0.3$ MeV (i.e. $\sim 30\%$ below the birth energy of 3.5 MeV). The pitch angle distribution of the inferred anomalous loss appears to occur in a narrow region above the passing-trapped boundary ($\chi_{fb} \approx 56^\circ$) and is peaked at a toroidal pitch angle of $\sim 63^\circ \pm 7^\circ$. This anomalous loss drops by approximately a factor of 3 in magnitude from the upper row to the lower row of collimating ports (separated by ~ 1.1 cm), in contrast to the first orbit loss model which remains nearly constant between the two rows. There is no evidence of this anomalous loss on the 90° lost alpha scintillator detector.

4.4.2 Comparison of 1.8 MA Anomalous Loss with Delayed Loss

The anomalous results obtained with the alpha collector probe are qualitatively similar to an anomalous loss feature called ‘delayed loss’, which is not yet understood [40]. Delayed loss is observed with the 90° lost alpha scintillator detector for DD fusion products (i.e. 3 MeV proton, and 1 MeV triton) in DD plasmas. Delayed loss, however, has not been observed with the scintillator detectors for DT α -particles [9]. The following is a list of the observed characteristics of delayed loss and how they compare to the anomalous loss observed with the alpha collector probe.

1. Delayed loss is seen at the scintillator detector located 90° poloidally below the outer midplane (i.e. at the bottom of the TFTR vessel), but not at the 20°, 45° nor 60° detectors. This is consistent with the current results in that the measurements made with the alpha collector probe were only made at the bottom of the vessel.
2. The delayed loss to the 90° scintillator detector has a strong dependence on the plasma major radius, being largest at the small major radius of $R=2.45$ m, and disappearing at $R > 2.55$ m. Again, this is consistent with the current results in that the measurements made with the alpha collector probe were made in $R=2.45$ m plasmas. The alpha collector was used only in these small plasmas to minimize probe heating by maximizing its distance from the plasma. The design does allow its use in up to $R=2.52$ m plasmas, but no exposures were done at this radius.
3. The strength of delayed loss increases with respect to the first orbit loss with increased plasma current, becoming dominant above 1.8 MA. This is consistent with the result that only first orbit loss (with the exception of a small anomalous loss feature at low energy) was observed at 1.0 MA, but a large anomalous loss, in addition to first orbit loss, was observed at 1.8 MA using the alpha collector probe. The total loss (first orbit plus delayed loss) in DD at 1.8 MA as measured with the 90° scintillator detector was about a factor of 2 above the expected

first orbit loss [40], as compared to a factor of 7 for the alpha collector in DT at 1.8 MA.

4. The energy of delayed loss particles is about half (i.e. $55\pm 15\%$ [40]) that of the prompt first orbit loss, as inferred from the gyroradius of its scintillator impact. This is consistent, within the energy resolution of the detectors, with the $\sim 70\pm 10\%$ of birth energy inferred for the anomalous loss of the alpha collector.
5. Delayed loss at $I_p=1.8$ MA occurs at a pitch angle approximately 10° above that of the fattest banana orbit. This is roughly consistent with the anomalous loss pitch angle inferred to be $\sim 7^\circ\pm 7^\circ$ above the fattest banana pitch angle of 56° .
6. Delayed loss is delayed by $\sim 200\pm 100$ ms with respect to the usual first orbit loss, as can be seen most clearly at the beginning and end of neutral beam injection. The time resolution of the alpha collector is limited to a single discharge since it integrates α -particles over an entire shot. Thus this feature of delayed loss can not be checked with the alpha collector. However, the inferred energy of $\sim 70\pm 10\%$ of the birth energy for the anomalous loss requires a delay of ~ 100 ms for them to slow down to this energy (assuming an energy e-folding time of ~ 200 ms) consistent with delayed loss.
7. Delayed loss increases slowly with NBI power at a fixed plasma current. The alpha collector exposures were all done at an NBI power of ~ 10 MW. Thus a comparison of the NBI power dependence of the two anomalous losses can not be made. The design of the collector probe does allow its use in full power discharges, making a beam power scan possible, but such a scan was not done.
8. For $R=2.45$ m and $I_p=1.8$ MA plasmas, delayed loss to the 90° scintillator detector is of the same order of magnitude as first orbit loss in DD plasmas, but is absent in DT plasmas. The anomalous loss to the alpha collector appears to be about a factor of 6 times larger than first orbit loss in DT plasmas. The alpha collector is not capable of detecting DD fusion products. The lack of detectable levels of delayed loss on the scintillator detector in DT plasmas but apparently large levels in the alpha collector is most likely due to the different radial positions of the two probes. The lower row of the alpha collector extends

nearly 1 cm farther into the vessel than does the pinhole aperture of the 90° scintillator detector (Sec. 3.5). The strong radial dependence of the anomalous loss, seen in the upper/lower row comparisons of Fig. 4.16, may be sufficient to make it an insignificant contribution to the loss observed by the scintillator detector. Their different toroidal positions relative to toroidal asymmetries in the vessel such as limiters and the path of neutral heating beams may also be a factor.

It may be significant to note that the delayed loss features changed significantly when the 90° scintillator detector was repositioned after the 1990 run to accommodate the installation of a new poloidal RF limiter [40]. Previously, the detector aperture was located about 4 cm radially outside (i.e. below) and about 120° toroidally from the edge of the nearest limiter. The new limiter was installed only 45° toroidally from this detector which forced a relocation of its aperture to only about 1 cm below the edge of this new limiter to avoid shadowing of the aperture [41]. After the repositioning, the delayed loss feature increased in magnitude (by a factor of ~ 4 at $I_p=1.8$ MA) and peaked at a pitch angle closer to the passing-trapped boundary. The implication was that after its repositioning, the 90° detector collected more anomalous delayed loss at low pitch angles than it had previously, presumably because these ions had not reached the aperture of the detector in the 1990 run. The first orbit loss features remained essentially unchanged between the two runs. This demonstrates the fact that delayed loss is extremely sensitive to the relative positioning of a detector at 90° and the obstacles that fusion products may encounter such as RF limiters.

The similarities between delayed loss and the anomalous loss observed with the alpha collector imply that they may be due to the same loss mechanism. In Sec. 4.5 some of the possible loss mechanisms are considered.

4.4.3 Trajectories of anomalous loss orbits

The trajectory of an α -particle's last orbit prior to intersection with the detector can be calculated using the Lorentz ORBIT code. Fig. 4.17 shows the last orbit traced

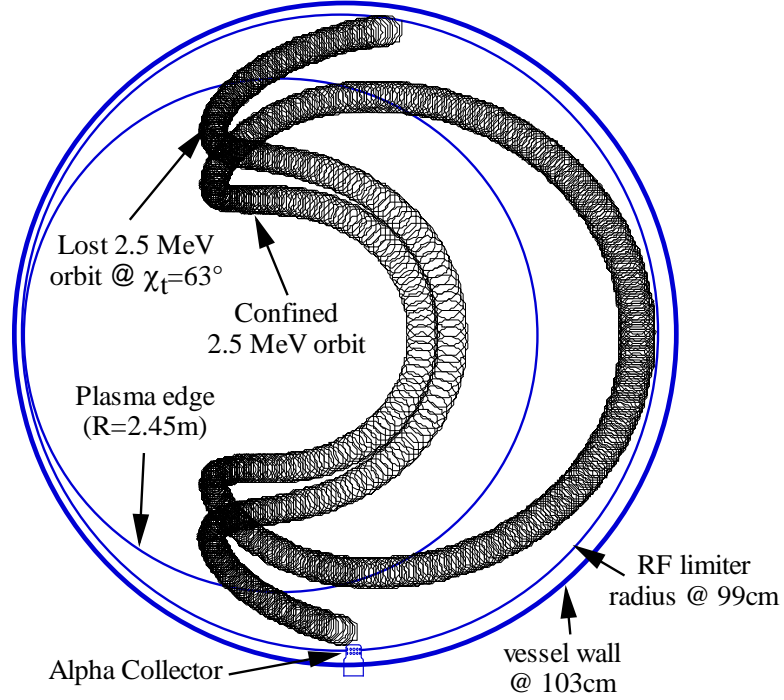


Figure 4.17: Trajectories in a $R=2.45$ m, $I_p=1.8$ MA plasma of an anomalous loss orbit (2.5 MeV, $\chi_t=63^\circ$) that strikes the detector at the bottom of the TFTR vessel and a marginally confined orbit with the same parameters that just misses the RF limiter at the outer midplane. The banana tips of the two orbits are displaced by ~ 17 cm.

backwards in time from the alpha collector at the bottom of the vessel to an RF limiter at the top of the vessel for an α -particle at $E = 2.5$ MeV and $\chi_t=63^\circ$ (the parameters inferred for the anomalous loss) for the $R=2.45$ m, $I_p=1.8$ MA discharge of exposure B. Also shown in Fig. 4.17 is a marginally confined orbit of the same energy which was started with an upward vertical displacement of the lower banana tip of ~ 17 cm with respect to the last orbit. The outer leg of this confined orbit just barely misses the projection of the RF limiter (centered at $R=2.61$ m with a minor radius of 0.99 m) near the outer midplane. Thus, confined orbits with banana tips just below this one intersect the wall just below the outer midplane. Therefore, the anomalous loss orbits detected at 90° could be brought there by a relatively large vertical step on the last bounce of a previously confined trapped orbit, while smaller vertical steps would cause the loss to occur nearer the outer midplane, as is the case

for stochastic ripple diffusion [10].

A detailed study of many such anomalous loss orbits such as those in Fig. 4.17 has shown that the vertical displacement of the lower banana tip required for a previously confined orbit to reach the alpha collector at the bottom of the vessel (for $E = 2.2$ to 2.8 MeV alpha orbits within $\chi_t = 56^\circ - 70^\circ$) is at least 15 cm. Such a large step-size, however, is inconsistent with the observed radial dependence of the anomalous loss. The 1.1 cm separation between the upper and lower rows of ports is much less than the required step-size of >15 cm. Thus there should be little variation in the alpha fluence between the rows, but measurements show a factor of 3 difference between the upper and lower row.

If α -particle orbits could scrape off at the bottom of the vessel (rather than at the outer midplane) as they diffuse outwards, then small step-size radial diffusion could explain the observed radial dependence and absence of the anomalous loss on the scintillator detectors. However, as can be inferred from Fig. 4.17, the probe would have to be placed ~ 20 cm further into the vessel to intercept a marginally confined α -particle orbit with the anomalous loss parameters. A smaller banana width could allow an α -particle orbit to strike the bottom of the vessel first, but this would require an α -particle energy of ~ 0.3 MeV, less than the minimum detectable energy of the alpha collector. But if, for the sake of argument, one assumes that there are orbits that strike the bottom of the vessel first as they diffuse radially outwards, then the radial dependence of the anomalous loss can be used to calculate a diffusive step-size. Assuming that at every bounce the particles walk randomly with a step-size of b , and that they will be scraped-off by an obstacle (such as the RF limiters or the probe head) with a probability P_l , the α -particle flux at a distance x behind the obstacle is $I(x) = I_0(1 - P_l)^N$, where I_0 is the α -particle flux at $x=0$, and $N = (x/b)^2$ is the number of bounces needed for the particle to randomly walk the distance x [42]. The probability of scrape-off is estimated to be the ratio of the toroidal extent of the obstacles above x to the toroidal circumference of the vessel. It can easily be shown that the scrape-off on the probe head is insignificant compared to the scrape-off on the RF limiters. For the lower row of ports, with $x=0.6$ cm and $P_l \approx 0.13$ (eight limiters that each have a toroidal extent above x of ~ 27 cm), the factor of 3 between rows results in a step-size of ~ 0.2 cm. Diffusion at this step-size down to the location of

the scintillator detector, with $x=1.2$ cm and $P_l \approx 0.19$ (toroidal extent of each limiter above x increased to ~ 39 cm) occurs with a flux reduction by a factor of ~ 2000 with respect to the upper row of ports, consistent with the absence of anomalous loss to the 90° scintillator detector.

A step-size of 0.2 cm per bounce corresponds to a diffusion coefficient, $D = b^2/\tau_b$, of ~ 0.4 m²/s, where $\tau_b \approx 10\mu\text{s}$ is the bounce period. This results in a time scale for diffusion to the wall, $\tau_D \approx a^2/4D$, of ~ 0.6 s. Assuming all the alphas diffuse at this rate, $\sim 30\%$ of the α -particles should be lost to the wall within one energy e-folding time. However, small step-size diffusion to the bottom of the TFTR vessel probably isn't realistic since it is not consistent with high energy orbits that tend to scrape-off near the midplane. A larger step-size would result in a larger global loss, however, there would likely be a threshold condition such that not all of the α -particles are included in the diffusive process. Thus, without knowing the loss mechanism, it is difficult to estimate the global loss associated with the observed anomalous loss.

The large step-size of 17 cm inferred from the orbits of Fig. 4.17 is consistent with the 15 cm that was estimated in the same manner in Ref. [40] for delayed loss of 1.5 MeV (half the birth energy) DD fusion protons to the 90° scintillator detector for a $R=2.45\text{m}$, $I_p=2.0$ MA discharge. Thus the arguments as to the unlikeliness of pitch angle scattering, TF ripple, and MHD as possible causes of delayed loss [40] also apply to the 1.8 MA anomalous loss observed with the alpha collector probe, and will thus only be briefly summarized in the next section. Several new possibilities that attempt to explain the anomalous loss are also considered in the next section.

Possible explanations:	Anomalous loss features:					
	a) absence on 90°scintillator	b) I_p dependence	c) total fluence	d) energy distribution	e) pitch distribution	f) radial distribution
1) Collisional Loss	X	?	X	O	X	?
2) TF ripple	?	?	X	X	O	?
3) MHD	?	?	X	?	?	?
4) CX Loss	X	O	O	O	O	X
5) I_p ramp down	X	O	O	X	?	?
6) Scattering	?	X	X	O	?	O
7) Activation	O	X	X	?	X	?
8) Foil surface fusion	X	X	X	O	?	O
9) Dif'n of residual He	O	X	?	X	?	O
10) Dif'n of implanted He	O	X	X	X	?	O

X - Inconsistent, O - Consistent, ? - Undecided

Table 4.2: *Anomalous Loss Explanations*

4.5 Possible Anomalous Loss Mechanisms

A model attempting to explain the mechanism responsible for the anomalous loss observed with the alpha collector would have to be consistent with the following features:

- (a) Absence of anomalous loss on the 90° lost alpha scintillator detector in DT.
- (b) I_p dependence - occurs at 1.8 MA but not at 1.0 MA.
- (c) Total fluence - ≈ 6 times larger than first orbit loss.
- (d) Energy distribution - peak $\sim 2.5 \pm 0.3$ MeV inferred from shallow range distribution.
- (e) Pitch angle distribution - peak $\sim 7 \pm 7^\circ$ above the passing-trapped boundary, and most likely concentrated in narrow region above this boundary.
- (f) Radial dependence - factor of 3 decrease from upper to lower row (separated by 1.1 cm).

The anomalous loss mechanisms described in the following sections are summarized in Table 4.2 with respect to their consistency with the observed loss features.

4.5.1 Collisional Loss

The ~ 0.2 sec time delay observed on the 90° scintillator detector for delayed loss suggests a classical collisional loss mechanism, since this time is on the order of the slowing down time for fusion products [34]. Although large pitch angle scattering is capable of causing a confined orbit to become lost, it is too infrequent to be of significance, occurring on a time scale of >10 sec.

Small pitch angle scattering of barely passing α -particles into the first orbit loss cone can generate a diffusion of α -particles across the passing-trapped boundary, resulting in collisional nonprompt loss (Sec. 2.4.1). The α -particles that are subsequently lost should be marginally trapped, i.e. they should appear at the detector at the pitch angle of the passing-trapped boundary ($\sim 56^\circ$ at 1.8 MA). However, delayed loss is seen to occur at pitch angles clearly above the passing-trapped boundary. This also appears to be the case with the alpha collector anomalous loss at 1.8 MA (Sec. 4.3.3). Furthermore, models consistently predict small loss fractions for collisional loss relative to first orbit loss. For instance, Ref. [34] reported a TRANSP prediction for an $R=2.45$ m, $I_p=1.6$ MA TFTR discharge of a global loss due to collisions of α -particles of 0.35%, which was only $\sim 5\%$ of the calculated first orbit loss fraction for that shot.

4.5.2 Toroidal Field (TF) Ripple Effects

There are at least two different mechanisms through which TF ripple can cause radial transport of fast ions (Sec. 2.3.2). Stochastic ripple diffusion (SRD) [12] is a collisionless process which produces a radial step near the banana tip of those trapped particles that meet a particular threshold criterion. The maximum vertical step-size for 2.5 MeV α -particles in the conditions of discharge B can be shown to be ≈ 5 cm, in a manner similar to the calculation of Ref. [40] that estimated a ≈ 3.5 cm maximum step-size for 1.5 MeV protons in a 2 MA plasma. Therefore, even if a trapped particle passes through two banana tips before passing near the midplane, it can only gain up to a maximum of 10 cm outward displacement, significantly less than the 17 cm

necessary to reach the alpha collector at the bottom of the vessel (Sec. 4.4.3). This relatively small step-size is such that almost all of the SRD loss should be localized within 30° of the outer midplane [10].

A synergistic enhancement of fast ion diffusion has been found for SRD with collisions [13]. This effect is simulated using the Hamiltonian guiding center drift orbit Monte Carlo code, gc-ORBIT [43] (not to be confused with the Lorentz ORBIT code). Under the conditions of the 1.0 MA discharges, this code predicts a global alpha loss of $\sim 25\%$. Only $\sim 15\%$ of this global loss is ‘delayed’ (i.e. occurring below 3.5 MeV). For the conditions of the 1.8 MA discharges, this code predicts a global alpha loss of $\sim 4\%$, of which only $\sim 21\%$ is ‘delayed’. Thus, the synergistic enhancement is not of sufficient magnitude to make the ‘delayed’ losses at 1.8 MA much more significant than they are at 1.0 MA. Furthermore, these ‘delayed’ losses are clearly peaked poloidally within 30° below the outer midplane. It should be noted, however, that preliminary work involving improved modeling of the magnetic field in the vacuum gap region between the plasma and the first wall, by a group at the Kiev Institute for Nuclear Research, has indicated the possibility of half-energy alphas reaching the 90° detectors through this mechanism [44].

The other TF ripple effect that can cause radial transport of fast ions is super-banana trapping inside the ripple wells [40]. Particles lost through ripple well trapping would have pitch angles very close to 90° , causing most of them to be self-shadowed by the probe head, as shown in Fig. 4.13. Note that a true pitch angle of 90° corresponds to a toroidal pitch angle of $\sim 85^\circ$ due to the $\sim 5^\circ$ offset between true and toroidal pitch angles (Sec. 4.3.3). The detection of the partially thermalized anomalous loss in the foil stack in the 30° collimating port of exposure B (Fig. 4.6(b)) indicates that the anomalous loss extends down to toroidal pitch angles below 75° (Sec. 4.3.3). Furthermore, the left collection fraction analysis of Sec. 4.3.3 gives an estimate of $63^\circ \pm 7^\circ$ for the toroidal pitch angle of the anomalous loss, slightly smaller than the $\sim 70^\circ$ measured by the 90° scintillator detector for delayed loss. Ref. [40] concluded that it was unclear how particles lost through this mechanism could arrive at the detector with pitch angles this small. Most importantly, a loss of ripple well trapped particles at a true pitch angle of $\sim 90^\circ$ would have a better likelihood of implanting into the foils in the 120° port than in the 75° port because the 75° port has a larger self-shadowing

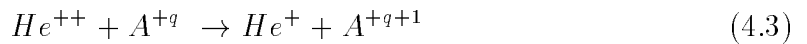
effect. However, the anomalous loss is not detected in the 120° foils. Thus, it seems unlikely that ripple well trapping could provide an explanation of the anomalous loss.

4.5.3 MHD Effects

The two mechanisms by which magnetic perturbations due to MHD activity can cause radial transport of high energy particles were considered with respect to delayed loss in Ref. [40]. These mechanisms are the parallel drift of the ion along radially perturbed field lines, and the perpendicular drifts across the field lines. Both the former mechanism and a non-resonant interaction of the latter, required an unrealistically large magnetic perturbation of $\tilde{B}_r/B_t \approx 10^{-2}$ to achieve a 10 cm step-size [40], where \tilde{B}_r is the local radial magnetic perturbation. The magnitude of normal magnetic perturbations inside plasmas is generally $\tilde{B}_r/B_t \approx 10^{-4}$ [45, 46]. Similarly, orbits resonant with the perturbation required the largest MHD perturbations in TFTR [40]. Thus it was concluded that the effects of some hidden MHD activity during seemingly MHD quiescent plasmas cannot easily explain the large last step necessary to bring the escaping orbit to the 90° detector [40]. This conclusion applies equally well to the MHD quiescent discharges conducted for the alpha collector exposures as it did to discharges examined for delayed loss.

4.5.4 Loss of He^+ from Charge Exchange with Impurities or NBI Neutrals

Another possibility is that fully stripped α -particles charge exchange (CX) with partially stripped impurities producing singly ionized α -particles through:



where A^{+q} are plasma impurity ions. The singly ionized α -particle then has twice the gyroradius it had before charge exchange, resulting in a doubling of its banana width.

The orbits of previously confined α -particles may suddenly transition to prompt loss trajectories that take some of the α -particles to the detector.

Olson [47] concluded that for a 0.1% low charge state impurity concentration of oxygen (i.e. $\sim 1 \times 10^{11} \text{ cm}^{-3}$) in TFTR, the average time for single electron capture for 2.0 MeV He^{++} is ≈ 5 ms. This is much less than the ~ 200 ms alpha slowing down time and hence could cause a net diffusion to the walls and be a previously unrecognized mechanism for α -particle transport in TFTR.

With the addition of carbon tiles, the main impurity in TFTR is now carbon, not oxygen. At $Z_{eff} \approx 1.5$ the impurity concentration for carbon is $\approx 5\%$, with roughly the same radial profile as the electron density. At electron temperatures ~ 10 keV most of this carbon is fully stripped (C^{+6}) in the core. PPPL's MIST code solves for the density of ions in each charge state using atomic physics appropriate for these low-density high-temperature plasmas [48]. MIST predicts a H-like carbon (C^{+5}) concentration of $\sim 5 \times 10^9 \text{ cm}^{-3}$ ($\sim 0.01\% n_e$) in the core, which increases by a factor of ~ 30 at the cooler plasma edge. The lower charge states of carbon are present in the core at concentrations reduced by a factor of 1000 or more in relation to C^{+5} .

Charge exchange cross sections calculated for the $He^{++} + C^{+5}$ collision system using two different methods are shown in Fig. 4.18. The classical-trajectory Monte-Carlo (CTMC) [49] method may not be appropriate in the energy range being considered due to unphysical capture to deeply bound states that only exist classically, resulting in cross sections that may be unrealistically large by up to a factor of about 5 at ~ 2.5 MeV. A coupled-Sturmian (CS) calculation was done at Pennsylvania State University [50, 51] to check on the magnitude of this uncertainty. Fig. 4.18 shows the CTMC results to be a factor of ~ 3 times larger than the CS results for 2.5 ± 1.0 MeV, the energy range of interest for the anomalous loss. The calculations of this section are based on the CTMC results which were obtained first, although they are probably less reliable. While these calculations support charge exchange loss as being consistent with anomalous loss features b–e of Table 4.2 (as discussed in the remainder of this section), features a and f are not supported by this mechanism. Therefore it was not deemed necessary to repeat the calculations using the CS results.

The CTMC charge exchange cross section is seen in Fig. 4.18 to be $\approx 1.3 \times$

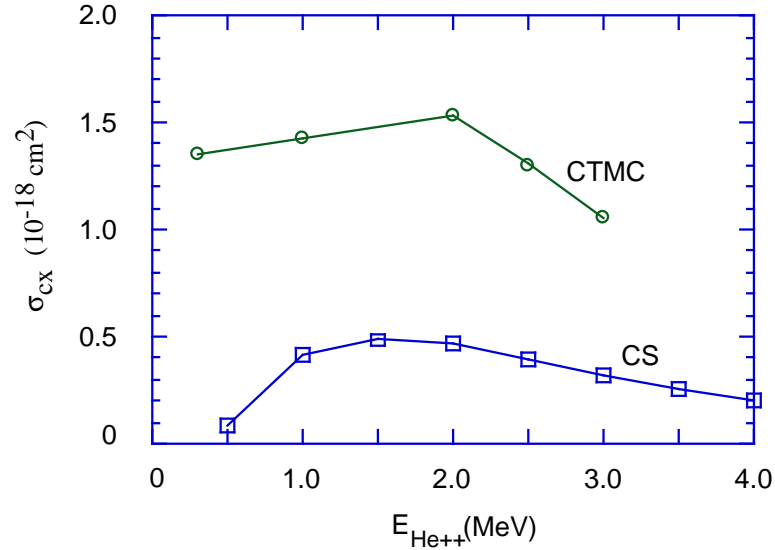


Figure 4.18: Calculated single electron capture cross section for the $\text{He}^{++} + \text{C}^{+5}$ collision system using the classical-trajectory Monte-Carlo method (CTMC) and the Coupled-Sturmian treatment (CS).

10^{-18} cm^2 for alphas at 2.5 MeV. This results in a collision period for charge exchange of 2.5 MeV α -particles in the core of $\tau_{\text{cx}} \approx 150 \text{ ms}$, which is of the same order as the alpha energy e-folding time, and a period of $\tau_{\text{cx}} \approx 5 \text{ ms}$ at the edge. Based on the CTMC calculations, therefore, charge exchange can be a significant factor in the evolution of α -particle orbits as they slow down.

Charge Exchange Orbits

Fig. 4.19 illustrates possible alpha orbit transitions due to charge exchange in a 1.8 MA plasma (exposure B) that can cause previously confined α -particles to strike the detector at the bottom of the vessel. Fig. 4.19(a) depicts a 2.5 MeV trapped α -particle that picks up an electron through charge exchange as it crosses the outer midplane on its counter-going leg and is subsequently lost to the detector. Fig. 4.19(b) depicts a 2.5 MeV counter-going passing α -particle that also charge exchanges as it crosses the outer midplane and is subsequently lost to the detector. A similar figure would show that co-going passing α -particles that charge exchange as they cross the

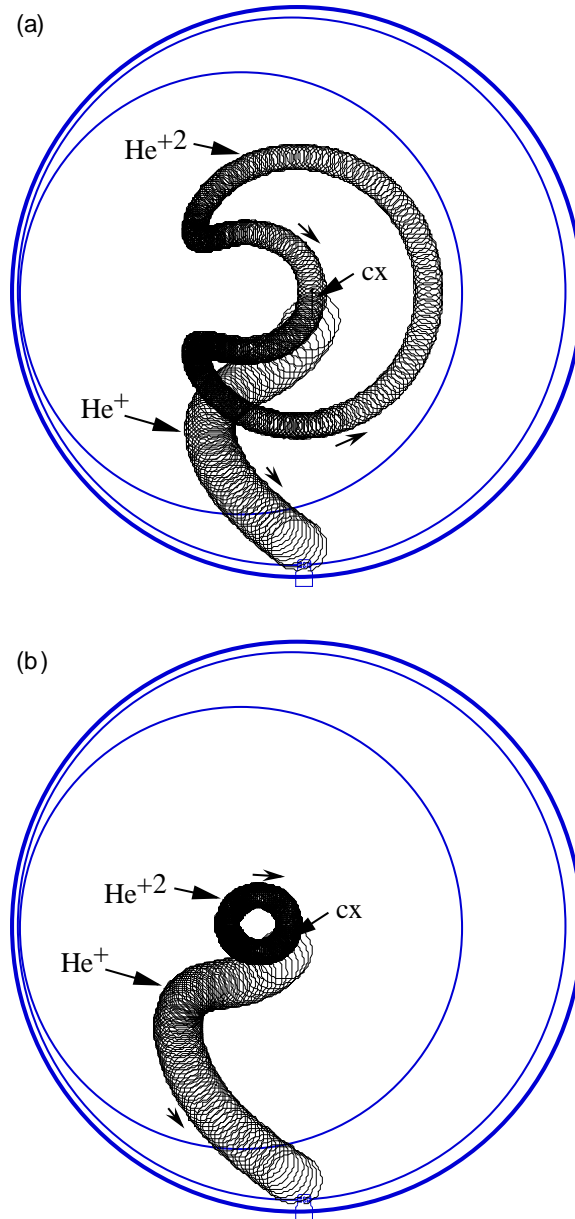


Figure 4.19: 2.5 MeV α -particle orbit transitions that take α -particles to the detector at 90° in $R=2.45 \text{ m}$, $I_p=1.8 \text{ MA}$ plasmas for α -particles charge exchanging (cx) at (a) the outer-midplane crossing point of the counter-going leg of a trapped particle ($R=270 \text{ cm}$, $\chi_t=63.5^\circ$), and (b) the outer-midplane crossing point of a counter-going passing particle ($R=260 \text{ cm}$, $\chi_t=65.3^\circ$). Small arrows show direction of guiding center motion.

inner midplane can also be subsequently lost to the detector on a co-going trajectory.

Fig. 4.20 illustrates what happens when α -particles charge exchange on the opposite side of orbits similar to those of Fig. 4.19. Fig. 4.20(a) shows that a 2.5 MeV trapped α -particle charge exchanging as it crosses the outer midplane on its co-going leg results in an orbit that passes closer to the magnetic axis. Similarly, Fig. 4.20(b) shows a 2.5 MeV counter-going passing α -particle that charge exchanges as it crosses the inner midplane also resulting in slight inward radial transport. Again, a similar figure would show that co-going passing α -particles that charge exchange as they cross the outer midplane also transport inwards. These particles are quickly reionized by the background plasma within a few poloidal transits, since the collision period for reionization in the core of $\sim 5\mu\text{s}$ [31] is on the order of the bounce frequency of $\sim 10\mu\text{s}$. The lost orbits of Fig. 4.19, however, reach the detector within $\sim 3\mu\text{s}$, spending very little time in the core where the plasma density is peaked, and thus have a much lower probability of being reionized.

Figs. 4.19 and 4.20 represent the extremes in the orbit transitions possible through charge exchange. Charge exchange at other locations along an orbit results in less radial transport. A series of successive charge exchanges and reionizations could result in a large step-size radial diffusive process. However, as discussed in Sec. 4.4.3, the large radial step-size needed to bring the orbits to the detector is inconsistent with the factor of 3 reduction in fluence between the upper and lower rows of ports. It is not obvious how charge exchange loss could account for the radial dependence and absence of anomalous loss on the lost alpha scintillator detectors in DT. The larger downward drifts associated with the larger gyroradius of the He^+ should make shadowing by the nearby RF limiters less effective, and hence allow the charge exchange lost particles to easily reach the lower row of collimating ports on the alpha collector and the scintillator detector.

Plasma current dependence

Fig. 4.21 is a plot of toroidal pitch angle vs. r/a for the outer midplane crossing point

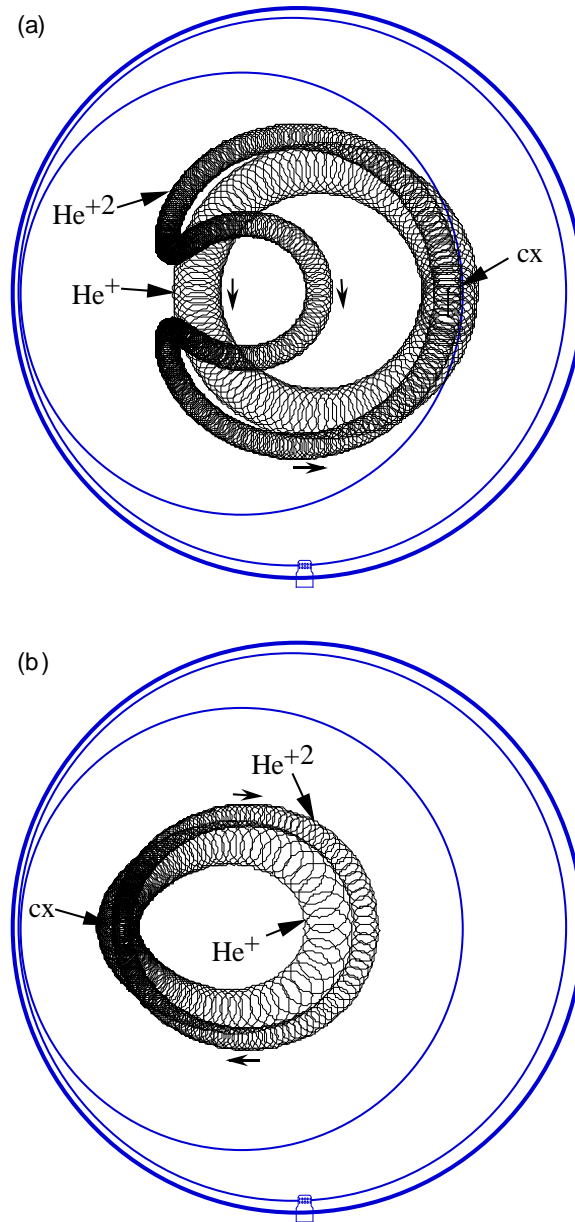


Figure 4.20: 2.5 MeV α -particle orbit transitions in $R=2.45 \text{ m}$, $I_p=1.8 \text{ MA}$ plasmas for α -particles charge exchanging (cx) at (a) the outer-midplane crossing point of the co-going leg of a trapped particle ($R=320 \text{ cm}$, $\chi_t=124^\circ$), and (b) the inner-midplane crossing point of a counter-going passing particle ($R=200 \text{ cm}$, $\chi_t=70^\circ$), both resulting in inwards radial transport.

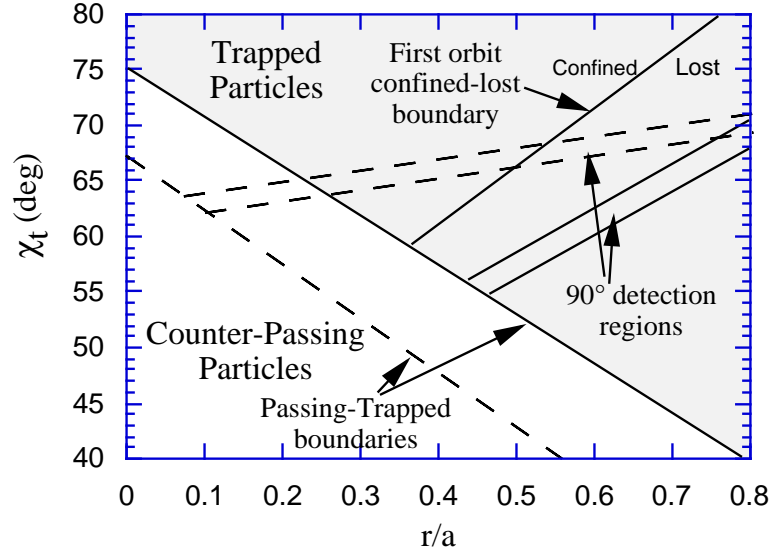


Figure 4.21: *Distribution of the different orbit classes for $R=2.45$ m, $I_p=1.8$ MA plasma in toroidal pitch angle versus their outer midplane crossing point for counter-going particles. Solid boundaries are for fully stripped 3.5 MeV α -particles. Dashed boundaries are for singly ionized 2.5 MeV α -particles representative of the anomalous loss.*

of counter-going particles in a 1.8 MA plasma. Both of these quantities are nearly conserved during an electron capture of the type shown in Fig. 4.19. The solid lines designate the boundaries for fully stripped 3.5 MeV α -particles. The passing/trapped boundary separates counter-passing orbits, which occur at low pitch angle or low minor radius, from trapped orbits (shaded region). The first orbit confined/lost boundary separates trapped confined orbits, which occur in the trapped region at high pitch angle or low minor radius, from trapped lost orbits. Within the region of trapped lost orbits is a subset of orbits, labeled as the 90° detection region, that intersect the detector at 90° below the midplane. The dashed lines designate the boundaries for singly ionized 2.5 MeV α -particles. All of the trapped 2.5 MeV singly ionized α -particles in this plot are lost in one poloidal orbit, thus there is no First Orbit Confined-Lost boundary for these particles. The region of 2.5 MeV singly ionized α -particles that intersect the vessel at 90° below the midplane are seen to correspond to previously first orbit confined (i.e. counter-passing and trapped confined orbits) 3.5 MeV fully stripped alphas all the way out to $r/a \approx 0.5$, within which over 90% of the alphas are born for a standard alpha source distribution (i.e. parabolic to the

eighth power). Therefore, nearly all of the 2.5 MeV singly ionized α -particle orbits that strike the 90° detector were previously confined.

An examination of α -particle orbits for a 1.0 MA plasma (producing a figure analogous to Fig. 4.21) has shown that all of the 2.5 MeV singly ionized α -particles that intersect the vessel at 90° below the midplane correspond to previously first orbit lost 3.5 MeV fully stripped α -particles. Therefore, there is no reservoir of confined α -particles at 1.0 MA available to take part in this loss mechanism, possibly explaining the absence of the anomalous loss at 1.0 MA.

Total fluence

The total fluence from this loss mechanism is estimated by modeling it as a new source of α -particles at a birth energy of 2.5 MeV, carrying a single charge, with an isotropic velocity distribution and the same radial source profile as the 3.5 MeV birth energy α -particles, allowing the use of the Lorentz ORBIT code. The predicted fluence of 2.5 MeV charge exchanged α -particles (i.e. He^+) to the 75° port of exposure B is a factor of 2 larger than the first orbit loss prediction under these assumptions. This falls short of the ratio of measured anomalous loss to predicted first orbit loss of 6 by a factor of 3. However, a flattening of the radial source profile from parabolic to the eighth to pure parabolic is sufficient to account for the full factor of 6. Flattening of the profile might be expected due to the peaking of the C^{+5} density profile on the edge of the plasma, making charge exchange more likely to occur there. Also, the assumption of an isotropic velocity distribution may affect the calculation.

A similar calculation (also assuming a new source of isotropic 2.5 MeV He^+ with the same source profile as the 3.5 MeV He^{++}) using the gc-ORBIT code (Sec. 4.5.2) to predict the global first orbit loss (rather than to a particular detector) in exposure B, yields 22.2% global loss, a factor of ~ 8 larger than the 2.7% predicted for first orbit loss of 3.5 MeV α -particles. And the loss to a poloidally localized region of the wall about 90° where the detector is located is ~ 6 times larger for 2.5 MeV He^+ than for 3.5 MeV He^{++} . The factor of 3 difference between the Lorentz ORBIT and gc-ORBIT predictions at 90° is probably due to the different projections that the

singly and doubly charged alpha orbits that are collected by the detector would make on the wall. This implies that the 2.5 MeV He^+ orbits collected by the detector would project onto an area of the wall ~ 3 times smaller than the 3.5 MeV He^{++} , owing to the fact that the larger downward drift of the 2.5 MeV He^+ causes them to strike the wall at angles closer to normal incidence thus creating a smaller projection. While these are just rough estimates of charge exchange loss, they do indicate that this mechanism might be capable of generating losses on the order of magnitude of the observed anomalous loss.

To get a more realistic estimate of the total loss it will be necessary to develop or modify a guiding center following code to include charge exchange and reionization as a function of α -particle energy during the slowing down process. This code would also need to take into account the radial dependence of the charge exchange and reionization probabilities since charge exchange is more likely to occur at the edge where the C^{+5} density profile is peaked, and reionization is more likely to occur in the core where the plasma density profile is peaked.

Pitch angle distributions

The pitch angle distributions for first orbit loss of 3.5 MeV He^{++} and charge exchange loss of 2.5 MeV He^+ calculated by the Lorentz ORBIT code as described above are shown in Fig. 4.22. The peak of the 2.5 MeV He^+ distribution occurs $\sim 6^\circ$ higher in toroidal pitch angle than it does for the first orbit loss of 3.5 MeV He^{++} . This is consistent with the inference that the anomalous loss peaks at a pitch angle $\sim 7^\circ \pm 7^\circ$ above the passing-trapped boundary for first orbit loss (Sec. 4.3.3). It is not clear that the shape of the pitch angle distribution for charge exchange loss would be the same as that calculated by treating it as a first orbit loss of 2.5 MeV He^+ , but the peak is likely to remain fixed at 62° since this corresponds to the passing-trapped boundary for 2.5 MeV He^+ in a 1.8 MA plasma.

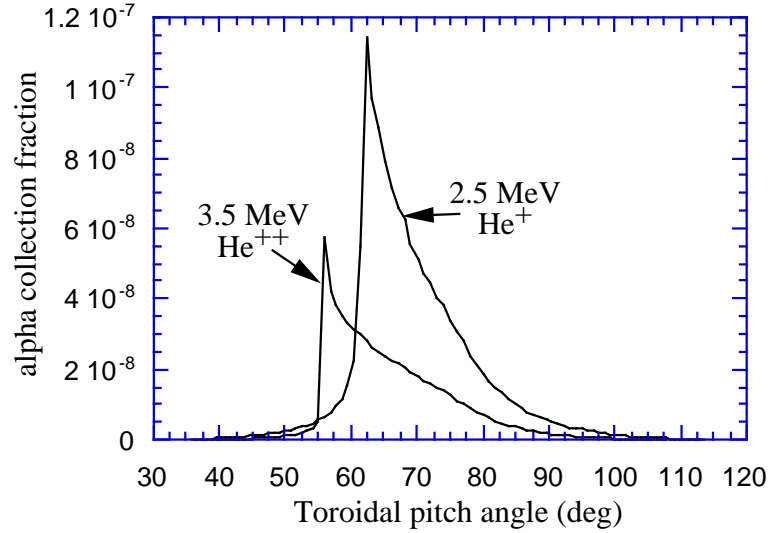


Figure 4.22: *Toroidal pitch angle distributions calculated at the detector for 3.5 MeV fully stripped α -particles and 2.5 MeV singly ionized α -particles in a $R=2.45$ m, $I_p=1.8$ MA plasma, assuming the same source profile and an isotropic velocity distribution in each case.*

Energy distribution

The energy distribution of charge exchange lost particles can be estimated by calculating the probability of charge exchange throughout the slowing down process. The probability for charge exchange at energy E , over a small period, Δt , such that E is fairly constant is:

$$P_{cx} = 1 - e^{-\Delta t/\tau_{cx}(E)} \quad (4.4)$$

where the collision period for charge exchange, τ_{cx} , is calculated as a function of energy as the α -particle slows down using Fig. 4.18. The time to slow down by 0.25 MeV increments is estimated from:

$$\frac{dE}{dt} = -\frac{E}{\tau_{sd}} \approx \frac{\Delta E}{\Delta t} \quad (4.5)$$

where τ_{sd} is the slowing down time (i.e. energy e-folding time) in the core. Reionization is neglected such that once an α -particle undergoes charge exchange it is assumed that it is no longer available to charge exchange at a lower energy. The resulting energy distribution is shown in Fig. 4.23 for three different slowing down

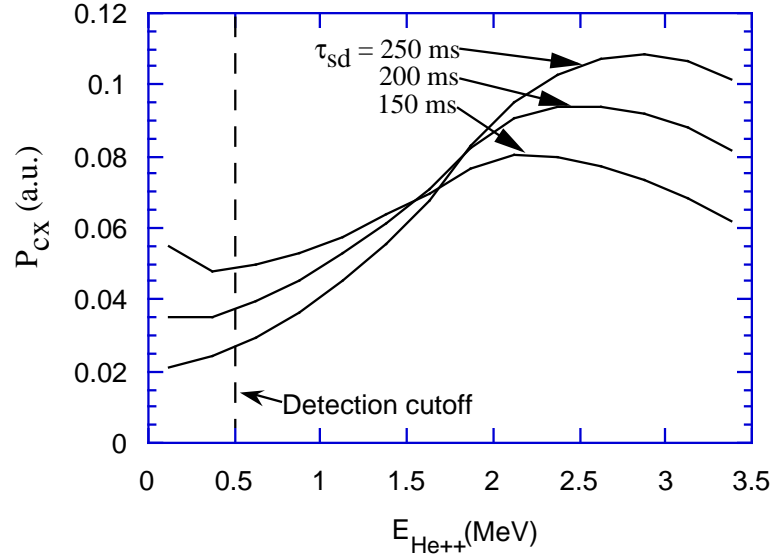


Figure 4.23: *Calculated probability of charge exchange versus α -particle energy. Assuming α -particles are lost only on their first charge exchange event, this plot represents the expected energy distribution of charge exchange lost α -particles.*

times. The inferred energy of the peak of the anomalous loss of 2.5 ± 0.3 MeV is seen to be consistent with $\tau_{sd} = 200 \pm 50$ ms. The higher anomalous loss energy inferred from exposure D (2.7 ± 0.3 MeV) as compared to exposure B (2.2 ± 0.3 MeV) (see Sec. 4.3.2) might be explained by the longer slowing down time of the hotter plasma in exposure D (Table 4.1). At a slowing down time of 200 ms, $\sim 90\%$ of α -particles are calculated to charge exchange before slowing down below the minimum detection energy of 0.5 MeV.

NBI neutrals

The other potential donors of electrons present in significant quantities are the NBI neutrals [52]. In this case, the velocity of the donor (i.e. the neutral beam species) must be taken into consideration since it is an appreciable fraction of the α -particle velocity. For instance, a 100 keV deuteron travels at about a third the speed of a 2.0 MeV α -particle. The cross section for charge exchange between a fully stripped 2.5 MeV α -particle and a neutral 100 keV deuteron reaches a maximum of $\sim 10^{-18}$ cm² when

they are traveling in the same direction, and a minimum of $\sim 10^{-21}$ cm² when they are traveling in opposite directions [53]. Using the maximum of 10^{-18} cm² to obtain a conservative estimate, and assuming a density of NBI neutrals of $\sim 10^9$ cm⁻³ and a beam volume to plasma volume ratio of ~ 0.01 to account for the beam localization results in a collision period of ~ 70 sec. Thus, this process is insignificant in comparison to impurity charge exchange and slowing down.

The delayed loss observed by the scintillator detectors in DD might be caused by a similar mechanism. Since the DD fusion products are only singly ionized, charge exchange results in neutralization and subsequent straight line trajectories. Reionization in the plasma might allow some of these fusion products to transition to prompt loss orbits [52]. The differing mechanisms might account for the detection of the anomalous loss only in DD plasmas for the scintillator detectors.

The preceding calculations based on the CTMC cross sections show that CX loss may be consistent with many of the anomalous loss features. However, this loss mechanism is not consistent with the radial distribution of the anomalous loss nor its absence on the 90° scintillator detector.

4.5.5 Loss during I_p Rampdown

As the plasma current is ramped down at the end of a plasma discharge, remaining high energy α -particles become deconfined as the downward ∇B and curvature drifts become dominant. However, the I_p ramp down in exposure B doesn't start until 500 ms after the end of NBI and since the energy e-folding time (τ_{sd}) due to electron drag remains < 200 ms, as shown in Fig. 4.24, in the plasma core during this time, the α -particle energy should have dropped by several factors of e by the start of the I_p ramp. Just two e-folding times are sufficient to reduce the α -particle energy below the detector's minimum detectable energy of 0.5 MeV. The observed peak in the energy distribution occurs at an energy only $\sim 30\%$ lower than 3.5 MeV and so, assuming there are no accelerating forces acting on the α -particles during the ramp down, cannot be attributed to anything that occurs > 100 ms after the end of NBI.

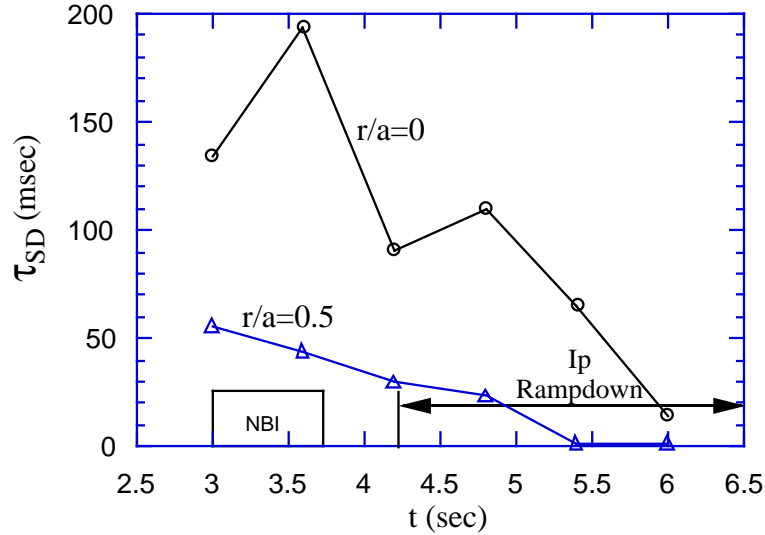


Figure 4.24: *Slowing down times calculated for $r/a=0$ and $r/a=0.5$ as a function of time in the discharge of exposure B.*

The induced toroidal electric field associated with the I_p ramp down can, however, cause a positive acceleration of counter-going passing α -particles. But this toroidal acceleration causes them to become more passing, which is not consistent with the detection of co-going particles. Furthermore, if there is a significant lower energy loss occurring after NBI, it should be visible to the lost alpha scintillator detectors, but it has never been observed. Therefore, a partially thermalized loss due to the current ramp down at the end of the discharge is not a viable explanation of the anomalous loss data.

It should be mentioned that the I_p ramp down in exposure D begins just 200 ms after the end of NBI, which was extended by 300 ms to increase the total alpha fluence to the collector probe. In Sec. 4.3.2 the peak in the alpha energy distribution was inferred to be $\sim 2.7 \pm 0.3$ MeV for exposure D. This is ~ 0.5 MeV higher than the peak of exposure B which had a 500 ms delay between the end of NBI and the beginning of the I_p ramp down. The higher anomalous loss energy associated with the shorter delay may be an indication that the anomalous loss mechanism does occur after the end of NBI, although, as mentioned above, this is highly unlikely. A scan of the delay time between NBI and the ramp start time could resolve this issue.

4.5.6 Scattering off RF Limiters and Collimator Walls

Scattering off of RF limiters and the wall of a collimating port can reduce the energy spectrum of the incoming α -particles. However, it is unlikely that scattering could explain the anomalously large alpha fluence observed in the 1.8 MA plasmas since this is not a new source of α -particles. It is also unlikely that there will be a significant contribution of scattered α -particles in the foil samples since large angle deflections of α -particles are quite rare in solids. TRIM-95 simulations (Sec. 4.2.2) of 3.5 MeV α -particles implanting into carbon at shallow angles result in just 20% of the implanted α -particles reemerging from the face of a flat piece of carbon when implanted at an angle of incidence of 89° (1° grazing angle), and less than 1% at 85° . In other words, most of the α -particles that enter a limiter or the wall of a collimating port will be stopped (within $\sim 11\mu\text{m}$) without reemerging. Bench top implants using aluminum collimators with ^{241}Am alpha sources were done for calibration purposes. Results showed reasonable agreement to the predicted fluence and range distribution (Sec. 3.4.2). Furthermore, it is unlikely that the plasma current dependence could be explained by scattering.

4.5.7 Activation of Surrounding Materials

Activation of materials in first wall components by absorption of 14 MeV fusion neutrons and the subsequent release of α -particles through (n,α) reactions is very unlikely as a possible explanation of the anomalous loss. The largest cross sections for (n,α) reactions from 14 MeV neutrons are on the order of 10^{-25} cm^2 [54]. Using this conservatively large cross section (even though it is unrealistic for the materials in the first wall) results in a mean free path for a 14 MeV neutron of $\sim 100\text{ cm}$ in solid density. Assuming the resulting α -particles can escape from within $10\mu\text{m}$ of the surface, the neutron fluence of $\sim 10^{11}\text{ neutrons/cm}^2$ yields $\sim 10^6\text{ alphas/cm}^2$, or about six orders of magnitude smaller than the levels detected by the alpha collector. Therefore, (n,α) reactions can not provide the flux levels needed to explain the anomalous loss.

The fact that most of the (n,α) reactions have half lives $>10\text{ sec}$ [54] could allow

the collector probe to integrate the alpha collection over an extended duration even after the shot is over, possibly explaining the absence of the anomalous loss on the real time scintillator detectors. However, it would be difficult to explain the pitch angle distribution and plasma current dependence of the anomalous loss with such a mechanism.

4.5.8 Foil Surface Fusion

Another possibility that must be considered is that NBI D & T ions at 100 keV may be striking the surface of the foil and the walls of the collimating ports and fusing with D & T that are on the surface. This would give rise to an alpha source with a nearly isotropic velocity distribution near the surface of the foils. These α -particles wouldn't have to undergo any collimation so could implant at large incident angles (0° being normal to the surface) explaining the shallow depth distribution. However, the deeper collimating ports of the redesigned probe head were intended to exclude NBI ions while allowing α -particles, which have $\sim 3\times$ larger gyroradius, to still implant (Sec. 4.3). It can be inferred from the fact that the anomalous loss features remained essentially unchanged between the two designs that foil surface fusion was not significant. This mechanism can also be ruled out on the basis of the current dependence. As I_p increases, the confinement of NBI ions should increase, providing less of a source of fusion on the foil surface.

4.5.9 Diffusion of Residual He

Residual He in the tokamak, leftover from previous experiments or from alpha ash, will not reach MeV energies during a discharge with no RF. The first Ni foil layer should stop α -particles below 0.5 MeV. If the foils are heated sufficiently to allow diffusion of this He into the deeper foil layers there should be a monotonic decrease in the alpha fluence with layer depth from a peak in the shallowest layer. Thus diffusion of residual He can not account for the peaks in the fourth and fifth layers of the 1.8 MA exposures.

Furthermore, it is unlikely that the current dependence of the anomalous loss could be explained by diffusion of residual He since the improved confinement associated with the higher plasma current should reduce heating of collector foils. Diffusion of residual He may, however, explain the low energy anomalous loss observed in 1.0 MA discharges.

4.5.10 Diffusion of Implanted He

The diffusion of implanted He from layer to layer between the time of implantation and removing the foils from the spool piece cannot explain the anomalously large fluence associated with the 1.8 MA data. Furthermore, if implanted He does diffuse, it should diffuse in both directions and not just toward the shallower layers as implied by the 1.8 MA data.

4.6 Summary, Conclusions, and Suggestions for Future Work

See Sec. 6.2 of the Conclusions Chapter for a summary, conclusions, and suggestions for future work.

Chapter 5

Major Radius Shift Experiment

5.1 Introduction

At first sight, it seems reasonable that as a confined marginally passing α -particle trajectory, such as that shown in Fig. 5.1, moves toward higher magnetic field during an inward major radius shift that the α -particle would mirror and become a trapped particle (shown in Fig. 5.1 by the lighter shade) leading to increased α -particle loss. Increased alpha loss observed using the lost alpha scintillator detectors during previous major radius shifts conducted on TFTR, usually for cross calibration of multi-chord diagnostics, have raised the question whether this alpha loss is induced by the shift itself or by the MHD that is often generated during such shifts. To answer this question, a systematic study of alpha loss during major radius shifts in MHD quiescent plasmas was conducted using the lost alpha scintillator detectors. The alpha collector of Chapters 3 and 4 was not used during this experiment because of the use of large major radius plasmas ($R=2.62$ m) in which the alpha collector would extend inside the last closed flux surface and overheat. Furthermore, the poor time resolution of the alpha collector makes it unsuited to making observations of a transient nature (e.g. R shifts).

A shift-induced deconfinement of previously confined, marginally passing α -particles to the lost alpha scintillator detectors would make it possible to study the physics of charged particles near the passing/trapped boundary in phase space. In particular, it might be possible to experimentally verify the existence of collisional nonprompt alpha loss (Sec. 2.4.1) [15], which, under steady state conditions, is thought to contribute an insignificant amount (i.e. $< 10\%$) to the total fusion product loss. Fig. 5.2(a) depicts velocity phase space for a fixed r/a outer midplane crossing point of counter-going particles. As α -particles slow down from $v/v_0 = 1$, where v_0 is the birth velocity, they also undergo pitch angle scattering which alters their v_{\perp}/v . This results in the scattering of marginally passing α -particles across the passing/trapped boundary as they slow down, causing these particles to be nonpromptly lost. The passing/trapped boundary moves to higher v_{\perp}/v at lower v/v_0 due to the improved confinement associated with the narrower banana width at lower energy. Below a certain energy the trapped particles are also confined and no longer contribute to collisional nonprompt

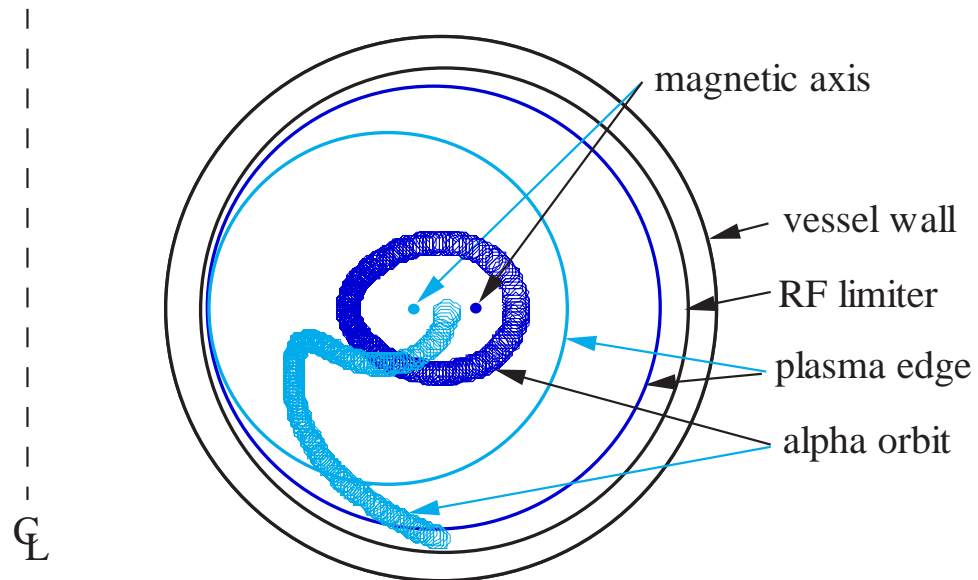


Figure 5.1: *Inward major radius shift of plasma from 2.6 m to 2.4 m (2.4 m features drawn in light shade) causing a marginally passing α -particle orbit to transition to a trapped orbit lost to the 90° detector, assuming no energy is gained by the α -particle during the compression.*

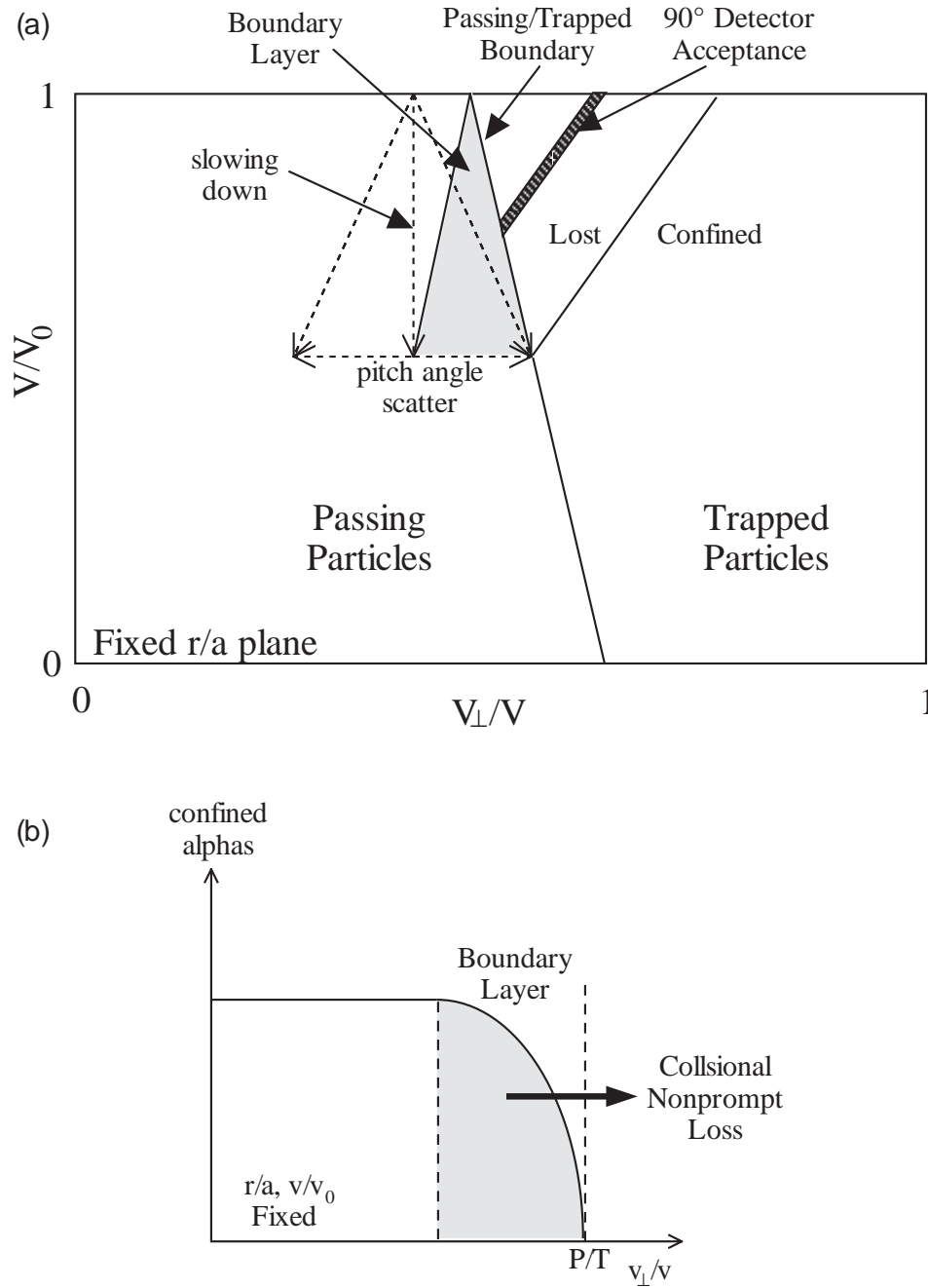


Figure 5.2: (a) Velocity space depicting slowing down and pitch angle scattering of alphas. Marginally confined passing particles scattering across the passing/trapped boundary create a partially depleted boundary layer as depicted in (b) for fixed r/a and v/v_0 .

loss. The phase space region in which α -particles intercept the 90° detector is also depicted. As shown in Fig. 5.2(b) for a given energy and r/a , this collisional loss process establishes a partially depleted boundary layer near the passing/trapped boundary in which the α -particle distribution function decays to zero at the boundary. The slope of this distribution function should lead to a diffusive flux of particles across the boundary. If an inward major radius shift can cause a shift of the passing/trapped boundary toward the passing region in phase space, however, this loss mechanism can be transiently enhanced by moving the boundary into an undepleted region in phase space.

The inward major radius shift is an adiabatic compression, generated by increasing the vertical magnetic field on a time scale that is slow compared to the thermal particle collision time, but fast compared to the energy confinement time [55]. The toroidal magnetic field is held constant during the shift such that $a \sim R^{1/2}$ to conserve toroidal magnetic flux. At the same time, the plasma current is increased as $I_p \sim R^{-1}$ to maintain the q profile constant. These scalings are modified by the fact that the plasma is continually limited by the bumper limiter at R_{bl} on the high field side. This causes the outer edge of the plasma to be scraped off, since the minor radius is constrained by this limiter to $a = R_0 - R_{bl}$, which decreases faster than $a \sim R^{1/2}$.

During adiabatic compression, the magnetic moment and canonical angular momentum of an α -particle should be conserved. These quantities comprise two of the three constants of the motion needed to fully characterize the guiding-center motion of a charged particle in an axisymmetric tokamak. The third quantity needed to complete the orbit description is the particle's energy. Thus, a determination of the energy gained from compression is required. This energy change can be found by averaging the velocity change along the trajectory of the particle in time [56], and is found to increase in roughly the same proportion as the decrease in plasma major radius for marginally passing α -particles. Somewhat surprisingly, this energy gain is found to be sufficient to allow most marginally passing α -particles to remain passing throughout the major radius shifts such that little or no shift-induced alpha loss is expected.

However, an unexpected loss of partially thermalized alphas lost at the passing/trapped boundary in phase space was observed in this experiment. This anomalous loss occurs at a plasma current of 1.4 MA, but not at 1.0 nor 1.8 MA. It occurs ~ 80 ms after an inward major radius shift from 2.6 to 2.4 m, and persists until the major radius is shifted back out to 2.6 m. Collisional loss and MHD are considered as possible explanations, but neither are consistent with this anomalous loss.

5.2 Experiment

5.2.1 Experimental Design and Initial Expectations

Major radius shifts in TFTR DT discharges were done at three values of plasma current; 1.0, 1.4, and 1.8 MA. All were done at 10 MW of NBI power, low enough to avoid significant MHD activity, but high enough to provide sufficient lost alpha signal. The NBI phase lasted for 1.5 s, as shown in Fig. 5.3(a). The plasma was first allowed to equilibrate for 700 ms after the onset of NBI. The major radius was then shifted inward, as shown in Fig. 5.3(b), from 2.6 m to R' in 80 ms, where R' was 2.4 m for the 1.0 and 1.4 MA discharges, and 2.5 m for the 1.8 MA discharge. The higher current case was more severely limited in shift range by the potential for disruption caused by the edge q passing through a low rational value. The major radius is then shifted back out to 2.6 m, also in 80 ms, starting 320 ms after the end of the first shift. Baseline discharges at 2.6 m and R' were also done at each plasma current for comparison. The TFTR shot numbers for the shifted and baseline (BL) discharges are listed in Table 5.1, along with R' and the value the plasma current was shifted to (I'_p) in conjunction with the major radius shift to R' . Each shifted shot was repeated to ensure reproducibility. The backup shot numbers (and corresponding parameters if different from primary shot) are shown in parenthesis. The results presented in the remainder of this chapter are only from the primary shots, but a comparison with the backup shots does show consistency.

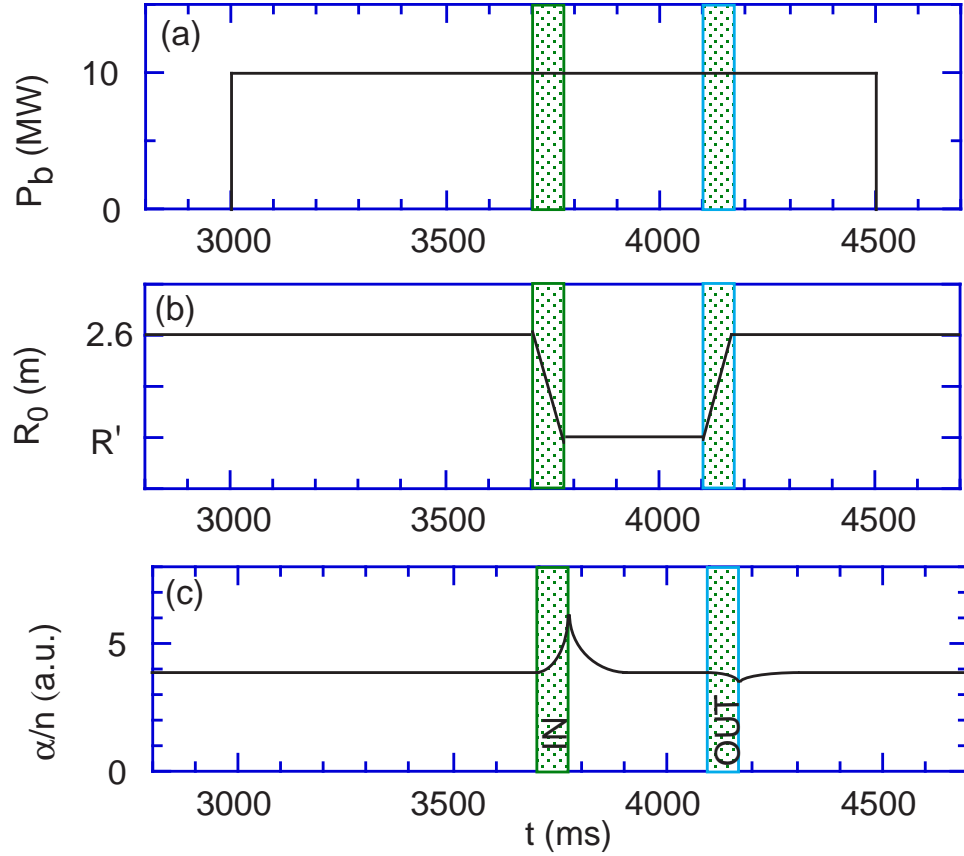


Figure 5.3: Waveforms for (a) the NBI power, (b) the major radius, and (c) schematic representation of the expected lost- α signal to the 90° detector.

The expectation that there would be an increased alpha loss during the IN shift is shown schematically in Fig. 5.3(c). The gradual decay of the peak in the alpha signal was expected with the transient effect of having a more fully populated boundary layer region near the passing/trapped boundary, producing increased collisional non-prompt loss [15] for the length of time it takes to reestablish an equilibrium [57, 58]. It was also expected that an increased alpha loss signal would be accompanied by a widening of the gyroradius distribution and a decrease in the mean gyroradius, since the additional loss would be comprised of α -particles that have been confined long enough to slow down to some degree, and not just birth energy α -particles. Also, because the additional loss should occur at the passing/trapped boundary, the increased loss signal would be accompanied by a narrowing of the pitch angle distribution, since

I_p (MA)	1.0	1.4	1.8
R' (m)	2.4 (2.35)	2.4	2.5
I_p' (MA)	1.1 (1.1)	1.5	1.9
Shifted Shot #	86139 (86171)	86136 (86134)	86144 (86143)
BL Shot # ($R_0=2.6$ m)	86169	86168	86176
BL Shot # ($R_0=R'$, $I_p=I_p'$)	86167	86166	86175

Table 5.1: *R Shift Shot List*

the additional loss would be more localized in pitch angle than first orbit loss, and a decrease in the mean pitch angle, since the passing/trapped boundary occurs below the mean of the first orbit loss pitch angle distribution.

Little effect was expected during the OUT shift since the passing/trapped boundary was expected to shift in phase space toward a region of trapped particles which had been previously lost on their first orbit (since passing particles are expected to become more passing as the plasma moves to lower magnetic field). A small reduction in the lost alpha signal was, however, expected due to the reduced collisional nonprompt loss associated with the more fully depleted boundary layer region that would be established as a result of the OUT shift.

5.2.2 Experimental Results

Total Alpha flux

Fig. 5.4 shows the neutron normalized 90° lost alpha detector signals as a function of time at the three values of plasma current: (a) 1.0 MA; (b) 1.4 MA; and (c) 1.8 MA. The circle and x symbols correspond to the alpha collection fractions (alphas detected/alphas produced) calculated for first orbit loss by the Lorentz ORBIT code using the alpha source and q radial profiles from TRANSP. The 1.4 MA R shifted

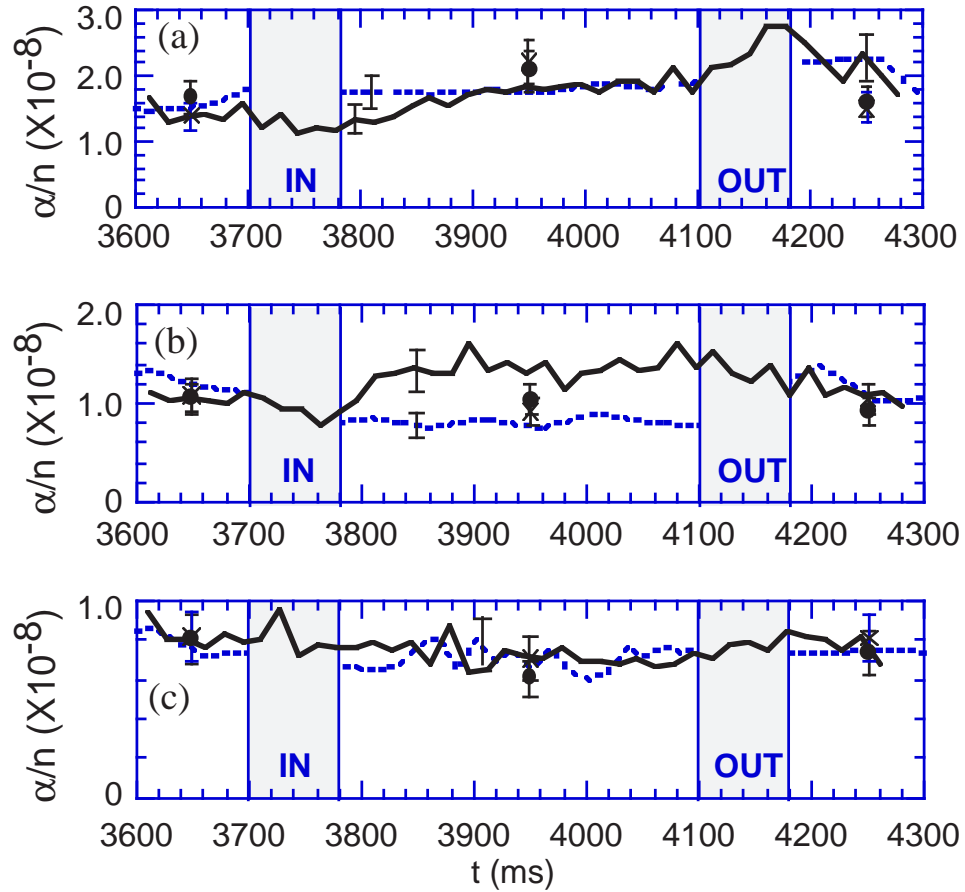


Figure 5.4: 90° lost alpha detector signals for (a) 1.0 MA, (b) 1.4 MA, and (c) 1.8 MA major radius shifts. Solid traces are for the shifted discharges while the dashed traces are for baseline discharges for comparison. Circle and x symbols correspond to the alpha collection fractions calculated for first orbit loss. Error bars of $\pm 15\%$ are based on detector uncertainty.

signal in Fig. 5.4(b) is normalized to the calculated first orbit alpha collection fraction at 3.65 s. The relative strengths of the remaining signals are preserved such that no further normalizations are needed. For comparison, the signals from two separate baseline discharges at each current, one at 2.6 m (shown before IN and after OUT) and one at R' (shown between IN and OUT), are shown in dashed lines. The lost alpha signals of the baseline discharges should be comprised predominantly of first orbit loss. With the possible exception of the 1.0 MA discharge in Fig. 5.4(a), there does not appear to be any appreciable change in the alpha signal during the IN shift. The 1.0 MA discharge may be exhibiting a slight decrease in normalized alpha loss during the IN shift, opposite to the expected effect, but the magnitude of this drop is within the uncertainty of the detection method. Similarly, there does not appear to be any significant change during the OUT shift. The most pronounced effect occurs in the 1.4 MA discharge, shown in Fig. 5.4(b), between the IN and OUT shift. Here the shifted discharge displays alpha loss approximately 70% higher than the baseline shot. The first orbit model points for the shifted and baseline shots at 3.95 s, however, do not exhibit this effect. The increased loss takes about 80 ms to build up after the end of the IN shift. This result was unexpected.

Gyroradius Distribution

The 2D images of the scintillator detector are interpreted in terms of gyroradius and pitch angle as discussed in Sec. 2.5.1. Gyroradius distributions are obtained by averaging over a range of pitch angles and vice versa for pitch angle distributions. Fig. 5.5 shows the mean value of the gyroradius distribution (averaged over the full pitch angle range of 40 to 90°) as a function of time for the signals in Fig. 5.4. The mean gyroradii of the shifted discharges agree with that of the baseline shots, within the detector uncertainty, with the exception of the time interval between the IN and OUT shift in the 1.4 MA discharge shown in Fig. 5.5(b). This correlates with the anomalously large signal seen in Fig. 5.4(b). Assuming an anomalous loss flux that is 70% that of first orbit loss, as inferred from Fig. 5.4(b), the decrease in mean gyroradius seen in Fig. 5.5(b) corresponds to an anomalous loss energy of $E_{anom} \approx (0.8 \pm 0.1)E_0$. For the the 1.0 MA discharge shown in Fig. 5.4(a), where

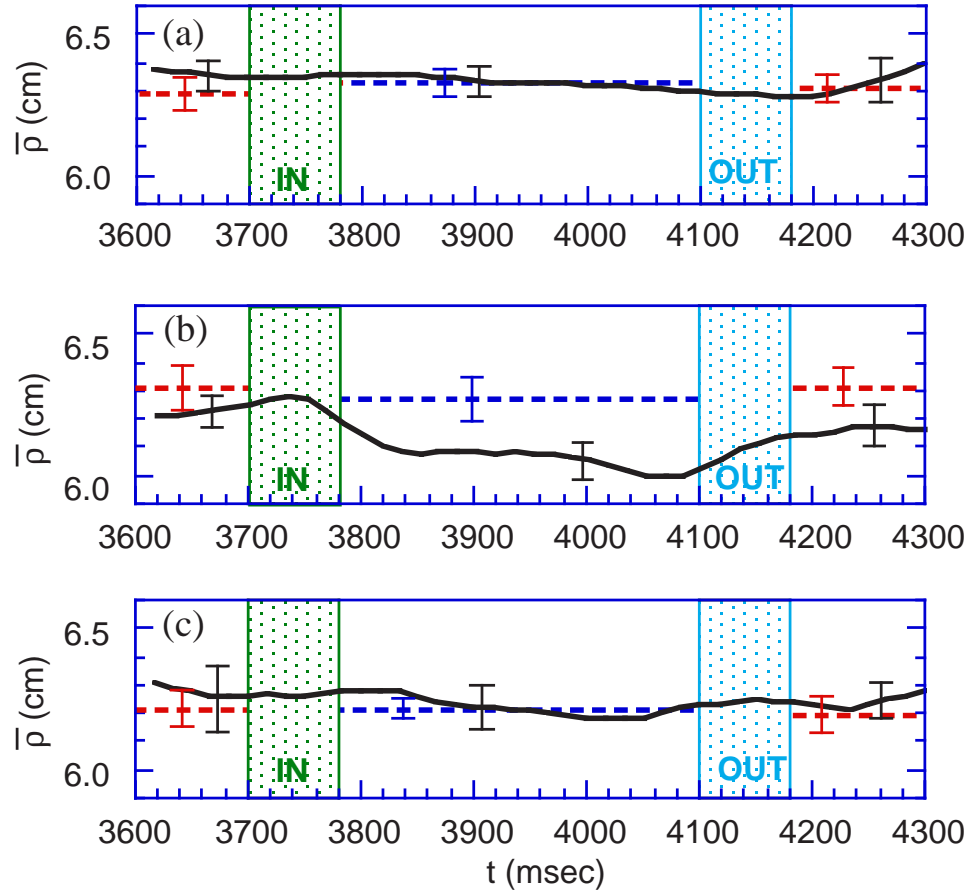


Figure 5.5: Mean of the gyroradius distribution as a function of time for the 90° lost alpha detector signals shown in Fig. 5.4. Error bars based on one standard deviation in data scatter.

it was not clear if there was an anomalous loss feature, there does not appear to be any significant deviation from the baseline mean gyroradius during the IN and OUT shifts, making it consistent with first orbit loss at 3.5 MeV.

Pitch Angle Distribution

Fig. 5.6 shows the mean value of the pitch angle distribution as a function of time for the signals in Fig. 5.4. The mean pitch angles of the shifted discharges agree with that of the baseline shots for each of the plasma currents, within the detector uncertainty,

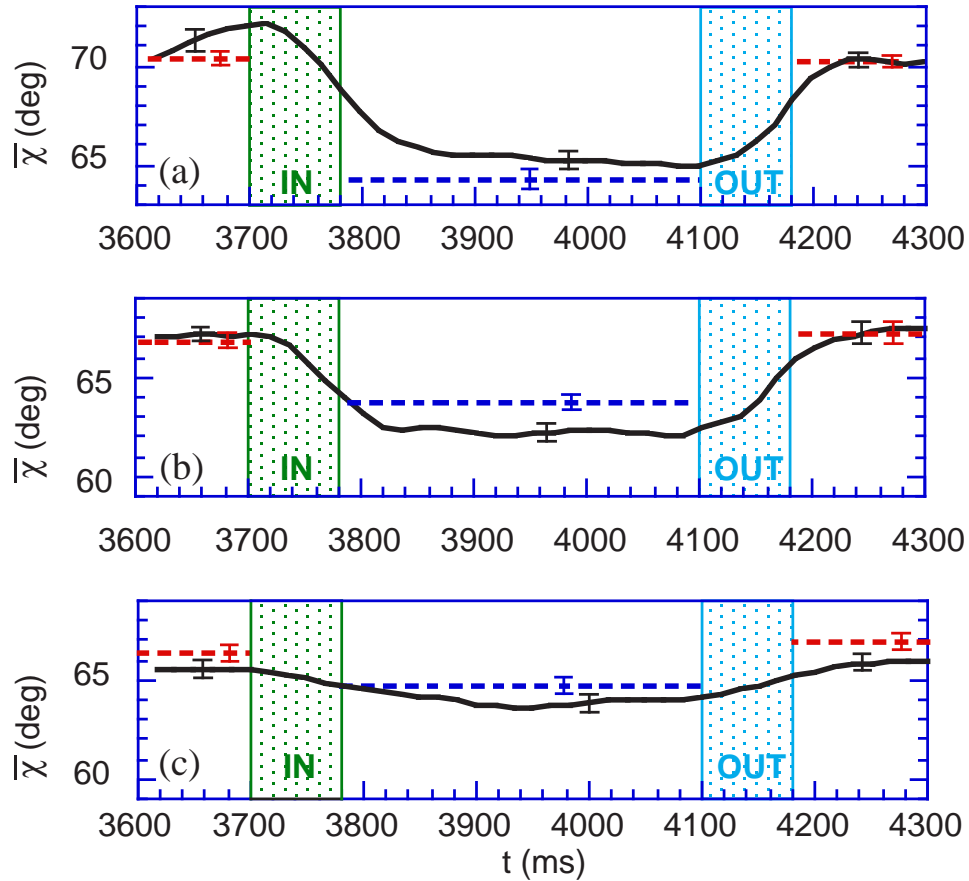


Figure 5.6: Mean of the pitch angle distribution as a function of time for the 90° lost alpha detector signals shown in Fig. 5.4. Error bars based on one standard deviation in data scatter.

with the exception, of the time interval between the IN and OUT shift in the 1.4 MA discharge shown in Fig. 5.6(b). Again, this correlates to the anomalous signal seen in Fig. 5.4(b).

Fig. 5.7 shows the actual pitch angle distribution for the 1.4 MA shifted discharge and its baseline comparison shot, integrated over the time of the anomalous loss between the shifts (3.9 to 4.1 s). The dashed curve labeled (a) is the baseline distribution renormalized to the peak of the shifted distribution to show that the shifted distribution is significantly narrower than that of the baseline distribution and is concentrated near the passing/trapped boundary at 59° (labeled P/T). The dashed curve labeled (b) is the sum of the baseline distribution and a modeled loss at the passing/trapped

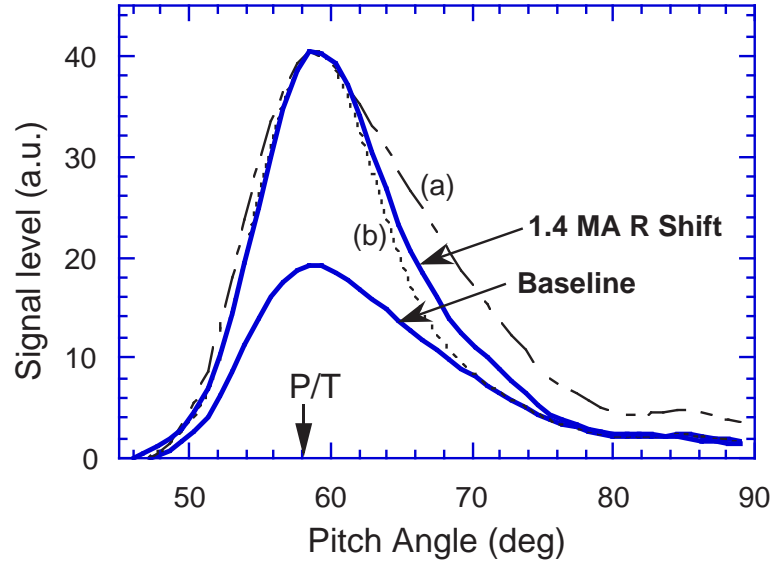


Figure 5.7: Pitch angle distribution for period of time during anomalous loss (3.8–4.1 s). Solid lines correspond to baseline and shifted discharges. Distribution (a) is the baseline distribution renormalized to the shifted distribution for shape comparison. Distribution (b) is the sum of the baseline distribution and a distribution of α -particles lost at the passing/trapped boundary (labeled P/T) corrected for detector response.

boundary, which takes into account the geometrical and optical resolutions of the detector. The close agreement between curve (b) and the shifted distribution is a good indication that the anomalous loss is peaked at the passing/trapped boundary, possibly extending up to $\sim 5^\circ$ above this boundary. The pitch angle distributions for the discharges at the other currents, and for the 1.4 MA discharge before and after the shifts, display reasonably good agreement with their baseline shots, consistent with pure first orbit loss. This is true with the possible exception of the 1.8 MA discharge, which appears to exhibit behavior similar to the 1.4 MA discharge during the period between the shifts, but in a much less pronounced fashion.

5.3 Discussion

From Figs. 5.4–5.6 it is inferred that there are no additional alpha losses, besides the first orbit loss, occurring during the times of the IN and OUT shifts at the three values of plasma current. There does, however, appear to be an anomalous loss of partially thermalized α -particles at the passing/trapped boundary occurring between the time of the IN and OUT shifts at 1.4 MA.

Section 5.3.1 will offer an explanation for the absence of the expected effect of the shifts on alpha loss. Then some possible explanations for the 1.4 MA anomalous loss feature will be considered in Section 5.3.2.

5.3.1 Shift Induced Loss

Induced Toroidal Electric Field

Ref. [56] considers the effect that adiabatic compression has on α -particle orbits. The shift of the poloidal flux to smaller major radius induces a toroidal electric field which reverses direction from the high field to the low field side of the plasma. This toroidal electric field is given by:

$$E_\phi = (\partial\Psi/\partial t)_a/2\pi Rc \quad (5.1)$$

where Ψ is the poloidal flux and the partial derivative $(\partial\Psi/\partial t)_a$ is taken in a reference frame at rest with respect to the vessel. This toroidal electric field produces an $\mathbf{E} \times \mathbf{B}$ drift that pulls the α -particles inward in major radius along with the plasma while accelerating them to higher energy. It can be shown that all α -particles gain energy regardless of their orbit classification [56]. This results from the fact that the drift surface of a co-going orbit is shifted outward in major radius (Fig. 2.1), causing the particle to spend more time being accelerated by the induced toroidal electric field on the outboard side of the plasma than being decelerated by the reversed electric field direction on the inboard side. Conversely, the drift surface of a counter-going orbit

is shifted inward, causing the particle to spend more time being accelerated on the inboard side than being decelerated on the outboard side. A trapped particle orbit achieves net energy gain because the acceleration during the co-going leg is sufficient to overcome any deceleration that might be experienced due to an incomplete transit on the inboard side of the plasma during the counter-going leg. In general, $\langle E_\phi v_\parallel \rangle > 0$ (where $\langle \dots \rangle$ denotes average along a particle trajectory in time) and passing particles gain more energy than trapped particles because they travel farther along the accelerating field.

Energy Gain and Shift Induced Loss

We begin with a heuristic argument to explain the lack of induced alpha loss during the IN shift. The velocity gained by marginally passing α -particles can be estimated from an approximate description of compression discussed in Ref. [56] where:

$$\frac{dv}{dt} \simeq \frac{v}{R_{ma}} \left| \frac{dR_{ma}}{dt} \right| \left[\frac{1}{2} + \frac{v_\parallel^2}{2v^2} \right] \quad (5.2)$$

where R_{ma} is the major radius of the magnetic axis. Solving for the fractional change in α -particle energy we find:

$$\frac{\Delta E}{E} = \frac{2\Delta v}{v} \simeq -\frac{\Delta R_{ma}}{R_{ma}} \left[1 + \frac{\langle E_\parallel \rangle}{E} \right] \quad (5.3)$$

where $\langle E_\parallel \rangle$ is an α -particle's parallel energy along the magnetic field averaged over the particle's orbit. For a marginally passing α -particle, which spends a large majority of its orbit bounce time near the inner midplane where its parallel velocity tends to zero, the $\langle E_\parallel \rangle$ term in Eq. 5.3 is negligible. Thus the fractional energy gain of a marginally passing α -particle is approximated by the fractional decrease in the major radius.

The change in the maximum toroidal magnetic field that an α -particle orbit reaches is related to the change in its minimum major radius by:

$$\frac{\Delta B_{max}}{B_{max}} = -\frac{\Delta R_{min}}{R_{min}} \quad (5.4)$$

Thus, assuming for the moment that an α -particle orbit shifts along with the plasma so that $\Delta R_{min}/R_{min} \simeq \Delta R_{ma}/R_{ma}$, then from Eqs. 5.3 and 5.4 we find that $E'/E \simeq B'_{max}/B_{max}$, where the prime denotes after the IN shift. Using the conservation of magnetic moment, $\mu = E_{\perp}/B = E(1 - \lambda^2)/B$, where the pitch variable $\lambda \equiv v_{\parallel}/v = \cos \chi$, we find that for a marginally passing particle ($\lambda_{min} \simeq 0$):

$$\frac{\mu'}{\mu} = 1 = \frac{E'(1 - \lambda'^2_{min})/B'_{max}}{E(1 - \lambda^2_{min})/B_{max}} \simeq \frac{(1 - \lambda'^2_{min})}{(1 - \lambda^2_{min})} \quad (5.5)$$

From Eq. 5.5 we find that $\lambda'_{min} \simeq \lambda_{min}$, so that a marginally passing α -particle remains marginally passing, and therefore there is no alpha loss induced by the shift. But we have not given any evidence to support the assumption that an α -particle orbit moves the same amount as the plasma during the shift. Determining the new R_{min} of an α -particle orbit as a result of the R shift would require a complex equation of motion calculation taking into account the changing magnetic equilibria throughout the shift. A simpler method that avoids the need to track the entire shift is to consider the constants of the motion before and after the shift. The (μ, P_{ϕ}) space presented in Sec. 2.2.2 will be used.

Major Radius Shift in (μ, P_{ϕ}) Space

The boundaries designating orbit classifications in (μ, P_{ϕ}) space, shown in Fig. 2.2(b), shift in response to changes in plasma conditions, such as major radius and α -particle energy. However, in the absence of collisions, μ and P_{ϕ} of an individual α -particle remain fixed. Thus, by calculating the population of α -particles swept out by the shifting boundaries, the expected effect on the lost alpha signal can be estimated.

First, we consider the case of zero energy gain by an α -particle. Fig. 5.8(a) zooms in on a region of the (μ, P_{ϕ}) space for 3.5 MeV α -particles in the 1.4 MA discharge. The fixed (R,Z) parabola corresponding to the location of the 90° detector is also included. The boundaries after the IN shift are shown in lighter shading. The shifts of the boundaries, assuming no α -particle energy gain, are clearly evident. The portion of the 90° detector curve from the passing/trapped boundary to the LCFS $v_{\parallel} = 0$ line corresponds to first orbit loss of trapped α -particles (represented by the curve

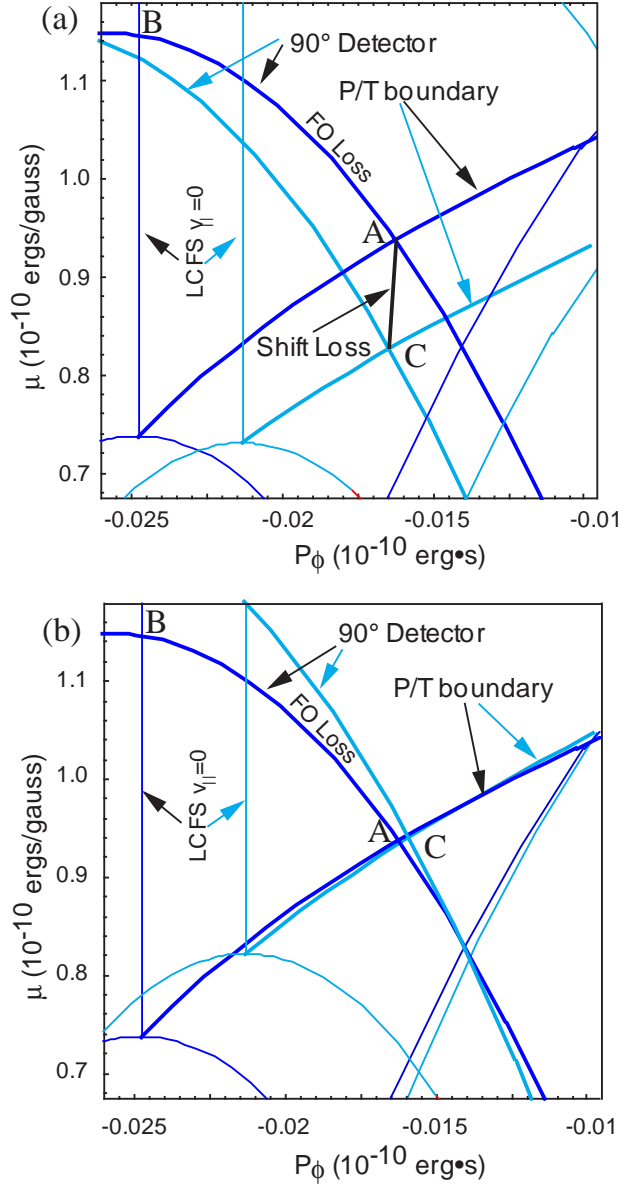


Figure 5.8: Region of (μ, P_ϕ) space showing boundaries before (3.6 s) and after (3.9 s) the IN shift for the 1.4 MA discharge (after IN shift designated by light shading), assuming (a) zero energy gain and (b) 12% energy gain by α -particles. First orbit loss is characterized by the portion of the 90° detector parabola between the passing/trapped boundary and the $v_{||} = 0$ along the LCFS (i.e. trace AB). Shift induced loss is characterized by the line connecting the intersections of the 90° detector parabola and the passing/trapped boundary before and after the IN shift (i.e. line AC). The energy gain of 12% shown in (b) is the gain needed to eliminate shift induced loss.

AB before the shift). The intersection of the P/T boundary and the 90° detector curve represents where previously confined counter-going α -particles transition to trapped α -particles lost to 90° detector as the P/T boundary sweeps across their (μ, P_ϕ) . The line AC then represents the α -particles near 3.5 MeV that contribute to any 90° detector signal increase induced by the IN shift. Alphas below the 3.5 MeV birth energy can also be lost by this mechanism. Thus, the population of α -particles that will be lost due to the shift builds up prior to the shift. The build up period is determined by the time it takes to slow down to a critical energy, below which the α -particles' banana width is too narrow to reach the 90° detector. For the 1.4 MA case in Fig. 5.8(a), the critical energy at $(r/a) = 0.3$ (within which radius over 50% of the α -particles are born) is $\approx 0.8E_0$. With an energy e-folding time of ~ 225 ms, it only takes ~ 50 ms to slow down to this energy. Thus, the α -particles lost by the shift accumulate on roughly the same time scale as they are released by the 80 ms shift.

As a rough estimate of the expected 90° detector signal fractional increase, we find:

$$\frac{\Delta Sig_{90^\circ}}{Sig_{90^\circ}} \approx \frac{W_{shift} t_{crit}}{W_{fo} t_{shift}} \quad (5.6)$$

where ΔSig_{90° is the expected 90° detector signal increase, W_{shift} and W_{fo} are the source weighted loss rates induced by the shift (integrated over AC in Fig. 5.8) and from first orbit loss (integrated over AB in Fig. 5.8), respectively, and t_{crit} and t_{shift} are the time to slow down to the critical energy and shift time, respectively. For the 1.4 MA case depicted in Fig. 5.8(a), in which it is assumed that the α -particles gain no energy during the shift, an estimated 50% increase is predicted. This result was used for the expected lost alpha signal increase of Fig. 5.3(c) during the IN shift.

The predicted 90° detector signal increase is reduced if the α -particles are allowed to gain energy during the IN shift, as discussed in the previous section. The energy gain required to totally eliminate the shift-induced signal increase is found by increasing the α -particle energy until there is no longer a shift of the P/T boundary. Fig. 5.8(b) shows that this case occurs for $\sim 12\%$ α -particle energy gain for the 1.4 MA case. By plotting the P/T boundary for other α energies capable of reaching the 90° detector it is found that the $\sim 12\%$ energy gain necessary to eliminate the signal increase is approximately independent of α -particle energy in the range 1.0–3.5 MeV.

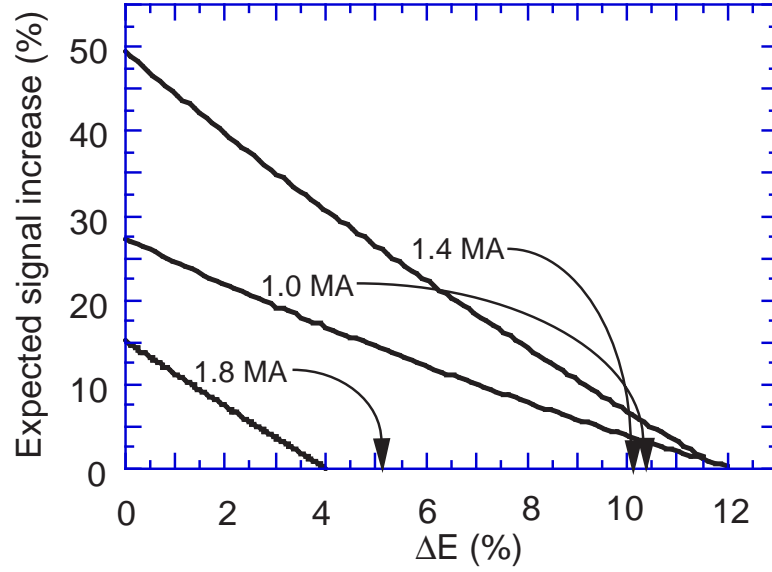


Figure 5.9: Predicted 90° detector signal increase as a function of energy gained by α -particles for each of the three currents. The energy gain, estimated from Eq. 5.3, is shown by the arrows.

This is also the energy gain required to keep the R_{min} point at the same r/a such that the α -particle orbit maintains its position in the plasma with respect to magnetic flux surfaces throughout the R shift. This result is consistent with the heuristic argument of the last section.

Fig. 5.9 shows the predicted 90° detector signal increase as a function of α -particle energy gain estimated using Eq. 5.6. In both the 1.0 and 1.4 MA cases, the shift-induced loss is eliminated at $\sim 12\%$ α -particle energy gain, while the 1.8 MA case cuts off at only $\sim 4\%$ due to the smaller shift range. The energy gain predicted by Eq. 5.3 is depicted by the arrows in Fig. 5.9 for each of the three values of plasma current. It is seen that the energy gained by alpha particles during the IN shift should have a significant effect on the predicted 90° detector signal increase. While the models used are only approximate, they are sufficient to show that the shift-induced alpha loss is reduced by a factor of five or more when the α -particle energy gain is taken into account. While the absolute magnitude of the calculated signal increase is probably only accurate to within a factor of 2 or 3, the important point is that the energy gained by an α -particle is near the point at which no shift-induced

alpha loss is expected.

Additional effects, not taken into account in this model, would tend to further reduce the predicted shift-induced loss. For instance, collisional nonprompt loss has the effect of reducing the population of α -particles in a boundary layer region near the passing/trapped boundary because these particles can pitch angle scatter across to the trapped side of the boundary and become lost. So these particles, which would have been the first to be lost due to the shift, are no longer available to be lost during the shift. Furthermore, the α -particles that are swept out by the boundary have a non-zero average E_{\parallel} resulting in larger energy gain according to Eq. 5.3 and, as can be seen in Fig. 5.9, cause a further reduction in shift-induced loss.

The 1.0 MA case warrants further discussion. The expected signal increase for zero α -particle energy gain is smaller than in the 1.4 MA case. This is because in the 1.0 MA discharge, first orbit loss α -particles can come from the plasma core where the source profile is peaked. In the 1.4 MA case, first orbit loss α -particles can only come from as close as $r/a \approx 0.2$, while the shift-induced α -particles can come from closer in to the core. Thus the shift induces a larger effect in the 1.4 MA case. Also, the shift-induced α -particles in the 1.0 MA case are lost at lower energies since fattest banana α -particle orbits near the birth energy have banana widths that are too large, causing them to strike the vessel on the inboard side. For shift-induced lost α -particles to strike the 90° detector at 1.0 MA, their energy must be $< 0.7 E_0$. Thus a similar size shift induced loss in the 1.0 and 1.4 MA discharges would lead to a lower mean gyroradius in the 1.0 MA case, making it easier to diagnose.

Uncertainties

Several simplifying assumptions were made in calculating the shift-induced loss levels in Fig. 5.9. For instance, it was assumed that the weighting factors of Eq. 5.6 could be represented by the source strength at the orbits' outer midplane crossing point (i.e. the point of closest approach to the magnetic axis where the source is peaked), rather than integrating the source term along entire orbits. Although a counter-going marginally passing orbit is different from a trapped orbit, the steep peakedness of the

source profile combined with the shift of alpha drift surfaces away from flux surfaces (Fig. 2.1), ensures that the alpha distribution of either orbit type is dominated by the contribution from near this OMP crossing point. Furthermore, since the time to slow down to the critical energy, t_{crit} , is short compared to the slowing down time, (τ_{SD}), it was assumed that it would be sufficient to do the calculation at one energy (i.e. the birth energy, or, in 1.0 MA case, the maximum energy at which alphas can reach the 90° detector). These factors combine to make the calculated signal increase accurate to within a factor of 2 or 3. The energy gain at which the shift induced loss is eliminated, however, should be accurate to within a few percent as determined by uncertainty in the magnetic equilibria.

5.3.2 Anomalous Loss Between the Shifts

Another result of this experiment is the unexpected loss of partially thermalized α -particles ($E \approx 0.8E_0$) at the passing/trapped boundary in between the time of the IN and OUT shifts at 1.4 MA. This loss is similar to the loss feature known as ‘delayed’ loss (Sec. 4.4.2) [40] observed in small major radius ($R_0 = 2.45m$) deuterium plasmas at high plasma current ($I_p \geq 1.8$ MA) with the 90° lost alpha scintillator detector. An anomalous loss consistent with ‘delayed’ loss was also observed in deuterium-tritium plasmas using the Alpha Collector probe (Chapter 4). The mechanism causing this loss is not yet understood. However, ‘delayed’ loss is observed to occur at a pitch angle $\sim 10^\circ$ above the passing/trapped boundary in deuterium, and has not been observed in DT plasmas with the 90° lost alpha scintillator detector used in this experiment. The large pitch angle of ‘delayed’ loss requires a large radial step diffusive process to allow α -particles to reach the 90° location without having been previously scraped off at the outer midplane.

A loss at the passing/trapped boundary, such as the anomalous loss at 1.4 MA, does not necessarily require an explanation based on large radial diffusion, since any mechanism that can cause marginally passing α -particles to cross over the boundary is sufficient. Such mechanisms that have been explored in detail are ICRH induced loss [20], collisional nonprompt loss [15], and MHD induced loss [40]. Since there was

no RF in these discharges, ICRH can be ruled out. And although the collisionality of these plasmas went up after the IN shift, it will be shown that collisional loss is such a small contributor to total alpha loss that it isn't expected to be significant during these 'steady state' conditions. These discharges were designed to avoid MHD activity, and it will be shown that there is no correlation between the anomalous loss and what little MHD there is in these discharges. But first, the possibility that the anomalous loss signal is a result of differences in the source and q profiles between the shifted and baseline discharges is examined.

Source and q Profiles

The following arguments regarding the effect of source and q profiles on the mean gyroradius, neutron normalized alpha flux, and pitch angle distribution, support the supposition that the additional alpha loss seen in the 1.4 MA R shifted discharge between the time of the IN and OUT shift is an actual anomalous loss of partially thermalized alphas, and not pure first orbit loss mistaken as such due to instrumental error.

The pitch angle distribution and flux of first orbit alpha loss is dependent on the alpha source and plasma current (or equivalently, q) radial profiles. However, these profiles should not have an effect on the gyroradius distribution of first orbit loss since this loss occurs at a fixed energy of 3.5 MeV ($\pm \sim 0.5$ MeV spread for Doppler shift). Thus, it is not expected that differences in these profiles could account for the ~ 0.2 cm decrease in mean gyroradius seen for the shifted discharge in Fig. 5.5(b) if this observation is to be consistent with first orbit loss. But there could be instrumental errors not taken into account in the error bars in this figure. In particular, it is possible that the model used to map a (ρ, χ) grid onto the scintillator image, which is used to transform alpha impact position on the scintillator to gyroradius and pitch angle (Sec. 2.5.1), is slightly misaligned. This could cause differing pitch angle distributions with the same alpha loss energy to result in slightly differing apparent gyroradius distributions once the transformation is applied.

Fig. 5.10 shows the original 1.4 MA pitch angle distributions of Fig. 5.7 (averaged

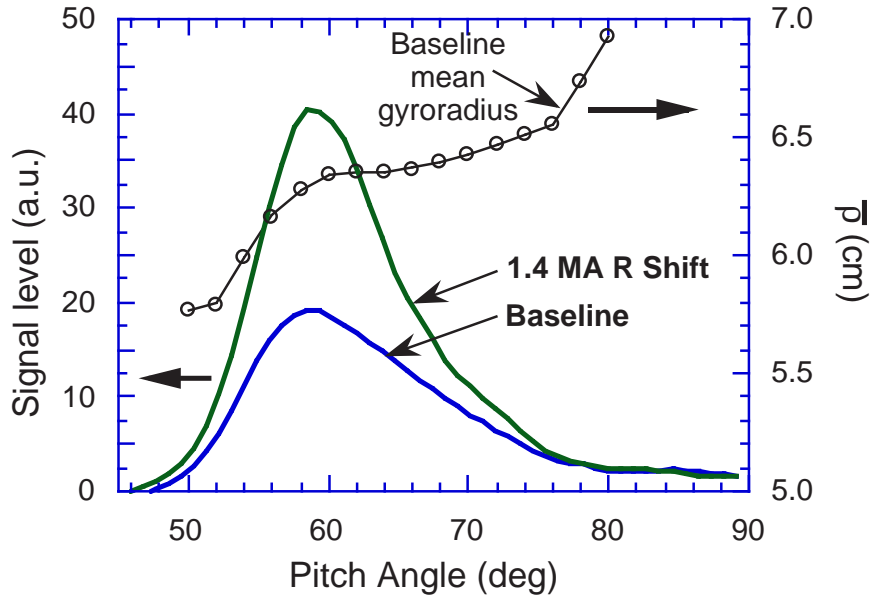


Figure 5.10: *Baseline and shifted pitch angle distributions averaged over 3.9–4.1 s (left scale) and mean gyroradius of the baseline discharge as a function of pitch angle averaged over 2° bins (right scale).*

over the time period of the anomalous loss, 3.9–4.1 s), along with the mean gyroradius of the baseline distribution as a function of pitch angle. The mean gyroradius was calculated for 2° wide bins in pitch angle. Assuming that the energy distribution of the loss is independent of pitch angle (e.g. first orbit loss), one would also expect that the mean gyroradius would be independent of pitch angle. The misalignment of the mapping model must then be responsible for the pitch angle dependence of the mean gyroradius seen in Fig. 5.10. Since the shifted pitch angle distribution is more concentrated at lower pitch angle (where the apparent mean gyroradius is also lower) than the baseline is, the misalignment of the mapping model may cause it to have a lower apparent mean gyroradius. Using the mean gyroradius curve of Fig. 5.10 to calculate the mean gyroradius of the baseline pitch angle distribution, averaged over $50\text{--}80^\circ$ in pitch angle, results in a mean gyroradius value of 6.30 cm, in agreement with the baseline mean gyroradius in Fig. 5.5(b) between the IN and OUT shift. To determine if the pitch angle distribution of the 1.4 MA shifted discharge could cause first orbit loss at 3.5 MeV to appear to have a lower mean gyroradius, the same binned mean gyroradius distribution (i.e. corresponding to first orbit loss) was applied to this

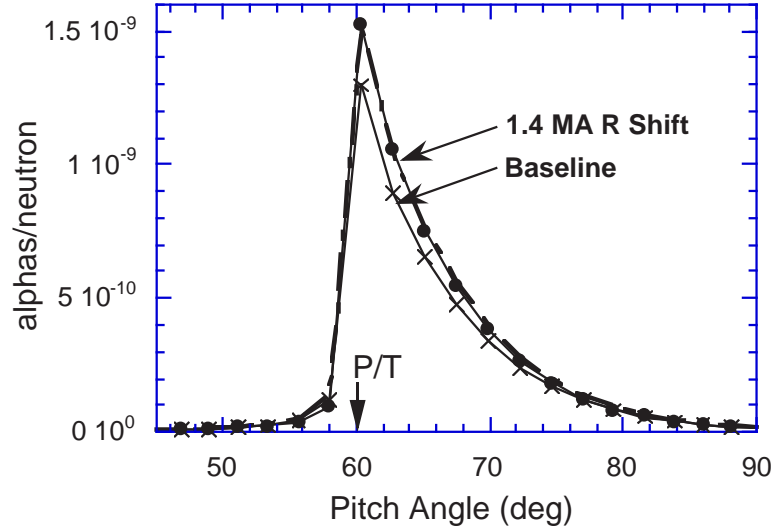


Figure 5.11: Pitch angle distributions for the baseline (x's) and shifted (circles) discharges calculated using the Lorentz ORBIT code. The baseline distribution renormalized to the peak of the shifted distribution is shown by the dashed line.

discharge in the same manner, resulting in a mean gyroradius value of 6.29 cm, only 0.01 cm less than the baseline value. Therefore, the differing pitch angle distributions, combined with a misaligned mapping model, do not account for the ~ 0.2 cm lower mean gyroradius observed for the shifted discharge seen in Fig. 5.5(b).

To further counter the argument that differing source and q profiles are responsible for the anomalous loss features, the TRANSP [16] calculated q profile and the Abel inverted source profile generated from measurements made with the neutron collimator [59] were used to calculate the alpha loss to the 90° detector for the 1.4 MA baseline and shifted discharges at 3.95 s (i.e. during the time of the anomalous loss) using the Lorentz ORBIT code (Sec. 4.2). Fig. 5.11 shows the calculated pitch angle distributions. These distributions are narrower and more sharply peaked at the passing/trapped boundary than those of Fig. 5.7 because they are not ‘smeared’ out by the detector response, which can be modeled by a convolution of these calculated distributions with a Gaussian response function. The slightly differing source and q profiles result in an $\sim 18\%$ larger alpha loss for the shifted discharge as compared to the baseline discharge. This is in consistent with the $\sim 13\%$ spread between the shifted and baseline first orbit calculations at 3.95 s shown in Fig. 5.4(b), which were

done using the TRANSP calculated source profile as input rather than the neutron collimator generated source profile. So the calculated increase in the first orbit loss of $< 20\%$ is significantly less than the observed 70% increase. To compare the shapes of the distributions, the baseline distribution is renormalized to the peak of the shifted distribution (shown by the dashed line), similar to what was done in Fig. 5.7. The shapes of the baseline and shifted distributions are clearly in agreement. There is no peaking of the shifted distribution at the passing/trapped boundary with respect to the baseline distribution as was seen in the observed distributions of Fig. 5.7(b). Therefore, the observed 1.4 MA loss is not consistent with the predicted first orbit loss.

Collisional Loss

To investigate the effect of collisionality, the Hamiltonian guiding center drift orbit Monte Carlo code, ORBIT [43], was used to simulate the slowing down process of α -particles under the conditions of the 1.4 MA R shifted discharge. One thousand particles were allowed to slow down from 3.5 to below 2.5 MeV ($0.7 E_0$) while being acted upon by collisions (Sec. 2.4.1) and stochastic TF ripple diffusion (Sec. 2.3.2). Stochastic ripple diffusion (SRD) is a collisionless process which produces a radial step near the banana tip of those trapped particles that meet a particular threshold criteria [12]. Collisions can act to enhance this loss mechanism by allowing α -particles on previously non-stochastic orbits to exceed this threshold, leading to a synergistic effect [13].

The results from the ORBIT code are presented in Fig. 5.12. For the conditions before the shift, when $R=2.6$ m, a global alpha loss of $\sim 21\%$ is found, as shown by the first bar of Fig. 5.12(a) where a total of 213 of the original 1000 particles are lost. Of this loss, $\sim 26\%$ is nonprompt (i.e. not first orbit loss). However, most of this nonprompt loss occurs near the outer midplane, as is typical for SRD since it is a small step-size radial diffusive process and must first scrape off at the outer midplane where outwardly diffusing orbits first hit the wall. Only about 7% of the alpha loss to a region 10° either side of the 90° wall location (corresponding to only 2 of the

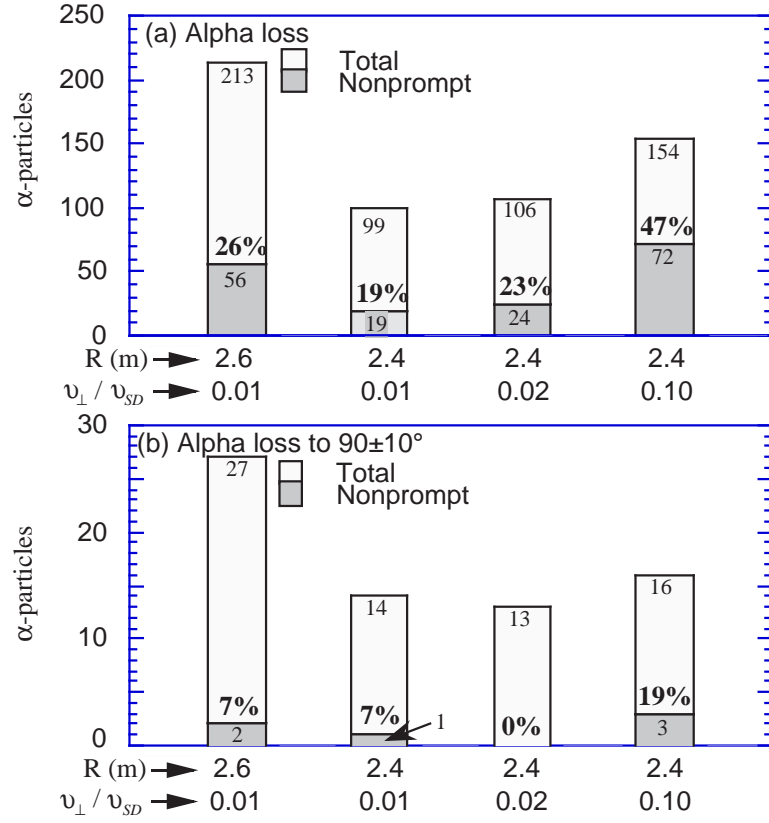


Figure 5.12: *Alpha loss calculated using the guiding center ORBIT code for the 1.4 MA discharge before ($R=2.6$ m) and after ($R=2.4$ m) the IN shift. After the IN shift was run for three values of collisionality. Bars represent (a) total loss to the wall and (b) loss to the bottom of the vessel at $90 \pm 10^\circ$. Total (prompt plus nonprompt) and nonprompt amounts are labeled (out of original 1000 alphas tracked), along with the percentages that make up nonprompt loss.*

original 1000 particles) is nonprompt as seen in the first bar of Fig. 5.12(b). For the conditions after the IN shift, when $R=2.4$ m (i.e. during the anomalous loss), and assuming the same collisionality as the previous case, a global alpha loss of $\sim 10\%$ is found, of which $\sim 19\%$ is nonprompt (second bar of Fig. 5.12(a)). The lower total loss is due to the fact that the magnetic flux surfaces, and hence the alpha orbits, are farther from the walls in a smaller major radius plasma. But still, only about 7% of the alpha loss to a region 10° either side of the 90° wall location (only 1 of original 1000) is nonprompt (second bar of Fig. 5.12(b)).

Of course the effect of compression on the collisionality must be considered. The relevant quantity is the collisionality ratio of the 90° scattering rate to the slowing down rate, ν_\perp/ν_{SD} , since this determines the degree of pitch angle scattering in a slowing down time. This quantity is found to increase on the order of 30% due to the compression. To be conservative, ORBIT was run for the conditions during the anomalous loss with the 90° scattering time halved, so that the collisionality ratio was doubled. The global alpha loss increased slightly to $\sim 11\%$ (third bar of Fig. 5.12(a)), the increase being due to the increase in nonprompt loss (collisional and SRD) which made up $\sim 23\%$ of the loss. However, none of the nonprompt loss hit the wall 10° either side of the 90° location (third bar of Fig. 5.12(b)). Due to the small statistical sample this is not significantly different than the previous two results where there were 2 and then only 1 nonprompt alphas striking this region. What is significant is that this result did not increase to $\sim 70\%$ of first orbit loss in this region (i.e. ~ 9 of original 1000 particles) as is the case for the observed anomalous loss. Even increasing the collisionality ratio by a factor of 10 resulted in only $\sim 19\%$ of the alpha loss to a region 10° either side of the 90° wall location (3 of original 1000) being nonprompt (fourth bar of Fig. 5.12(b)). Thus nonprompt collisional loss does not appear to be a viable explanation for anomalous loss occurring in between the shifts at 1.4 MA.

MHD

The discharges of this experiment were done at relatively low NBI power (i.e. 10 MW) to avoid MHD activity. However, an inspection of measurements made with the Mirnov magnetic probes [60] and the multichannel electron cyclotron emission (ECE) polychromator arrays [61] reveal a low level of MHD in several of the discharges. For instance, the Mirnov signals indicate the presence of a ~ 60 kHz mode near the radius of maximum pressure gradient, features characteristic of the kinetic ballooning mode (KBM) [62], in the 1.0 MA shifted discharge beginning at the end of the IN shift at 3.77 s, and persisting past the end of the OUT shift. KBMs have been observed to cause alpha particle loss at the passing/trapped boundary resulting in an increased loss of up to three times first orbit loss to the 90° detector in high β (plasma pressure/magnetic pressure), high power ($P_B = 21$ MW, $P_{fusion} = 5.5$ MW)

DT plasmas [17]. However, the alpha loss of this 1.0 MA discharge is in agreement with its baseline comparison discharge which did not exhibit MHD activity, indicating that the KBMs of this lower power ($P_B = 10$ MW, $P_{fusion} = 1.1$ MW) discharge were probably too small to cause significant alpha loss.

The 1.4 MA shifted discharge, which produced the anomalous alpha loss results, was done twice to ensure reproducibility. Nearly identical alpha loss results were obtained in both shots. However, one of these discharges exhibits a ~ 50 kHz mode, also consistent with the KBM, whereas the other discharge exhibits a weak $3/2$ mode at ~ 10 kHz. Thus, there does not appear to be a correlation of the anomalous loss with MHD activity.

5.4 Summary, Conclusions, and Suggestions for Future Work

See Sec. 6.3.

Chapter 6

Conclusion

6.1 Introduction

The development of DT fusion tokamak reactors as a long term energy option will require an understanding of the behavior of alpha particles in thermonuclear plasmas. While the confinement of alpha particles is necessary to achieve ignition, a more critical concern is that the loss of these energetic particles could cause damage to the first wall of a reactor.

This thesis covered two experiments investigating separate aspects of escaping alphas in TFTR. Chapters 3 and 4 described the development and results of the alpha collector probe. Chapter 5 described the major radius shift experiment done to investigate the effect on alpha loss. This chapter summarizes these two experiments and draws some conclusions. Suggestions for future experimental work are given here in the event that the TFTR experimental campaign is restarted or that similar results are observed on other machines. However, the suggestions for further modeling do not require an operational tokamak.

6.2 Alpha Collector

6.2.1 Summary

Escaping α -particles have been collected from four DT shots in stacks of thin nickel foils located within the alpha collector probe on TFTR. The subsequent melting of the foils in a closed volume and measurement of the released He as a function of layer depth yields a lost alpha energy distribution, with better than 20% energy resolution. Two rows of eight collimating ports each provide full 180° pitch angle coverage (with the exception of self-shadowing of very deeply trapped particles by the probe head), but with limited pitch angle resolution. The foil deposition technique employed by the alpha collector is accurate to within $\pm 10\%$ at fluences above $\sim 10^9$ alphas, providing an absolutely calibrated measurement to check alpha loss models and to cross calibrate

other detection methods. The lack of electronics and optics gives it good immunity to high neutron fluxes, and the use of a mass spectrometer in the analysis allows for positive ion identification. Although these features make the alpha collector an attractive diagnostic for future fusion reactors, several disadvantages may make other methods preferable. For instance, the alpha collector has no intrinsic time resolution, requires accessibility to retrieve the exposed foils, and requires a long turn around time between exposure and analysis.

The alpha collector has been used to measure escaping alphas in 2.45 m plasmas for two discharges at a plasma current of 1.0 MA, and two discharges at 1.8 MA. For the 1.0 MA discharges, the total alpha fluence, energy distribution, pitch angle distribution, and radial distribution are all in good agreement with the first orbit loss model, and with the signals from the nearby 90° lost alpha scintillator detector, with the exception of a small anomalous loss feature at an energy below ~ 2 MeV. The results of the 1.8 MA discharges, however, display a large anomalous loss feature, in addition to first orbit loss, with an alpha fluence a factor of ~ 6 larger than the predicted first orbit loss. This anomalous loss is broadly peaked at an energy of ~ 2.5 MeV. From this partial thermalization it can be inferred that this loss is ‘delayed’ with respect to alpha production by about one third of the energy e-folding time. The anomalous loss occurs for particles that are co-going at the detector which are more trapped than the fattest banana orbit, and it exhibits a strong radial dependence which may be due to RF limiter shadowing, or an indication of a diffusive loss mechanism. The signals of the 90° scintillator detector during these discharges, however, are in agreement with the first orbit loss model and do not display any sign of this anomalous loss.

6.2.2 Conclusions

The qualitative characteristics of the anomalous loss detected at 1.8 MA with the alpha collector probe are similar to those of the ‘delayed’ loss feature identified in DD plasmas with the 90° scintillator detector [40]. This implies that they may be due to the same loss mechanism, although, it is not understood why the anomalous loss

does not appear on the scintillator detectors in DT.

The strong radial dependence of the anomalous loss, a factor of three decrease in measured fluence from the upper to the lower row of collimating ports, suggests a radial diffusive process, which should cause a reduction in alpha flux due to scrape-off outside the radius of an obstacle such as the RF limiters. However, to go from a marginally confined orbit, which just misses the outer midplane, to the anomalous loss orbit which intercepts the detector, the alpha banana tip would have to jump at least 15 cm. Such a large step-size results in very little radial variation over the 1.1 cm separation between the upper and lower rows of collimating ports. If it is assumed that orbits exist that intercept the RF limiters at the bottom of the vessel first, rather than at the midplane, then a small step-size of ~ 0.2 cm can account for the factor of three drop. However such orbits require that the alpha energy be below the minimum detectable energy of ~ 0.5 MeV. Thus there appears to be an inconsistency between the radial dependence and the diffusive step-size required to bring an α -particle to the detector, making it difficult to develop a model which accounts for the characteristics of the anomalous loss. This inconsistency has led us to question our basic understanding of α -particle orbits in TFTR. In particular, improved modeling of the magnetic fields in the vacuum gap region between the last closed flux surface and the wall may reveal that outwardly diffusing alphas can scrape off at the bottom of the vessel, as well as at the outer midplane. This might provide a mechanism for alphas to reach the alpha collector through the relatively small step-size diffusive process of stochastic ripple diffusion. Such a small step-size diffusive process would be consistent with the absence of the anomalous loss to the 90° scintillator detector, since it is located nearly a cm farther outside the RF limiter radius than the lower row of ports on the alpha collector.

Several possible mechanisms have been considered in an attempt to explain the anomalous loss. The explanation that is most consistent with the observations is charge exchange loss, in which previously confined α -particle orbits transition to prompt loss orbits as a result of electron capture from hydrogen-like carbon impurities. Further work is needed to quantify this loss mechanism and to determine if its effects should be evident to other escaping and confined alpha diagnostics. The most straight forward approach is to develop a guiding center Monte Carlo code to take

into account the probabilities for charge exchange and reionization as a function of alpha energy and minor radius (since plasma and impurity density depend on minor radius). However, the absence of the anomalous loss on the scintillator detectors and its radial dependence do not appear to be consistent with the large step-size diffusion that would be associated with this loss process.

In the design of a fusion reactor it is necessary to be able to predict the alpha wall loading in order to prevent hot spots. Thus, the global alpha loss and its distribution to the first wall is more important than the loss to a localized detector. Unfortunately, it is difficult to make wall loading predictions based on the loss to a single detector. This is because the effective wall area of a given detector (i.e. the area generated by projecting the trajectories of the detected particles onto the first wall as if they had not been stopped by the detector) may vary widely between different types of alpha loss. Although the detected anomalous loss is significantly larger than the predicted first orbit loss, this loss may be preferentially concentrated in the detector (due to a large effective wall area), resulting in a lower actual wall loading than might be expected. For instance, for a small-step diffusive loss mechanism, the effective wall area generated by a detector positioned inside the RF limiter radius can be relatively large since the detector can scrape-off particles that would otherwise have spread over a large area owing to the randomization of the diffusion process.

Similarly, without knowing the loss mechanism, it is difficult to estimate the global alpha loss based on a localized detector since this measurement provides no information regarding poloidal distribution. Assuming that the mechanism responsible for the anomalous loss is impurity charge exchange, then the gc-ORBIT code estimate of $\sim 20\%$ global loss, which is ~ 8 times the first orbit loss prediction (Sec. 4.5.4), can be taken as a ‘best guess’ of the upper limit of the global anomalous alpha loss. However, this may be a gross over-estimate due to the potentially large uncertainties in the charge exchange cross section and the method used to quantify this loss mechanism. As of yet, no other diagnostic results have suggested the existence of such a loss. As for a lower limit of the global anomalous alpha loss, it is conceivable that this loss is very poloidally localized to the bottom of the vessel or that it is concentrated in the detector (due to a large effective wall area), resulting in an insignificant global loss in comparison to first orbit loss.

6.2.3 Suggestions for Future Work

Further work is needed to characterize the anomalous alpha loss seen in this experiment. Scans in plasma current, major radius, beam power, and radial position could shed more light on the anomalous loss. For instance, it should be possible to determine if the small low energy loss feature at 1.0 MA is related to the anomalous loss at 1.8 MA through a plasma current scan. And probe head design changes could improve the quality of the measurement. Such changes could include narrower collimating ports to improve pitch angle resolution, thinner nickel foils to improve energy resolution, and programmable shutters over the foils to improve time resolution.

Further modeling, particularly of the charge exchange loss mechanism, might provide an explanation for the anomalous loss. Efforts to correctly model the magnetic field in the vacuum gap region between the last closed flux surface and the wall [44] might produce orbits that scrape off at the bottom of the vessel rather than at the outer midplane. This could provide a mechanism for alphas lost through stochastic ripple diffusion to reach the alpha collector at the bottom of the vessel.

6.3 Major Radius Shift Experiment

6.3.1 Summary and Conclusions

It has been observed that major radius shifts do not induce additional alpha loss in TFTR, as had been expected. Subsequent modeling of the alpha particle dynamics revealed that the energy gained by marginally passing α -particles during a compression is probably sufficient to avoid mirroring as they move to higher magnetic field, such that they remain passing and confined. However, the major radius shift experiment uncovered a new unexpected loss of partially thermalized ($E \approx 0.8E_0$) α -particles being lost at the passing/trapped boundary. Increased pitch angle scattering of α -particles across the passing trapped boundary in the post-compression,

hotter, denser plasma does not appear to be sufficient to explain this anomalous loss. Observed MHD activity also does not appear to be correlated with this anomalous loss.

6.3.2 Suggestions for Future Work

Future experimental efforts should attempt to further characterize the anomalous loss. This can be accomplished by varying the shift range and rate and by conducting a finer plasma current scan. The delay time after the IN shift could be extended to see if the anomalous loss subsides as the plasma approaches steady state. Further theoretical modeling could improve the alpha loss predictions during the shifts. Modification of a guiding center code such as ORBIT to track the orbits of α -particles throughout the shifts could provide a direct numerical calculation. But priority should be placed on understanding the anomalous loss at 1.4 MA.

Bibliography

- [1] A. Einstein, H. A. Lorentz, H. Minkowski, and H. Weyl, *The Principle of Relativity*. Dover, 1952.
- [2] K. M. McGuire *et al.* *Phys. Plasmas*, vol. 2, p. 2176, 1995.
- [3] L. A. Artsimovich *Nucl. Fusion*, vol. 12, p. 215, 1972.
- [4] N. J. Fisch *Phys. Plasmas*, vol. 2, p. 2375, 1995.
- [5] W. W. Heidbrink *et al.* *Nucl. Fusion*, vol. 34, p. 535, 1994.
- [6] J. A. Rome and Y.-K. M. Peng *Nucl. Fusion*, vol. 19, p. 1193, 1979.
- [7] C. T. Hsu and D. J. Sigmar *Phys. Fluids B*, vol. 4, p. 1492, 1992.
- [8] S. J. Zweben *et al.* *Nucl. Fusion*, vol. 30, p. 1551, 1990.
- [9] S. J. Zweben *et al.* *Nucl. Fusion*, vol. 35, p. 893, 1995.
- [10] R. L. Boivin *et al.* *Nucl. Fusion*, vol. 33, p. 449, 1993.
- [11] O. A. Anderson and H. P. Furth *Nucl. Fusion*, vol. 12, p. 207, 1972.
- [12] R. J. Goldston *et al.* *Phys. Rev. Lett.*, vol. 47, p. 647, 1983.
- [13] M. Redi *et al.* *Nucl. Fusion*, vol. 35, p. 1191, 1995.
- [14] S. J. Zweben *et al.* *Nucl. Fusion*, vol. 35, p. 1445, 1995.

- [15] C. S. Chang *et al.* *Phys. Plasmas*, vol. 1, p. 3857, 1994.
- [16] R. Hawryluk *et al.* in *Proc. Course Varenna, 1979, CEC, Brussels*, vol. 1 of *Physics of Plasmas Close to Thermonuclear Conditions*, p. 19, 1980.
- [17] D. S. Darrow *et al.* *Phys. Plasmas*, vol. 3, p. 1875, 1996.
- [18] R. Nazikian *et al.* *Phys. Rev. Lett.*, vol. 78, p. 2976, 1997.
- [19] R. B. White *et al.* *Phys. Plasmas*, vol. 2, p. 2871, 1995.
- [20] D. S. Darrow *et al.* *Nucl. Fusion*, vol. 36, p. 1, 1996.
- [21] S. J. Zweben *et al.* *Nucl. Fusion*, vol. 29, p. 825, 1989.
- [22] D. S. Darrow *et al.* *Rev. Sci. Instrum.*, vol. 66, p. 476, 1995.
- [23] H. W. Herrmann *et al.* *Rev. Sci. Instrum.*, vol. 66, p. 351, 1995.
- [24] H. W. Herrmann *et al.* *Nucl. Fusion*, p. in press, 1997.
- [25] R. A. Langley *Bull. Am. Phys. Soc.*, vol. 29, p. 1309, 1984.
- [26] R. Bastaz *et al.* *Rev. Sci. Instrum.*, vol. 61, p. 3199, 1991.
- [27] E. V. Carruthers *et al.* *J. Nucl. Mater.*, vol. 176/177, p. 1027, 1990.
- [28] J. Zhu *et al.* *Nucl. Instr. and Meth.*, vol. B59/60, p. 168, 1991.
- [29] J. F. Ziegler, *Helium: Stopping Powers and Ranges in All Elemental Matter*. Pergamon Press, Oxford, 1977.
- [30] A. E. Pontau, C. B. Layne, and W. Bauer *J. Nucl. Mat.*, vol. 103, p. 535, 1981.
- [31] G. P. Chong *et al.* *Bull. Am. Phys. Soc.*, vol. 39, p. 1675, 1994.
- [32] G. P. Chong, "Measurement of helium in nickel foils from the tfr alpha collector probe," Master's thesis, University of Toronto Institute for Aerospace Studies, 1995.
- [33] K. Y. Wong *et al.* *Fusion Engineering and Design*, vol. 16, p. 159, 1991.

- [34] S. J. Zweben *et al.* *Phys. Plasmas*, vol. 1, p. 1469, 1994.
- [35] G. J. Sadler *et al.* *Nucl. Fusion*, vol. 35, p. 1609, 1995.
- [36] J. Felt *et al.* *Rev. Sci. Instrum.*, vol. 61, p. 3262, 1990.
- [37] J. F. Ziegler, J. P. Biersack, and U. Littmark, *The Stopping and Range of Ions in Solids*. Pergamon Press, Oxford, 1985.
- [38] W. Choe *personal communication*, 1996. Princeton Plasma Physics Laboratory.
- [39] L. C. Johnson *et al.* *Rev. Sci. Instrum.*, vol. 66, p. 894, 1995.
- [40] S. J. Zweben *et al.* *Nucl. Fusion*, vol. 33, p. 705, 1993.
- [41] S. J. Zweben *et al.* *Rev. Sci. Instrum.*, vol. 63, p. 4565, 1992.
- [42] S. T. Wang and S. J. ZWEBEN, "Model of alpha particle diffusion in the outer limiter shadow of tftr," PPPL Report 3186, Princeton Plasma Physics Laboratory, 1996. submitted to *Nucl. Fusion Lett.*
- [43] R. B. White *Phys. Fluids B*, vol. 2, p. 845, 1990.
- [44] V. Yavorski *personal communication*, 1996. Inst. for Nuclear Research, Kiev.
- [45] S. J. Zweben *et al.* in *14th Int. Conf. on Plasma Physics and Controlled Nuclear Fusion Research, Wurzburg, 1992*, vol. 1, p. 363, IAEA, Vienna, 1992.
- [46] H. E. Mynick in *Theory of Fusion Plasmas*, (Proc. Joint Varenna-Lausanne Int. Workshop Chexbres, 1988), Editrice Compositori, Bologna, pp. 385–400, 1988.
- [47] R. E. Olson *Phys. Lett.*, vol. 71A, p. 341, 1979.
- [48] R. A. Hulse *Nucl. Technol. Fusion*, vol. 3, p. 259, 1983.
- [49] R. E. Olson *Phys. Rev.*, vol. A16, p. 531, 1977.
- [50] T. G. Winter *Phys. Rev.*, vol. A47, p. 264, 1993.
- [51] T. G. Winter *personal communication*, 1996. Pennsylvania State University, Wilkes-Barre Campus.

- [52] R. F. Heeter *Bull. Am. Phys. Soc.*, vol. 40, p. 1768, 1995.
- [53] R. A. Phaneuf *et al.*, "Atomic data for fusion, vol. v," ornl-6090, Oak Ridge National Laboratory, 1987.
- [54] Z. Bödy and J. Csikai, "Handbook on nuclear activation data," IAEA Tech. Report Series 273, International Atomic Energy Agency, Vienna, 1987. 261-304.
- [55] H. P. Furth and S. Yoshikawa *Phys. of Fluids*, vol. 13, p. 2593, 1970.
- [56] N. N. Gorelenkov *Sov. J. Plasma Phys.*, vol. 16, p. 241, 1990.
- [57] H. W. Herrmann *et al. Bull. Am. Phys. Soc.*, vol. 39, p. 1675, 1994.
- [58] H. W. Herrmann *et al. Bull. Am. Phys. Soc.*, vol. 41, p. 1381, 1996.
- [59] J. D. Strachan *et al. Rev. Sci. Instrum.*, vol. 66, p. 1247, 1995.
- [60] E. Fredrickson *et al. Rev. Sci. Instrum.*, vol. 57, p. 2084, 1986.
- [61] A. Janos *et al. Rev. Sci. Instrum.*, vol. 66, p. 668, 1995.
- [62] Z. Chang *et al. Phys. Rev. Lett.*, vol. 76, p. 1071, 1996.